Doctorate Dissertation (Censored)

博士論文 （要約）

Topology of gap nodes in multi-orbital superconductors

（多軌道超伝導体におけるギャップノードのトポロジー）

A Dissertation Submitted for Degree of Doctor of Philosophy

December 2018

平成 30 年 12 月博士（理学）申請

Department of Physics, Graduate School of Science,

The University of Tokyo

東京大学大学院理学系研究科物理学専攻

Takeru Nakayama

中山　健

Abstract

The concept of topology was introduced in condensed matter systems to apply to quantum Hall systems and other gapped fermionic systems. Recently, it has been extended to gapless, or nodal superconductors. Inspired by these developments, we investigate topological perspective of gap nodes in multi-orbital superconductors. In a usual single-band model, electrons form either spin-singlet or spin-triplet Cooper pairs. In multi-orbital superconductors, their Cooper pairs have more complicated structure beyond spin-triplet bound states due to extra degrees of freedom such as orbital, sublattice, layer and valley. Thus, multi-orbital superconductors may have a new gap topology.

First, we address the issue of how nodeless fully gapped superconducting states are realized in multi-orbital systems even when gap nodes are expected from symmetry. Monolayer FeSe on $SrTiO_3$ substrate is a candidate of nodeless d-wave superconductor, and its pairing originates from a small but finite spin-orbit coupling. We investigate the evolution with decreasing spin-orbit coupling from a nodal state to the nodeless state from a viewpoint of topology. We show that this evolution depends strongly on the orbital degrees of freedom in Cooper pairs. In particular, there are two types of d-wave pairs, which we call orbitally trivial and orbitally nontrivial. In both cases, the gap nodes are characterized by a $\mathbb{Z}$ invariant and carry ± 2 topological charges related to a chiral symmetry. However, their charge distribution in the momentum space is different between the two cases, and this results in different evolutions when these nodes annihilate to form a nodeless state. They exhibit different Andreev flat bands spectra at sample edges. Furthermore, we show that it is possible to probe other types of nodal states by applying in-plane magnetic field. This field leads to the emergence of topologically protected nodal points and nodal line of energy dispersion, which are characterized by a $\mathbb{Z}_2$ invariant.

Second, we address the issue of how we obtain a new type of gap nodes in multi-orbital superconductors and its application. Multi-orbital superconductors with even-parity inversion and broken time-reversal symmetry may have a Fermi surface of Bogoliubov quasiparticles, which is called Bogoliubov Fermi surface, and this is topologically protected. We apply this idea of Bogoliubov Fermi surface to the heavy-fermion superconductor UPt_3. With symmetry consideration, we propose the pairing that belongs to two-dimensional irreducible representation E_{1g} in point group D_{6h}. This is a mixing of spin-singlet d-wave, spin-triplet in-plane p- and out-of-plane f-wave pairing. We show that a finite in-plane p-wave pairing amplitude gives rise to Bogoliubov Fermi surfaces and a finite density of states at zero energy. We further investigate thermal conductivity by using the Boltzmann theory and show that the Bogoliubov Fermi surfaces explain a finite residual density of states and also an anisotropy of thermal conductivity at $T = 0$.

A part of the contents of Chapter 3 is based on the following paper:

1. Takeru Nakayama, Tatsuya Shishidou and Daniel F. Agterberg, Nodal topology in d-wave superconducting monolayer FeSe, Phys. Rev. B **98**, 214503 (2018).

A part of the contents of Chapter 4 is based on the following paper:

2. Takeru Nakayama and Daniel F. Agterberg, Bogoliubov Fermi surfaces in UPt$_3$, in preparation.

The following two papers are not directly related to this thesis.

3. Takeru Nakayama, Ippei Danshita, Tetsuro Nikuni and Shunji Tsuchiya, Fano resonance through Higgs bound states in tunneling of Nambu-Goldstone modes, Phys. Rev. A **92**, 043610 (2015).

4. Takeru Nakayama and Shunji Tsuchiya, Perfect transmission of Higgs modes through virtual Higgs bound states, in preparation.

Contents

Chapter 1

Introduction

Background and motivation

The concept of topology is established as one of the keys in condensed matter systems. Starting from the discovery of integer quantum Hall effect [1], its relevant topological invariant associated with Thouless-Kohmoto-Nightingale-den Nijis (TKNN) formula [2] has brought a novel perspective to condensed matter systems. While Landau theory is successful in characterizing many phases by a *local* order parameter, such integer quantum Hall systems are not classified by Landau theory but have a *nonlocal* order parameter and topological phases [3]. The nonlocal order parameter manifests "bulk-edge correspondence" and predicts the presence of gapless modes at surfaces [4]. These gapless modes are robust against perturbations that preserve the symmetry of the systems. In integer quantum Hall systems, the Hall conductance is quantized and topological classification yields a $\mathbb{Z}$ invariant quantity called Chern number [5]. Topological insulators were found first in HgTe/CdTe quantum wells [6] and are characterized by a nontrivial $\mathbb{Z}_2$ invariant of band topology. They have gapless surface states while their bulk states are fully gapped. Schnyder *et al.* [7] developed the tenfold-way classifications, which is also called Altland-Zirmbauer classification [8], for gapped insulators and superconductors in arbitrary dimensions without interactions and that characterization uses time-reversal, particle-hole, and chiral symmetries.

Topology in superconductors is of great interest in recent years [9–12]. Gapped topological superconductors [13, 14] have attracted much attention because of Majorana surface states. They are fermionic quasiparticles that are their own anti-particles, and emerge due to a nontrivial topology of wave functions of quasiparticles in bulk. These surface states may have important applications for quantum computation technology. It has been also known that nodal superconductors have surface-bound states called Andreev bound states [15], which appear due to the sign change of gap function. Recently, it has been found that the Andreev bound states are a consequence of nontrivial topology of the nodal structure of superconductors [16].

Many theories of superconductivity have mainly studied single band systems and it is believed that the physics is qualitatively unchanged in superconductors with extra internal degrees of freedom such as orbital, sublattice, layer and valley or higher spin. Density functional theory [17, 18] and angle-resolved photoemission spectroscopy (ARPES) experiments [19–21] indicate that iron pnictide superconductors have multiple Fermi surfaces. A consensus [22] is that multiple orbitals play an essential role in pairing mechanism, differing

from other superconductors including high-T_c cuprates. Indeed, a recent theoretical study showed that the presence of significant amount of zero energy states due to inter-orbital pairing in iron pnictide superconductors [23]. It is also expected that inter-orbital pairing plays an important role in the other materials $Cu_xBi_2Se_3$ [24, 25] and YPtBi [26, 27]. Moreover, ARPES experiments of monolayer FeSe grown on $SrTiO_3$ substrate [28–31] showed that its superconducting state has a fully gapped energy dispersion of quasiparticles, but the dispersion has a nontrivial anisotropy [31]. The group of Agterberg recently predicted that its superconducting state has d-wave symmetry without nodes [32]. This is due to finite but too large spin-orbit coupling and nontrivial inter-orbital pairing, whereas typical d-wave states have topologically protected nodes in single-band systems [33]. In their theory, the spin-orbit coupling plays an essential role. It is necessary to stabilize the nodeless state, but gap nodes appear if the coupling is too large. A question is the mechanism that leads to a nodeless, fully gapped d-wave superconducting state, i.e., how such nodeless states emerge when nodes are expected from symmetry? In this thesis, we study this issue through an examination of the nodal d-wave state based on the established classification in gapless fermionic systems [34–36].

Another feature of multi-orbital superconductors is the possibility of an unusual gap structure. In usual single-band models, superconducting gaps are either nodeless or otherwise, have point or line nodes. However, multi-orbital superconductors may have a different type of gap structures. Bogoliubov Fermi surface [37] is proposed for multi-orbital superconductors with even-parity and broken time-reversal symmetries. As will be explained in Section 2.3, Bogoliubov Fermi surfaces are inflated from point or line nodes and they are characterized by a $\mathbb{Z}_2$ invariant [38] related to particle-hole conjugate and parity symmetries [39]. However, their experimental signatures have not yet been explored. In this thesis, we show that the Bogoliubov Fermi surfaces may explain thermal conductivity at low temperatures in the heavy fermion superconductors UPt_3 where polar Kerr effect experiment [40] reported broken time-reversal symmetry.

Outline of the thesis

This thesis is organized as follows. Chapter 2 is a review of pairing symmetry in unconventional superconductors and topology of their gap nodes. Chapters 3 and 4 are the main parts of this thesis. Chapter 5 is a summary and conclusion.

In Chapter 2, we review the basis of unconventional superconductivity with an emphasis on superconducting gap nodes. The study of gap nodes is important not only to investigate the pairing mechanism but also to identify topologically nontrivial surface states. In Section 2.2, we briefly review the topological classification in gapped fermionic systems based on Altland-Zirmbauer (AZ) classification [7, 8]. Such a topological classification has been generalized to gapless fermionic systems including nodal superconductors. Their gap nodes have topological charges characterized by $\mathbb{Z}$ or $\mathbb{Z}_2$ invariant. These will be used in Chapter 3. We also review multi-orbital physics in superconductors. In Section 2.3, we explain a new type of superconducting gap structure, Bogoliubov Fermi surfaces introduced by Agterberg *et al.* [37].

Chapter 3 is the first main part of this thesis, and we study monolayer superconductor FeSe grown on $SrTiO_3$ substrate. Section 3.1 is a review of recent experiments. In Section 3.2, we follow Ref. [32] and introduce a symmetry-based effective model to describe the electronic structure near the M-point of Brillouin zone. The model uses one representation of the point group D_{4h}. This representation is four-dimensional and forms two bands each of which is doubly degenerate. In this model, nodal points emerge due to interband spin-orbit coupling.

In Section 3.3, we show that the topological charges of these nodal points are a $2\mathbb{Z}$ invariant based on the established classification for gapless fermionic systems [36]. There are two topologically different phases, and they have different types of dispersionless Andreev surface states. In Section 3.4, we consider the case that the time-reversal symmetry is broken by applying the Zeeman field. We show the presence of topologically protected nodal points and nodal lines and they are characterized by $\mathbb{Z}_2$ invariants.

Chapter 4 is the second main part, and we study the multi-component superconductor UPt$_3$. Section 4.1 reviews relevant experiments to identify the gap symmetry. One plausible candidate of gap symmetry is E_{2u} representation in the point group D_{6h}. However, this does not explain that thermal conductivity shows that the presence of a finite residual density of states or neither a finite ratio of the in-plane to c-axis thermal conductivity unless impurity effects are taken into account. Therefore, in order to explain such low-temperature behaviors, we start in Section 4.2 from the model introduced in Refs. [41–43] for describing the normal-state electronic structure in UPt$_3$ and consider a two-dimensional representation E_{1g} symmetry in Section 4.3. For this even-parity pairing, we apply the idea of Bogoliubov Fermi surfaces. This E_{1g} representation includes the p-, d- and f- wave pairing amplitudes. In Section 4.4, we show that the in-plane p-wave pairing amplitude needs have a finite amplitude to realize the Bogoliubov Fermi surfaces. We calculate the thermal conductivity and show that this explains experiments in UPt$_3$ as far as the p-wave amplitude is not too small.

Chapter 5 is the summary in this thesis and we also make some remarks for future works.

Chapter 2

Nodal topology in unconventional superconductors

In this chapter, we review some of the basis of unconventional superconductivity. In many unconventional superconductors, the superconducting gap vanishes at points or along lines on the Fermi surfaces in the state. They are called gap nodes and imply the presence of low-energy excitations. After a review of the topological classification in gapped fermionic systems, we follow the works of Volovik [44] and introduce a phenomenological model of superconductors with point nodes to demonstrate that the point nodes have topological charges. We also review orbital degrees of freedom in superconductors. Following the works of Agterberg *et al* [37, 45], we explain a new type of superconducting gap structure i.e., Bogoliubov Fermi surfaces, in a multi-orbital superconductor with even-parity and broken time-reversal symmetries.

2.1 Gap function and its symmetry

2.1.1 Single-band model

Unconventional superconductivity is characterized gap function and its symmetry [33]. For its definition, we first consider single-band superconductors with the following effective Hamiltonian

$$\mathcal{H} = \sum_{\boldsymbol{k},\sigma_1,\sigma_2} \varepsilon_{\sigma_1\sigma_2}\left(\boldsymbol{k}\right) c^\dagger_{\boldsymbol{k}\sigma_1} c_{\boldsymbol{k}\sigma_2} + \frac{1}{2} \sum_{\boldsymbol{k},\boldsymbol{k}',\sigma_1,\sigma_2,\sigma_3,\sigma_4} V_{\sigma_1,\sigma_2,\sigma_3,\sigma_4}\left(\boldsymbol{k},\boldsymbol{k}'\right) c^\dagger_{-\boldsymbol{k}\sigma_1} c^\dagger_{\boldsymbol{k}\sigma_2} c_{\boldsymbol{k}'\sigma_3} c_{-\boldsymbol{k}'\sigma_4}, \quad (2.1)$$

where $c_{\boldsymbol{k}\sigma}$ $(c^\dagger_{\boldsymbol{k}\sigma})$ is the annihilation (creation) operator of the electron with momentum $\boldsymbol{k}$ and spin σ. $\varepsilon_{\sigma_1\sigma_2}$ is the electron energy including Zeeman and spin-orbit couplings. Due to the Pauli principle, the pairing interaction $V_{\sigma_1,\sigma_2,\sigma_3,\sigma_4}\left(\boldsymbol{k},\boldsymbol{k}'\right)$ has the following symmetries: $V_{\sigma_1,\sigma_2,\sigma_3,\sigma_4}\left(\boldsymbol{k},\boldsymbol{k}'\right) = -V_{\sigma_2,\sigma_1,\sigma_3,\sigma_4}\left(-\boldsymbol{k},\boldsymbol{k}'\right) = V_{\sigma_1,\sigma_2,\sigma_4,\sigma_3}\left(\boldsymbol{k},-\boldsymbol{k}'\right) = V^*_{\sigma_4,\sigma_3,\sigma_2,\sigma_1}\left(\boldsymbol{k}',\boldsymbol{k}\right)$. The many-body Hamiltonian in Eq. (2.1) can be treated by the mean-field approach. In superconducting states, Cooper pairs have a non-vanishing anomalous expectation value $\langle c_{\boldsymbol{k}\sigma_1} c_{-\boldsymbol{k}\sigma_2} \rangle$, which is related to a gap function,

$$\Delta_{\sigma_1,\sigma_2}\left(\boldsymbol{k}\right) = -\sum_{\boldsymbol{k},\sigma_3,\sigma_4} V_{\sigma_2,\sigma_1,\sigma_3,\sigma_4}\left(\boldsymbol{k},\boldsymbol{k}'\right) \langle c_{\boldsymbol{k}'\sigma_3} c_{-\boldsymbol{k}'\sigma_4} \rangle. \quad (2.2)$$

Then, the mean-field Hamiltonian is given by

$$\mathcal{H} = \sum_{\boldsymbol{k},\sigma_1,\sigma_2} \varepsilon_{\sigma_1\sigma_2}(\boldsymbol{k})\, c_{\boldsymbol{k}\sigma_1}^\dagger c_{\boldsymbol{k}\sigma_2} + \frac{1}{2} \sum_{\boldsymbol{k},\sigma_1,\sigma_2} \left[\Delta_{\sigma_1\sigma_2}(\boldsymbol{k})\, c_{\boldsymbol{k}\sigma_1}^\dagger c_{-\boldsymbol{k}\sigma_2}^\dagger + \text{h.c.} \right]. \tag{2.3}$$

It can be written with 4×4 matrix,

$$\mathcal{H} = \frac{1}{2} \sum_{\boldsymbol{k}} \left[c_{\boldsymbol{k}\uparrow}^\dagger,\ c_{\boldsymbol{k}\downarrow}^\dagger,\ c_{-\boldsymbol{k}\uparrow},\ c_{-\boldsymbol{k}\downarrow} \right] \left[\begin{array}{cc} \hat{\varepsilon}(\boldsymbol{k}) & \hat{\Delta}(\boldsymbol{k}) \\ \hat{\Delta}(\boldsymbol{k})^\dagger & -\hat{\varepsilon}(\boldsymbol{k})^T \end{array} \right] \left[\begin{array}{c} c_{\boldsymbol{k}\uparrow} \\ c_{\boldsymbol{k}\downarrow} \\ c_{-\boldsymbol{k}\uparrow}^\dagger \\ c_{-\boldsymbol{k}\downarrow}^\dagger \end{array} \right], \tag{2.4}$$

where $\hat{\varepsilon}(\boldsymbol{k})$ and $\hat{\Delta}(\boldsymbol{k})$ are 2×2 matrices in the spin space.

The gap function has the symmetry in $\boldsymbol{k}$ space and can be classified by the total spin of Cooper pair. For singlet pairing, the gap function has to be an even function in $\boldsymbol{k}$. Then,

$$\hat{\Delta}(\boldsymbol{k}) = \psi(\boldsymbol{k})\, i\sigma_y = \left[\begin{array}{cc} 0 & \psi(\boldsymbol{k}) \\ -\psi(\boldsymbol{k}) & 0 \end{array} \right], \quad \psi(-\boldsymbol{k}) = \psi(\boldsymbol{k}). \tag{2.5}$$

If $\varepsilon_{\sigma_1\sigma_2}(\boldsymbol{k}) = \varepsilon(\boldsymbol{k})\,\delta_{\sigma_1,\sigma_2}$, the quasiparticle energy for spin-singlet is

$$E(\boldsymbol{k}) = \sqrt{\varepsilon(\boldsymbol{k})^2 + |\psi(\boldsymbol{k})|^2}. \tag{2.6}$$

On the other hand, for triplet pairing, the gap function has to be an odd function in $\boldsymbol{k}$ and

$$\hat{\Delta}(\boldsymbol{k}) = (\boldsymbol{d}(\boldsymbol{k}) \cdot \boldsymbol{\sigma})\, i\sigma_y = \left[\begin{array}{cc} -d_x(\boldsymbol{k}) + i d_y(\boldsymbol{k}) & d_z(\boldsymbol{k}) \\ d_z(\boldsymbol{k}) & d_x(\boldsymbol{k}) + i d_y(\boldsymbol{k}) \end{array} \right], \quad \boldsymbol{d}(-\boldsymbol{k}) = -\boldsymbol{d}(\boldsymbol{k}), \tag{2.7}$$

with $\boldsymbol{d} = (d_x, d_y, d_z)$ vector which transforms as a vector under spin rotation [46]. If $\varepsilon_{\sigma_1\sigma_2}(\boldsymbol{k}) = \varepsilon(\boldsymbol{k})\,\delta_{\sigma_1,\sigma_2}$, the quasiparticle energy for spin-triplet is

$$E_\pm(\boldsymbol{k}) = \sqrt{\varepsilon(\boldsymbol{k})^2 + |\boldsymbol{d}(\boldsymbol{k})|^2 \pm |\boldsymbol{d}(\boldsymbol{k}) \times \boldsymbol{d}(\boldsymbol{k})^*|}. \tag{2.8}$$

If the case $|\boldsymbol{d} \times \boldsymbol{d}^*| \neq 0$, the superconducting state is called *non-unitary*, because $\hat{\Delta}(\boldsymbol{k})\,\hat{\Delta}^\dagger(\boldsymbol{k})$ is not proportional to the identity matrix.

2.1.2   Structure of gap nodes

In the BCS theory, the pairing interaction originates from electron-phonon coupling and is isotropic in $\boldsymbol{k}$ space, and therefore the gap function is also isotropic (See Fig. 2.1 (a)). On the other hand, in unconventional superconductors where pairing interaction originates from electron correlations, the pairing interaction has strong anisotropy. Consequently, the super-conducting gap also has strong anisotropy in many cases, and it can vanish at points or lines on the Fermi surfaces. They are called gap nodes, or simply nodes. One of the examples is high-T_c cuprates, and it is believed that the gap function has d-wave anisotropy due to strong electron correlation. Figure 2.1(b) shows d-wave pairing (more precisely $d_{x^2-y^2}$-wave). The zero points of the gap function are located in the direction of $\pm 45°$ and $\pm 135°$ and they form line nodes. Gap nodes imply the presence of low-energy excitations. Specific heat and
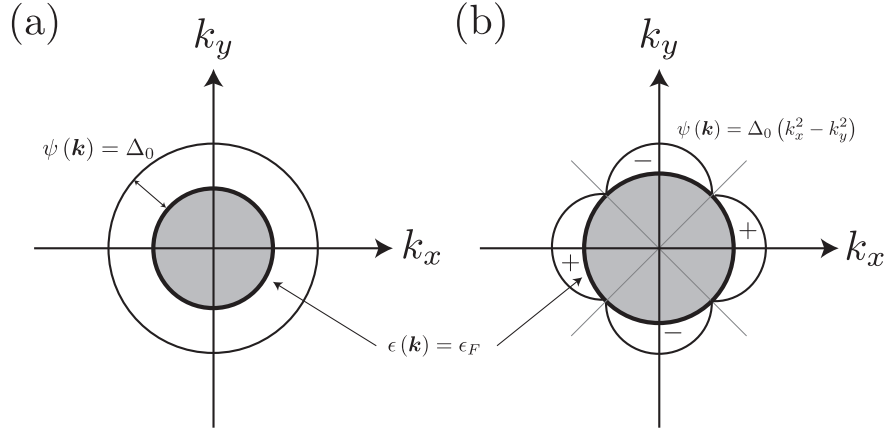
Figure 2.1: Schematic figures of gap function in (a) s-wave $\psi\left(\boldsymbol{k}\right) = \Delta_0$ and (b) d-wave pairing $\psi\left(\boldsymbol{k}\right) = \Delta_0\left(k_x^2 - k_y^2\right)$. The thick solid line and solid line represent the Fermi surfaces and the gap function on the Fermi surfaces, respectively.

Table 2.1: Density of states $\rho\left(\omega\right)$ at low-energy region for different structure of gap nodes.

Type	Dispersion	Example gap $\Delta\left(\boldsymbol{k}\right)$	$\rho\left(\omega\right)$
Gapful	–	const.	0
Point	linear	$\sqrt{k_x^2 + k_y^2}$	ω^2
Point	quadratic	$k_x^2 + k_y^2$	$|\omega|$
Line	linear	k_z	$|\omega|$
Line	quadratic	k_z^2	$\sqrt{|\omega|}$

thermal conductivity, penetration depth, and NMR relaxation rate are strongly affected by gap nodes. They show power-law temperature dependences at low-temperatures, differ from conventional fully gapped superconductors. Therefore, the structure of gap nodes plays an important role to discuss properties such as specific heat, thermal conductivity, penetration depth, NMR relaxation rate, tunneling spectroscopy, and photoemission spectroscopy. Table 2.1 summarizes the density of states $\rho\left(\omega\right) = V^{-1}\sum_{\boldsymbol{k}}\delta(\omega - E_{\boldsymbol{k}})$ in a low-energy region for the different types of gap nodes, where V is the volume of the system and $E_{\boldsymbol{k}}$ is the energy of quasiparticle with momentum $\boldsymbol{k}$.

The Hamiltonian in Eq. (2.1) has some symmetries that represented by a group $\mathcal{G}$. The group $\mathcal{G}$ consists of the global gauge symmetry group $U(1)$, time-reversal symmetry group, the spin rotation symmetry group SU(2), and also space group. Sigrist and Ueda classified the possible superconducting states in a system with the group $\mathcal{G}$, including also spin-orbit coupling with generalized Ginzburg Landau theory [33]. We show that basis functions of the irreducible representations $f\left(\boldsymbol{k}\right)$ of tetragonal point group (D_{4h}) and the hexagonal point group (D_{6h}) in Table 2.2 and 2.3, respectively. (Their character tables are shown in Ap-

Table 2.2: Basis functions of the irreducible representations $f(\boldsymbol{k})$ of the tetragonal point group (D_{4h}).

	$f(\boldsymbol{k})$		$f(\boldsymbol{k})$
A_{1g}	$c,\ k_x^2 + k_y^2,\ k_z^2$	A_{1u}	$k_x\sigma_x + k_y\sigma_y,\ \ k_z\sigma_z$
A_{2g}	$k_x k_y \left(k_x^2 - k_y^2\right)$	A_{2u}	$k_y\sigma_x - k_x\sigma_y$
B_{1g}	$k_x^2 - k_y^2$	B_{1u}	$k_x\sigma_x - k_y\sigma_y$
B_{2g}	$k_x k_y$	B_{2u}	$k_y\sigma_x + k_x\sigma_y$
E_g	$\{k_x k_z,\ k_y k_z\}$	E_u	$\{k_x\sigma_z,\ k_y\sigma_z\}$

Table 2.3: Basis functions of the irreducible representations $f(\boldsymbol{k})$ of the hexagonal point group (D_{6h}).

	$f(\boldsymbol{k})$		$f(\boldsymbol{k})$
A_{1g}	$c,\ k_x^2 + k_y^2,\ k_z^2$	A_{1u}	$k_x\sigma_x + k_y\sigma_y,\ \ k_z\sigma_z$
A_{2g}	$k_x k_y \left(k_x^2 - 3k_y^2\right)\left(k_y^2 - 3k_x^2\right)$	A_{2u}	$k_y\sigma_x - k_x\sigma_y$
B_{1g}	$k_z k_x \left(k_x^2 - 3k_y^2\right)$	B_{1u}	$k_x \left(k_x^2 - 3k_y^2\right)\sigma_z,\ k_z\left[\left(k_x^2 - k_y^2\right)\sigma_x - 2k_x k_y\sigma_y\right]$
B_{2g}	$k_z k_y \left(k_y^2 - 3k_x^2\right)$	B_{2u}	$k_y \left(k_y^2 - 3k_x^2\right)\sigma_z,\ k_z\left[\left(k_x^2 - k_y^2\right)\sigma_y - 2k_x k_y\sigma_x\right]$
E_{1g}	$\{k_x k_z,\ k_y k_z\}$	E_{1u}	$\{k_x\sigma_z,\ k_y\sigma_z\},\ \{k_z\sigma_x,\ k_z\sigma_y\}$
E_{2g}	$\{k_x^2 - k_y^2,\ 2k_x k_y\}$	E_{2u}	$\{k_x\sigma_x - k_y\sigma_y,\ k_y\sigma_x + k_x\sigma_y\}$

pendix C.)

2.2   Topology in superconductors

2.2.1   Topological classification in gapped fermionic systems

Before we discuss topology in nodal superconductors, we briefly review topological classifications of gapped fermionic systems. A pioneering work of discovering integer quantum Hall effect [1] and the presence of invariant quantity associated with Thouless-Kohmoto-Nightingale-den Nijis (TKNN) formula [2] has brought a novel perspective to various condensed matter systems. Landau theory is successful in characterizing many phases by a local order parameter but such integer quantum Hall systems are not classified by Landau theory. They have a nonlocal order parameter and topological phases [3]. The nonlocal order parameter implies "bulk-edge correspondence [4]" and predicts the presence of gapless modes at surfaces or in vortices [13, 14]. These gapless modes are robust against perturbations that preserve the symmetry of the systems. Since then, topology in gapped fermionic systems has attracted much attention. In integer quantum Hall systems, the Hall conductance is quantized and topological classifications yield $\mathbb{Z}$ invariant quantity called Chern number. Topological insulators found first in HgTe/CdTe quantum wells [6] are characterized nontrivial $\mathbb{Z}_2$ invariant of band topology. They have gapless surface states while their bulk states are fully gapped. A. P. Schnyder $et\ al.$ [7] developed the tenfold-way classification which is also called Altland-Zirmbauer (AZ) classification [8], for gapped insulators and superconductors in arbitrary dimensions D without interactions characterized by time-reversal (T), particle-hole

(C), and chiral (S) symmetries.

2.2.2 Nodal superconductors

So far, we have reviewed topological classification in gapped fermionic systems and nontrivial surface states appear as a consequence of "bulk-edge correspondence". In this section, we see that topological classification can be applied to gapless fermionic systems including nodal superconductors [11, 34, 47]. As mentioned in Section 2.1.2, gap nodes imply the presence of low-energy excitations. Here, we introduce a phenomenological model of nodal superconductor with point nodes as an example and show that the point nodes have topological charges. This argument is based on Refs. [11, 44].

We consider spinless superfluid fermions with chiral $p_x + ip_y$-wave pairing. Their Hamiltonian is given by the following Bogoliubov-de Gennes (BdG) form:

$$H\left(\boldsymbol{k}\right) = \left(\frac{\boldsymbol{k}^2}{2m} - \mu\right)\Gamma_z + \frac{\Delta_0}{k_F}\left(k_x\Gamma_x + k_y\Gamma_y\right) \equiv \boldsymbol{g}\left(\boldsymbol{k}\right)\cdot\boldsymbol{\Gamma}, \quad \mu = \frac{k_F^2}{2m}, \tag{2.9}$$

where Pauli matrices Γ_i describe the particle-hole degrees of freedom and k_F is the Fermi wave number. The eigenvalues of this Hamiltonian are $\pm E_{\boldsymbol{k}}$ with

$$E_{\boldsymbol{k}} = \sqrt{\left(\frac{\boldsymbol{k}^2}{2m} - \mu\right)^2 + \left(\frac{\Delta_0}{k_F}\right)^2\left(k_x^2 + k_y^2\right)}, \tag{2.10}$$

and there are two point nodes at the north and south poles of the original Fermi sphere $\boldsymbol{K}_{\pm} = (0,\, 0,\, \pm k_F)$. Consequently, the low-energy physics around the nodes $\boldsymbol{K}_{\pm}$ can be described by the Weyl Hamiltonian

$$H_{\pm}\left(\boldsymbol{p}\right) = \frac{\Delta_0}{k_F}\left(p_x\Gamma_x + p_y\Gamma_y\right) \pm v_F p_z\Gamma_z, \tag{2.11}$$

where $\boldsymbol{p} = \boldsymbol{k} - \boldsymbol{K}_{\pm}$ and $v_F = k_F/m$ is the Fermi velocity. Figures 2.2 (a) and (b) show that two-point nodes at the north and south poles of the Fermi sphere and Weyl dispersion around the nodes, respectively. Remarkably, the point nodes or Weyl nodes are not gapped out and are stable against arbitrary perturbations since the perturbations just shift the position of the point nodes. These point nodes have *topological charges* defined by

$$N_C = \frac{1}{4\pi}\int_C d\boldsymbol{k}\,\tilde{\boldsymbol{g}}\left(\boldsymbol{k}\right)\cdot\left(\frac{\partial\tilde{\boldsymbol{g}}\left(\boldsymbol{k}\right)}{\partial k_1} \times \frac{\partial\tilde{\boldsymbol{g}}\left(\boldsymbol{k}\right)}{\partial k_2}\right), \tag{2.12}$$

where $\tilde{\boldsymbol{g}}\left(\boldsymbol{k}\right) = \boldsymbol{g}\left(\boldsymbol{k}\right)/\left|\boldsymbol{g}\left(\boldsymbol{k}\right)\right|$ is the unit vector field and the region C is a surface which encloses a point node. This topological charge is the winding number of $\tilde{\boldsymbol{g}}\left(\boldsymbol{k}\right)$. Figure 2.2 (c) shows that the hedgehog structure of the unit vector fields $\tilde{\boldsymbol{g}}\left(\boldsymbol{k}\right)$ around a point node. Indeed, the topological charge for the point node of the north (south) pole is $+1$ (-1).

Andreev bound states

Since the 1990s, it has been known that unconventional superconductors have surface bound states called Andreev bound states, which appear due to sign change of the gap function [15]. Zero-energy Andreev bound states are dispersionless in momentum parallel to a surface.
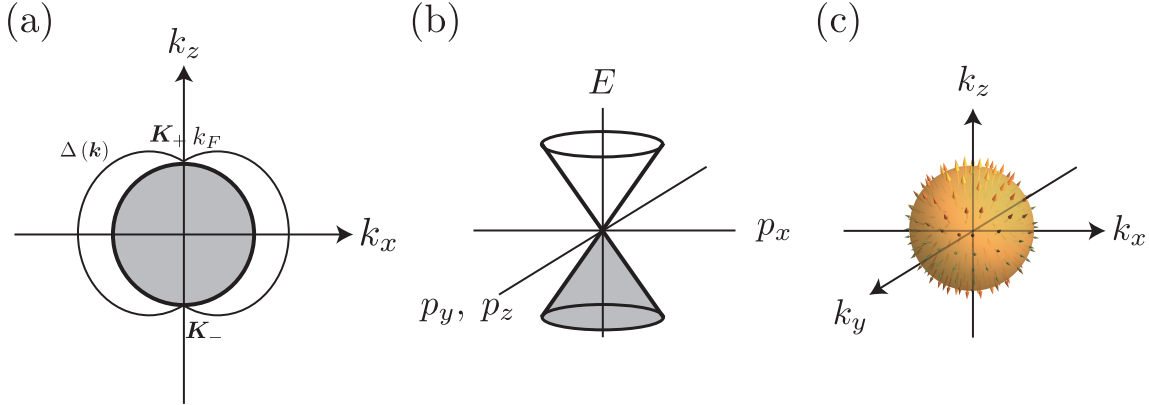
Figure 2.2: (a) Gap anisotropy and two point nodes at the north and south poles of the Fermi sphere $\boldsymbol{K}_{\pm}$. (b) Weyl dispersion around the point node (c) The hedgehog structure of the unit vector $\tilde{\boldsymbol{g}}(\boldsymbol{k})$ around the point node.

They were observed in the high-T_c cuprates with d-wave pairing, and they contribute to the zero-bias conductance peak in tunneling spectroscopy. Recently, it has been found that the Andreev bound states are a result of a nontrivial topology of the nodal structure of superconductors [16].

2.2.3   Gapless centrosymmetric systems

In the previous section, we have shown the stability of the gap nodes for spinless superfluid with chiral $p_x + ip_y$-wave pairing and shown that nodes are characterized by a topological charge. In this sense, though the global topological invariants cannot be defined in gapless fermionic systems, the gap nodes can also be characterized by local topological invariants and classified by AZ (tenfold-way) classification [48–51], similar to fully gapped fermionic systems. AZ classification uses three symmetries: time-reversal (T), particle-hole (C), and chiral (S) symmetries. These operators transform the single-particle Hamiltonian $H(\boldsymbol{k})$ as

$$
\begin{aligned}
TH(\boldsymbol{k})T^{-1} &= H(-\boldsymbol{k}), & T^2 &= \pm\mathbb{1}, \\
CH(\boldsymbol{k})C^{-1} &= -H(-\boldsymbol{k}), & C^2 &= \pm\mathbb{1}, \\
SH(\boldsymbol{k})S^{-1} &= -H(\boldsymbol{k}), & S^2 &= \mathbb{1},
\end{aligned}
\tag{2.13}
$$

where the chiral operator is defined as $S = -iTC$. If the time-reversal or the particle-hole conjugate invariant, squares of time-reversal or particle-hole conjugate operators are either plus or minus the identity operators. Therefore, there are $3 \times 3 = 9$ classes for the Hamiltonian by using the time-reversal and the particle-hole conjugate operators. However, these are not yet all ten classes since it is also necessary to consider the transformation of the Hamiltonian by the chiral operator. In the cases of both the time-reversal and the particle-hole conjugate symmetries are absent, the chiral symmetry either present or absent. Thus, one can obtain $3 \times 3 - 1 + 2 = 10$ possible classes of the Hamiltonian. We note that the time-reversal and the particle-hole conjugate operators are antiunitary, and the chiral operator is unitary and the time-reversal and particle-hole conjugate operators relate Hamiltonians at different $\boldsymbol{k}$ points.

Table 2.4: AZ+$\mathcal{I}$ classification of gapless centrosymmetric systems [36]. ± 1 in $\mathcal{T}$ and $\mathcal{C}$ column indicates the sign of $\mathcal{T}^2$ and $\mathcal{C}^2$. $\times$ denotes the absence of the symmetry. The homotopy groups π_p that determine the charges of a node. $D - d_{\mathrm{BZ}} - 1 \leq p \leq D - 1$ where D is spatial dimension and d_{BZ} is the dimension of Brillouin zone.

class	$\mathcal{T}$	$\mathcal{C}$	S	Homotopy groups		
				π_0	π_1	π_2
A	$\times$	$\times$	$\times$	$\mathbb{0}$	$\mathbb{0}$	$\mathbb{Z}$
AI	$+1$	$\times$	$\times$	$\mathbb{0}$	$\mathbb{Z}_2$	$\mathbb{Z}_2$
AII	-1	$\times$	$\times$	$\mathbb{0}$	$\mathbb{0}$	$\mathbb{0}$
AIII	$\times$	$\times$	1	$\mathbb{0}$	$\mathbb{Z}$	$\mathbb{0}$
BDI	$+1$	$+1$	1	$\mathbb{Z}_2$	$\mathbb{Z}_2$	$\mathbb{0}$
CII	-1	-1	1	$\mathbb{0}$	$\mathbb{0}$	$\mathbb{0}$
D	$\times$	$+1$	$\times$	$\mathbb{Z}_2$	0	$2\mathbb{Z}$
C	$\times$	-1	$\times$	$\mathbb{0}$	$\mathbb{0}$	$\mathbb{Z}$
DIII	-1	$+1$	1	$\mathbb{0}$	$2\mathbb{Z}$	$\mathbb{0}$
CI	$+1$	-1	1	$\mathbb{0}$	$\mathbb{Z}$	$\mathbb{Z}_2$

This classification is firstly applied to gapped fermionic systems. It expands to various condensed matter systems with additional symmetries [52–55]. In this section, we take the additional symmetry as inversion symmetry and we briefly review the topological classification in gapless centrosymmetric systems [36], dubbed the AZ+$\mathcal{I}$ classification, which will be used later in Chapters 3 and 4.

In the centrosymmetric systems, the inversion symmetry is preserved. The inversion operator P transforms Hamiltonian as

$$PH\left(\boldsymbol{k}\right)P^{-1} = H\left(-\boldsymbol{k}\right), \quad P^2 = \mathbb{1}. \tag{2.14}$$

Combining T and C with the inversion operator P,

$$\begin{aligned} \mathcal{T}H\left(\boldsymbol{k}\right)\mathcal{T}^{-1} &= H\left(\boldsymbol{k}\right), \quad \mathcal{T}^2 = \pm\mathbb{1}, \quad \mathcal{T} \equiv TP, \\ \mathcal{C}H\left(\boldsymbol{k}\right)\mathcal{C}^{-1} &= -H\left(\boldsymbol{k}\right), \quad \mathcal{C}^2 = \pm\mathbb{1}, \quad \mathcal{C} \equiv CP. \end{aligned} \tag{2.15}$$

$\mathcal{T}$ and $\mathcal{C}$ do not link with the momentum $\boldsymbol{k}$ to $-\boldsymbol{k}$. They impose local constraints in $\boldsymbol{k}$ space and become relevant for the topological classification of the nodes. Note that $\mathcal{T}$ and $\mathcal{C}$ are also antiunitary, and the set operators $\{\mathcal{T}, \mathcal{C}, S\}$ is mathematically equivalent to the set $\{T, C, S\}$. Therefore, we define tenfold symmetry classes by $\mathcal{T}, \mathcal{C}$ and S. Table 2.4 shows the topological classification of gapless centrosymmetric systems [36]. The homotopy groups π_p that determine the charges of a node are those with $\delta_{\mathrm{CL}} - 1 \leq p \leq D - 1$ where $\delta_{\mathrm{CL}} = D - d_{\mathrm{BZ}}$ is the node codimension for d_{BZ}-dimensional Brillouin zone.

2.3 Multi-orbital physics in superconductors

2.3.1 Bogoliubov Fermi surfaces

Finally, we move on multi-orbital physics in superconductors. Here, orbital stands for the extra degrees of freedom such as orbital, sublattice, layer and valley. Irrespective of the

many types of the additional degree of freedom, superconducting states in the multi-orbital materials are believed to be qualitatively the same as the single-orbital ones. The properties that we have mentioned above also hold for multi-orbital superconductors.

In this section, we introduce a new type of superconducting gap that we call *Bogoliubov Fermi surfaces* [37]. Usual superconducting gaps are either nodeless or otherwise, have point or line nodes. However, multi-orbital superconductors with even-parity and broken time-reversal symmetry may have a different category of gap structure. We show that this new type of nodes is inflated point or line nodes and that they are characterized by a $\mathbb{Z}_2$ invariant. The following arguments are based on Refs. [37, 45].

We start with a general single-electron Hamiltonian with two orbitals by

$$H_N\left(\boldsymbol{k}\right) = \frac{1}{2}\sum_{i,j=0,x,y,z} c_{i,j}\left(\boldsymbol{k}\right)\tau_i\otimes\sigma_j, \tag{2.16}$$

where $\tau_i\,(\sigma_j)$ matrices are Pauli matrices in the orbital (spin) space. Here, we consider the case that the two orbital have real wave functions.

We assume the parity symmetry and the time-reversal symmetry for this Hamiltonian. Since we consider only even-parity states, we restrict to a subspace where the eigenvalues of inversion operator P are $+1$. This is accomplished by $c_{i,j}(-\boldsymbol{k}) = c_{i,j}(\boldsymbol{k})$ and $P = \tau_0\otimes\sigma_0 = \mathbb{1}_4$. P and time-reversal operator T act as

$$PH_N\left(\boldsymbol{k}\right)P^{-1} = H_N\left(-\boldsymbol{k}\right), \tag{2.17}$$

$$TH_N\left(\boldsymbol{k}\right)T^{-1} = H_N\left(-\boldsymbol{k}\right), \tag{2.18}$$

where $T = \tau_0\otimes i\sigma_y K$ where K is the complex-conjugation operator. Combining P and T, we obtain *local* constraint relation in $\boldsymbol{k}$ space,

$$(PT)\,H_N\left(\boldsymbol{k}\right)(PT)^{-1} = H_N\left(\boldsymbol{k}\right). \tag{2.19}$$

Due to this constraint, we should emphasize that it is easily shown that only six Kronecker products $\tau_0\otimes\sigma_0$, $\tau_x\otimes\sigma_0$, $\tau_z\otimes\sigma_0$, $\tau_y\otimes\sigma_x$, $\tau_y\otimes\sigma_y$, and $\tau_y\otimes\sigma_z$ can appear in Hamiltonian (2.16) and the other Kronecker products do not.

In order to gain a deeper understanding of this model, we consider its special case corresponding to the generalized Luttinger-Kohn model [56],

$$\begin{aligned}H_N\left(\boldsymbol{k}\right) &= c_0 I_4 + c_{xy}\frac{J_x J_y + J_y J_x}{\sqrt{3}} + c_{yz}\frac{J_y J_z + J_z J_y}{\sqrt{3}} + c_{zx}\frac{J_z J_x + J_x J_z}{\sqrt{3}}\\ &\quad + c_{3z^2-r^2}\frac{2J_z^2 - J_x^2 - J_y^2}{3} + c_{x^2-y^2}\frac{J_x^2 - J_y^2}{\sqrt{3}},\end{aligned} \tag{2.20}$$

where J's are the angular momenta of $J = 3/2$ given by

$$J_x = \frac{1}{2}\begin{bmatrix} 0 & \sqrt{3} & 0 & 0 \\ \sqrt{3} & 0 & 2 & 0 \\ 0 & 2 & 0 & \sqrt{3} \\ 0 & 0 & \sqrt{3} & 0 \end{bmatrix}, J_y = \frac{i}{2}\begin{bmatrix} 0 & -\sqrt{3} & 0 & 0 \\ \sqrt{3} & 0 & -2 & 0 \\ 0 & 2 & 0 & -\sqrt{3} \\ 0 & 0 & \sqrt{3} & 0 \end{bmatrix},$$

$$\text{and } J_z = \frac{1}{2}\begin{bmatrix} 3 & 0 & 0 & 0 \\ 0 & 1 & 0 & 0 \\ 0 & 0 & -1 & 0 \\ 0 & 0 & 0 & -3 \end{bmatrix}. \tag{2.21}$$

These matrices are related to the five products $\tau_i \otimes \sigma_j$ as

$$\tau_x \otimes \sigma_0 = U^\dagger \frac{J_x^2 - J_y^2}{\sqrt{3}} U, \tag{2.22}$$

$$\tau_z \otimes \sigma_0 = U^\dagger \frac{2J_z^2 - J_x^2 - J_y^2}{3} U, \tag{2.23}$$

$$\tau_y \otimes \sigma_x = U^\dagger \frac{J_y J_z + J_z J_y}{\sqrt{3}} U, \tag{2.24}$$

$$\tau_y \otimes \sigma_y = U^\dagger \frac{J_z J_x + J_x J_z}{\sqrt{3}} U, \tag{2.25}$$

$$\tau_y \otimes \sigma_z = U^\dagger \frac{J_x J_y + J_y J_x}{\sqrt{3}} U, \tag{2.26}$$

with the unitary matrix

$$U = \begin{bmatrix} 1 & 0 & 0 & 0 \\ 0 & 0 & 0 & 1 \\ 0 & 0 & 1 & 0 \\ 0 & 1 & 0 & 0 \end{bmatrix}. \tag{2.27}$$

Now we consider superconducting states that have even-parity and we suppose zero total momentum Cooper pairs. We write the gap function as

$$\Delta(\boldsymbol{k}) = \left(\sum_{i,j=0,x,y,z} \psi_{i,j}(\boldsymbol{k}) \tau_i \otimes \sigma_j \right) U_T. \tag{2.28}$$

where the unitary part of the time-reversal oeprator

$$U_T = \tau_0 \otimes i\sigma_y = \begin{bmatrix} 0 & 0 & 0 & 1 \\ 0 & 0 & -1 & 0 \\ 0 & 1 & 0 & 0 \\ -1 & 0 & 0 & 0 \end{bmatrix}, \tag{2.29}$$

and $\psi_{i,j}(-\boldsymbol{k}) = \psi_{i,j}(\boldsymbol{k})$ since we focus on even-parity pairings. Pauli principle requires either orbital-triplet and spin-singlet or orbitally-singlet and spin-triplet pairing. Therefore, only six Kronecker products $\tau_0 \otimes \sigma_0$, $\tau_x \otimes \sigma_0$, $\tau_z \otimes \sigma_0$, $\tau_y \otimes \sigma_x$, $\tau_y \otimes \sigma_y$, and $\tau_y \otimes \sigma_z$ can appear in the gap function (2.28). Hence, we obtain the six possible gaps matrices η_k in the orbital-spin representation, which are given by

$$\eta_s = U_T, \tag{2.30}$$

$$\eta_{xy} = \frac{J_x J_y + J_y J_x}{\sqrt{3}} U_T, \tag{2.31}$$

$$\eta_{yz} = \frac{J_y J_z + J_z J_y}{\sqrt{3}} U_T, \tag{2.32}$$

$$\eta_{zx} = \frac{J_z J_x + J_x J_z}{\sqrt{3}} U_T, \tag{2.33}$$

$$\eta_{3z^2-r^2} = \frac{2J_z^2 - J_x^2 - J_y^2}{3} U_T, \tag{2.34}$$

$$\eta_{x^2-y^2} = \frac{J_x^2 - J_y^2}{\sqrt{3}} U_T. \tag{2.35}$$

The gap matrix η_s represents an orbitally trivial spin-singlet ($J = 0$) and pure intraband pairing. However, the other five gap matrices represent orbitally nontrivial spin-quintet ($J = 2$) and include both intra- and interband pairings. A general superconducting state is a mixed state with a linear combination of the product of these gaps and $\boldsymbol{k}$-dependent coefficients.

The inflated nodes called Bogoliubov Fermi surfaces to appear in the even-parity superconducting state with broken time-reversal symmetry. As an example, we consider spherically a symmetric normal Hamiltonian

$$H_N = \left(\alpha \boldsymbol{k}^2 - \mu\right) \mathbb{1}_4 + \beta \left(\boldsymbol{k} \cdot \boldsymbol{J}\right)^2, \tag{2.36}$$

where α, spin-orbit coupling β, and chemical potential μ are all constant. This corresponds to the Luttinger-Kohn model with $c_0 = (\alpha + 5\beta/4) \boldsymbol{k}^2 - \mu$, $c_{xy} = \sqrt{3}\beta k_x k_y$, $c_{yz} = \sqrt{3}\beta k_y k_z$, $c_{zx} = \sqrt{3}\beta k_z k_x$, $c_{3z^2-r^2} = \beta \left[k_z^2 - \left(k_x^2 + k_y^2\right)/2\right]$ and $c_{x^2-y^2} = \sqrt{3}\beta \left(k_x^2 - k_y^2\right)/2$. Its eigenvalues are

$$\epsilon_{\pm} = c_0 \pm \sqrt{c_{xy}^2 + c_{yz}^2 + c_{zx}^2 + c_{3z^2-r^2}^2 + c_{x^2-y^2}^2}. \tag{2.37}$$

For simplicity, we consider the case that only one of the two band crosses the chemical potential so that there is only one normal state Fermi surface.

Let us consider an anomalous part of Hamiltonian with broken time-reversal symmetry. The BdG Hamiltonian is given by

$$H\left(\boldsymbol{k}\right) = \left[\begin{array}{cc} H_N\left(\boldsymbol{k}\right) & \Delta\left(\boldsymbol{k}\right) \\ \Delta^{\dagger}\left(\boldsymbol{k}\right) & -H_N^T\left(-\boldsymbol{k}\right) \end{array} \right]. \tag{2.38}$$

We consider a chiral superconducting state with a mixture of spin-singlet and chiral quintet pairings. This is

$$\Delta\left(\boldsymbol{k}\right) = \Delta_1 \psi\left(\boldsymbol{k}\right) \eta_s + \Delta_0 \left(\eta_{zx} + i\eta_{yz}\right) \tag{2.39}$$

where Δ_1 and Δ_0 are real constant and the former (latter) pairing is spin-singlet (-quintet) pairing. We take $\psi\left(\boldsymbol{k}\right) = k_z \left(k_x + ik_y\right)$ that is chiral and breaks time-reversal symmetry and the latter pairing also does.

In order to see the effect of mixing of spin-singlet and spin-quintet pairing, we first consider the case of only spin-singlet pairing. For this case, the gap has two point nodes in the north and south poles and the line node in the basal plane ($k_z = 0$). Mixing on spin-quintet pairing, the original point and the line nodes are inflated and form two-dimensional surfaces as shown in Fig. 2.3, which we call the Bogoliubov Fermi surfaces. Since it is difficult to analytically obtain the eigenvalues of the BdG Hamiltonian (2.38), we solved numerically. These Bogoliubov Fermi surfaces are located a bit far from originally expected nodes.

2.3.2 $\mathbb{Z}_2$ invariant of Bogoliubov Fermi surfaces

In the previous section, we have seen that point and line nodes are inflated and become a new type of gaps nodes, i.e., the Bogoliubov Fermi surfaces in even-parity multi-orbital superconducting states with broken time-reversal symmetry. In this section, we show that this Bogoliubov Fermi surfaces are topologically stable and are characterized by $\mathbb{Z}_2$ invariant quantity [37, 39].
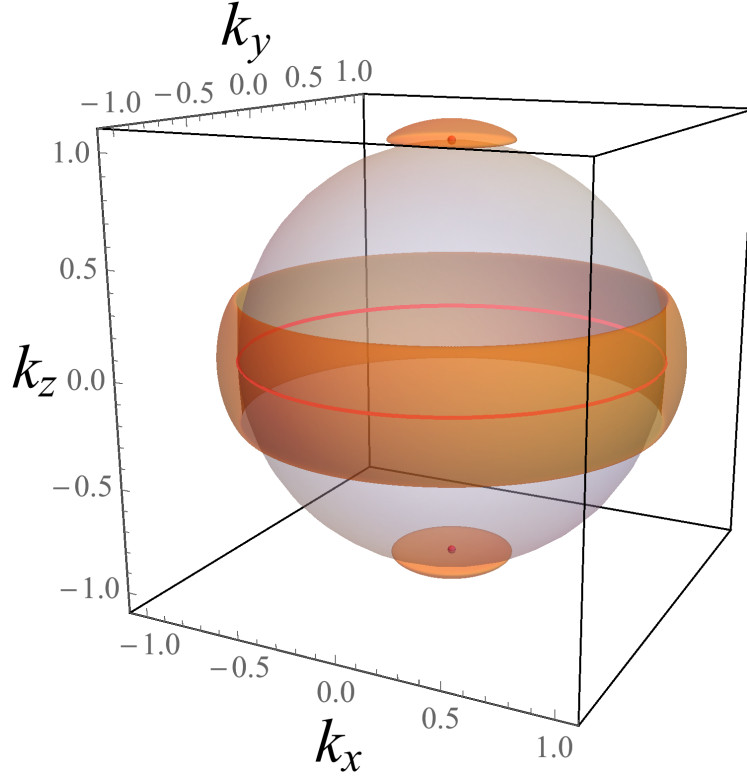
Figure 2.3: Bogoliubov Fermi surfaces (opaque orange) in a chiral superconducting state and normal state Fermi surface (semi-transparent). The point and line nodes that are predicted by single-band theory are red dots and line, respectively. We set parameters $(\alpha,\ \beta,\ \mu,\ \Delta_0,\ \Delta_1) = (1,\ -4/9,\ 8/9,\ 1/5,\ 1/20)$. This is the case that the normal state has only one Fermi surface around Γ point.

The Hamiltonian $H(\boldsymbol{k})$ in Eq. (2.38) has not only parity symmetry but also particle-hole symmetry. The inversion operator and the particle-hole conjugation operators act as

$$\begin{aligned}
PH(\boldsymbol{k})P^{-1} &= H(-\boldsymbol{k}), \\
CH(\boldsymbol{k})C^{-1} &= -H(-\boldsymbol{k}),
\end{aligned} \tag{2.40}$$

where $P = \Gamma_0 \otimes \mathbb{1}_4$ and $C = \Gamma_x \otimes \mathbb{1}_4 K$ with the Pauli matrices Γ_i in the particle-hole space. Combining with C and P, we obtain *local* constraint relation in $\boldsymbol{k}$ space,

$$(CP)H(\boldsymbol{k})(CP)^{-1} = -H(\boldsymbol{k}), \tag{2.41}$$

Because $(CP)^2 = +\mathbb{1}_8$, one can find unitary operator Ω that transform $H(\boldsymbol{k})$ as antisymmetric matrix. We define $U_{CP} \equiv U_C P = \Gamma_x \otimes \mathbb{1}_4$ where $U_C = \Gamma_x \otimes \mathbb{1}_4$. Then,

$$U_{CP}H(\boldsymbol{k})^T U_{CP}^\dagger = -H(\boldsymbol{k}). \tag{2.42}$$

Because U_{CP} is symmetric, it can be diagonalized as

$$U_{CP} = Q\Lambda Q^T, \tag{2.43}$$

where Q is a unitary matrix and Λ is a diagonal matrix. Inserting this into Eq. (2.42),

$$Q\Lambda Q^T H\left(\boldsymbol{k}\right)^T Q^* \Lambda^\dagger Q^\dagger = -H\left(\boldsymbol{k}\right). \tag{2.44}$$

Since Λ is a diagonal matrix, its root, $\sqrt{\Lambda} = \mathrm{diag}\left(\sqrt{\lambda_1}, \sqrt{\lambda_2}, \cdots\right)$ can be defined, even though λ_i are complex and $\sqrt{\Lambda}^\dagger = \left(\sqrt{\Lambda}\right)^{-1}$. Then it is easily shown the following relation,

$$\left(\sqrt{\Lambda}^\dagger Q^\dagger H\left(\boldsymbol{k}\right) Q \sqrt{\Lambda}\right)^T = -\sqrt{\Lambda}^\dagger Q^\dagger H\left(\boldsymbol{k}\right) Q \sqrt{\Lambda}. \tag{2.45}$$

Hence, an anti-symmetric complex matrix can be introduced by $\tilde{H}\left(\boldsymbol{k}\right) = \Omega^\dagger H\left(\boldsymbol{k}\right)\Omega$ where the unitary operator $\Omega = Q\sqrt{\Lambda}$. One can define $\mathbb{Z}_2$ invariant quantity with the sign of Pfaffian [37]

$$P\left(\boldsymbol{k}\right) = \mathrm{sgn}\left[\mathrm{Pf}\,\tilde{H}\left(\boldsymbol{k}\right)\right]. \tag{2.46}$$

We note that this Pfaffian is real since it is a polynomial of even degree of the components of the matrix $\tilde{H}$, which is purely imaginary. Recent studies have shown that a Fermi surface in CP invariant Hamiltonian has nontrivial $\mathbb{Z}_2$ charge and it is stable against CP invariant perturbations [38, 39]. We now express the topological charge in terms of the Pfaffian $P\left(\boldsymbol{k}\right)$. Since $\left[\mathrm{Pf}\,\tilde{H}\left(\boldsymbol{k}\right)\right]^2 = \det\tilde{H}\left(\boldsymbol{k}\right) = \det H\left(\boldsymbol{k}\right)$, the zeros of $P\left(\boldsymbol{k}\right)$ locate at the nodes in superconducting state. Thus, if the opposite sign of $P\left(\boldsymbol{k}\right)$ separates a region in momentum space by a two-dimensional surface, this Fermi surface is guaranteed by the following topological quantity

$$(-1)^l = P\left(\boldsymbol{k}_-\right) P\left(\boldsymbol{k}_+\right) \tag{2.47}$$

where $\boldsymbol{k}_+(\boldsymbol{k}_-)$ is momenta inside (outside) of the Fermi surface. In the normal-state, this $\mathbb{Z}_2$ invariant is trivial since $P\left(\boldsymbol{k}\right) = \epsilon_+\epsilon_-$ is always non-negative. Furthermore, in the case of time-reversal-symmetric superconductors also, there is no nontrivial $\mathbb{Z}_2$ charge since $P\left(\boldsymbol{k}\right)$ can be chosen non-negative for all momentum space [37–39]. However, in the case of superconductors with broken time-reversal symmetry pairing, since there is a region with $P\left(\boldsymbol{k}\right) < 0$ in general, a topologically protected region in momentum space, called Bogoliubov Fermi surface, with the nontrivial $\mathbb{Z}_2$ charge may arise.

2.3.3   Perturbation approach to Bogoliubov Fermi surfaces

We have seen that the topologically stable Bogoliubov Fermi surfaces may appear in even-parity superconducting state with broken time-reversal symmetry and are characterized by $\mathbb{Z}_2$ invariant quantity $(-1)^l$. Let us consider the origin of the Bogoliubov Fermi surfaces. In this section, we use a perturbation approach and show that the Bogoliubov Fermi surfaces emerge driven by internally anisotropic pairing [45].

We start from a two-orbital normal Hamiltonian given by

$$H_N\left(\boldsymbol{k}\right) = \left(\epsilon_{\boldsymbol{k},0} - \mu\right)\mathbb{1}_4 + \boldsymbol{\epsilon_k}\cdot\boldsymbol{\gamma}, \tag{2.48}$$

where $\boldsymbol{\gamma} = \left(\gamma^1, \cdots, \gamma^5\right)$ is the vector of the five Euclidean Dirac matrices and $\epsilon_{\boldsymbol{k},0}$, and $\boldsymbol{\epsilon_k} = \left(\epsilon_{\boldsymbol{k},1}, \cdots, \epsilon_{\boldsymbol{k},5}\right)$ are real even functions of $\boldsymbol{k}$. One can obtain this Hamiltonian from

the Hamiltonian (2.20) by a unitary transformation. We assume that the normal state has both inversion symmetry (P) and time-reversal symmetry (T) where $T = KU_T$ and we chose $U_T = \gamma^1\gamma^2$ without loss of generality. The normal Hamiltonian (2.48) has two different eigenvalues $E_{\boldsymbol{k},\pm} - \mu$ each of which is doubly degenerate

$$E_{\boldsymbol{k},\pm} - \mu = \epsilon_{\boldsymbol{k},0} \pm |\boldsymbol{\epsilon_k}| - \mu. \tag{2.49}$$

The inversion and time-reversal symmetries allow us to label the two eigenstates by a pseudospin index $\sigma = \pm 1$.

Next, we consider pairing potential that has even parity. The general form of the even parity pairing potential is given by

$$\Delta\left(\boldsymbol{k}\right) \;\; = \;\; \left(\eta_{\boldsymbol{k},0} + \boldsymbol{\eta_k} \cdot \boldsymbol{\gamma}\right) U_T, \tag{2.50}$$

$$U_T \;\; = \;\; \begin{bmatrix} 0 & 0 & 0 & 1 \\ 0 & 0 & 1 & 0 \\ 0 & 1 & 0 & 0 \\ 1 & 0 & 0 & 0 \end{bmatrix}, \tag{2.51}$$

where the pairing amplitudes $\eta_{\boldsymbol{k},0}$ and $\boldsymbol{\eta_k} = (\eta_{\boldsymbol{k},1}, \cdots, \eta_{\boldsymbol{k},5})$ are even functions of $\boldsymbol{k}$. The first and second terms in Eq. (2.50) represent internally isotropic and anisotropic pairing, respectively.

To show internally isotropic anisotropic pairing explicitly, we move on the pseudospin basis. The matrix of the BdG Hamiltonian in the pseudospin basis is

$$\begin{bmatrix} \begin{matrix} (E_{\boldsymbol{k},+} - \mu)\,\sigma_0 & 0 \\ 0 & (E_{\boldsymbol{k},-} - \mu)\,\sigma_0 \end{matrix} & \tilde{\Delta}\left(\boldsymbol{k}\right) \\[1.5em] \tilde{\Delta}^\dagger\left(\boldsymbol{k}\right) & \begin{matrix} (-E_{\boldsymbol{k},+} + \mu)\,\sigma_0 & 0 \\ 0 & (-E_{\boldsymbol{k},-} + \mu)\,\sigma_0 \end{matrix} \end{bmatrix}, \tag{2.52}$$

and the pairing potential is now as

$$\tilde{\Delta}\left(\boldsymbol{k}\right) = \begin{bmatrix} \psi_{\boldsymbol{k},+}i\sigma_y & (\psi_{\boldsymbol{k},I} + i\boldsymbol{d_k} \cdot \boldsymbol{\sigma})\,i\sigma_y \\ (\psi_{\boldsymbol{k},I} - i\boldsymbol{d_k} \cdot \boldsymbol{\sigma})\,i\sigma_y & \psi_{\boldsymbol{k},-}i\sigma_y \end{bmatrix}, \tag{2.53}$$

where the intraband pairing potential $\psi_{\boldsymbol{k},\pm}$ is

$$\psi_{\boldsymbol{k},\pm} = \eta_{\boldsymbol{k},0} \pm \frac{\boldsymbol{\epsilon_k} \cdot \boldsymbol{\eta_k}}{|\boldsymbol{\epsilon_k}|}, \tag{2.54}$$

and the interband pairing potential has the following relation:

$$|\psi_{\boldsymbol{k},I}|^2 + |\boldsymbol{d_k}|^2 = |\boldsymbol{\eta_k}|^2 - \frac{|\boldsymbol{\epsilon_k} \cdot \boldsymbol{\eta_k}|^2}{|\boldsymbol{\epsilon_k}|^2}. \tag{2.55}$$

The form of the interband pairing potentials spin-singlet $\psi_{\boldsymbol{k},I}$ and spin-triplet $\boldsymbol{d_k}$ depends on the choice of the pseudospin basis but we note that the off-diagonal blocks in Eq. (2.53) are the interband pairing potential and they originate from the internally anisotropic pairing $\boldsymbol{\eta_k}$. This interband pairing potential provides an important contribution to realize Bogoliubov Fermi surfaces. To see that, we use a perturbation approach and obtain an effective Hamiltonian

for the lower-energy band. A schematic picture of the perturbation approach is shown in Fig. 2.4 (a). We denote the BdG Hamiltonian with the pseudospin basis as

$$
\tilde{H}_{\boldsymbol{k}} = \begin{bmatrix} H_{\boldsymbol{k},+} & H_{\boldsymbol{k},I} \\ H_{\boldsymbol{k},I}^{\dagger} & H_{\boldsymbol{k},-} \end{bmatrix}, \tag{2.56}
$$

where the diagonal blocks $H_{\boldsymbol{k},\pm}$ represent intraband BdG Hamiltonian given by

$$
H_{\boldsymbol{k},\pm} = \begin{bmatrix} \left(E_{\boldsymbol{k},\pm} - \mu\right)\sigma_0 & \psi_{\boldsymbol{k},\pm}i\sigma_y \\ \psi_{\boldsymbol{k},\pm}i\sigma_y & -\left(E_{\boldsymbol{k},\pm} - \mu\right)\sigma_0 \end{bmatrix}, \tag{2.57}
$$

and the diagonal block $H_{\boldsymbol{k},I}$ represents interband pairing and is

$$
H_{\boldsymbol{k},I} = \begin{bmatrix} 0 & \left(\psi_{\boldsymbol{k},I} + i\boldsymbol{d}_{\boldsymbol{k}} \cdot \boldsymbol{\sigma}\right)i\sigma_y \\ \left(\psi_{\boldsymbol{k},I} + i\boldsymbol{d}_{\boldsymbol{k}}^* \cdot \boldsymbol{\sigma}^T\right)i\sigma_y & 0 \end{bmatrix}. \tag{2.58}
$$

Let us assume that only lower-energy band crosses the Fermi level and that the energy gap of two bands is much larger than the pairing potential, $|E_{\boldsymbol{k},+} - E_{\boldsymbol{k},-}| \gg \max\left(\eta_{\boldsymbol{k},0}, \boldsymbol{\eta}_{\boldsymbol{k}}\right)$. The Green's function for the lower-energy band states is given by

$$
\begin{aligned}
G_-^{-1}\left(\boldsymbol{k},\omega\right) &= \omega - H_{\boldsymbol{k},-} - H_{\boldsymbol{k},I}^{\dagger}\left(\omega - H_{\boldsymbol{k},+}\right)^{-1}H_{\boldsymbol{k},I} \\
&\simeq \omega - H_{\boldsymbol{k},-} + \left(E_{\boldsymbol{k},+} - E_{\boldsymbol{k},-}\right)^{-1}H_{\boldsymbol{k},I}^{\dagger}\Gamma_z H_{\boldsymbol{k},I}.
\end{aligned} \tag{2.59}
$$

Here, we use the approximation $H_{\boldsymbol{k},+} \simeq \left(E_{\boldsymbol{k},+} - \mu\right)\Gamma_z$, where Γ_z is the Pauli matrix in the particle-hole space and consider the frequency $\omega \sim E_{\boldsymbol{k},-} - \mu$. Therefore, the effective Hamiltonian for the lower-energy band is

$$
H_{\boldsymbol{k},-}^{\mathrm{eff}} = H_{\boldsymbol{k},-} + \delta H_{\boldsymbol{k},-}, \tag{2.60}
$$

where

$$
\delta H_{\boldsymbol{k},-} = \begin{bmatrix} -\delta\mu_{\boldsymbol{k},-} + \delta\boldsymbol{h}_{\boldsymbol{k},-} \cdot \boldsymbol{\sigma} & 0 \\ 0 & \delta\mu_{\boldsymbol{k},-} - \delta\boldsymbol{h}_{\boldsymbol{k},-} \cdot \boldsymbol{\sigma}^T \end{bmatrix}. \tag{2.61}
$$

Here, the effective chemical potential shift $\delta\mu_{\boldsymbol{k},-}$ and pseudo-magnetic field $\delta\boldsymbol{h}_{\boldsymbol{k},-}$ are calculated for the pairing potential (2.53) and the results are

$$
\delta\mu_{\boldsymbol{k},-} = -\frac{|\psi_{\boldsymbol{k},I}|^2 + |\boldsymbol{d}_{\boldsymbol{k}}|}{2|\epsilon_{\boldsymbol{k}}|}, \tag{2.62}
$$

$$
\delta\boldsymbol{h}_{\boldsymbol{k},-} = \frac{i\boldsymbol{d}_{\boldsymbol{k}} \times \boldsymbol{d}_{\boldsymbol{k}}^* - 2\operatorname{Im}\left(\psi_{\boldsymbol{k},I}\boldsymbol{d}_{\boldsymbol{k}}\right)}{2|\epsilon_{\boldsymbol{k}}|}. \tag{2.63}
$$

We note that pseudo-magnetic field $\delta\boldsymbol{h}_{\boldsymbol{k},-}$ only present when the gap breaks time-reversal symmetry. Indeed, $\delta\boldsymbol{h}_{\boldsymbol{k},-}$ can be written with projection operators $\mathcal{P}_{\boldsymbol{k},-}$ which project onto the lower energy bands at momentum $\boldsymbol{k}$ in

$$
\delta\boldsymbol{h}_{\boldsymbol{k},-} = \frac{\operatorname{Tr}\left[\Delta^{\dagger}\left(\boldsymbol{k}\right)\mathcal{P}_{\boldsymbol{k},-}\boldsymbol{\sigma}\mathcal{P}_{\boldsymbol{k},-}\Delta\left(\boldsymbol{k}\right)\right]}{4|\epsilon_{\boldsymbol{k}}|}. \tag{2.64}
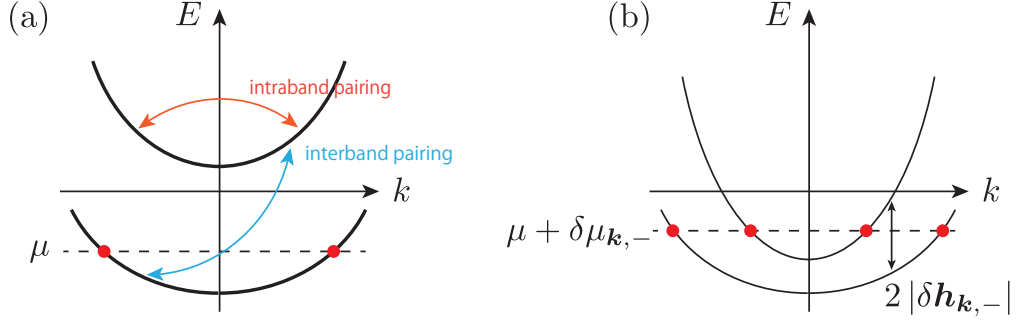$$

Figure 2.4: Schematic pictures for (a) a perturbation approach and (b) given the effective model for the lower-energy band. Thick solid lines represent doubly degenerate spectra and the red dots are the nodes.

This is understood as pseudospin polarization of the non-unitary superconducting state in lower energy bands. Consequently, the eigenvalues of the effective model (2.60) are given by

$$\pm |\delta \boldsymbol{h}_{\boldsymbol{k},-}| \pm \sqrt{[E_{\boldsymbol{k},-} - (\mu + \delta \mu_{\boldsymbol{k},-})]^2 + |\psi_{\boldsymbol{k},-}|^2}. \tag{2.65}$$

When the pseudo-magnetic field $\delta \boldsymbol{h}_{\boldsymbol{k},-}$ is nonzero at nodes of the intraband pairing potential $\psi_{\boldsymbol{k},-}$, the lower energy bands is split and shifted to finite energies, it gives rise to Bogoliubov Fermi surfaces. Figure 2.4 (b) illustrates the emergence of the Bogoliubov Fermi surfaces. The effective pseudo-magnetic field splits the lower energy band to form the Bogoliubov Fermi surfaces, this effective field originates from internally anisotropic pairing $\boldsymbol{\eta}_{\boldsymbol{k}}$.

Chapter 3

Nodal topology of superconducting monolayer FeSe on SrTiO$_3$

Recently, Agterberg *et al.* proposed in Ref. [37] that monolayer FeSe on SrTiO$_3$ substrate is a nodeless d-wave superconductor, and that the pairing originates from a small spin-orbit coupling. The nodeless d-wave state has already been discussed for cuprates [57] but spin-orbit coupling has not been taken into account. In this chapter, based on the recent theory [37], we examine the evolution with increasing spin-orbit coupling from the nodeless state to the nodal state from a viewpoint of topology. We show that this evolution depends strongly on the orbital degrees of freedom in Cooper pairs. In particular, there are two types of d-wave pairs, which we call orbitally trivial and orbitally nontrivial. In both cases, the gap nodes are characterized by a $\mathbb{Z}$ invariant and carry ± 2 topological charges related to a chiral symmetry. However, their charge distribution in the momentum space is different between the two cases, and this results in a different evolution in which these nodes annihilate to form a nodeless state. We show that the two types exhibit different Andreev flat band spectra at sample edges. In Section 3.4, we show a possibility of probing this nodeless state by applying an in-plane magnetic field. This field leads to the emergence of topologically protected nodal points and line, which are characterized by a $\mathbb{Z}_2$ invariant.

3.1   Introduction

Monolayer FeSe grown on SrTiO$_3$ substrate has generated much attention due to its high superconducting transition temperature T_c, which is higher than all the other Fe-based superconductors [58]. Quasiparticle interference experiments [59] and scanning tunneling microscopy (STM) [58, 60] suggest a plain s-wave pairing state. Angle-resolved photoemission spectroscopy (ARPES) experiments [28–31] also support this by observing a fully gapped quasiparticle energy dispersion, though with a nontrivial anisotropy [31]. (See Figs. 3.1(c) and (d).) The s-wave pairing state in this material is a puzzle since superconductivity is expected to be driven by repulsive electron-electron interactions [22]. Furthermore, monolayer FeSe lacks the hole pockets around the Γ-point in the Brillouin Zone (BZ), which exist in other iron pnictide compounds (see Fig. 3.1(b)). In the other iron pnictides, the $s_\pm$-wave pairing is likely [17, 18] and this is driven by spin fluctuations associated with electron scatterings between the electron and the hole pocket [22]. These fluctuations are absent in the monolayer FeSe and therefore the $s_\pm$-wave pairing is unlikely. This has led to a debate about
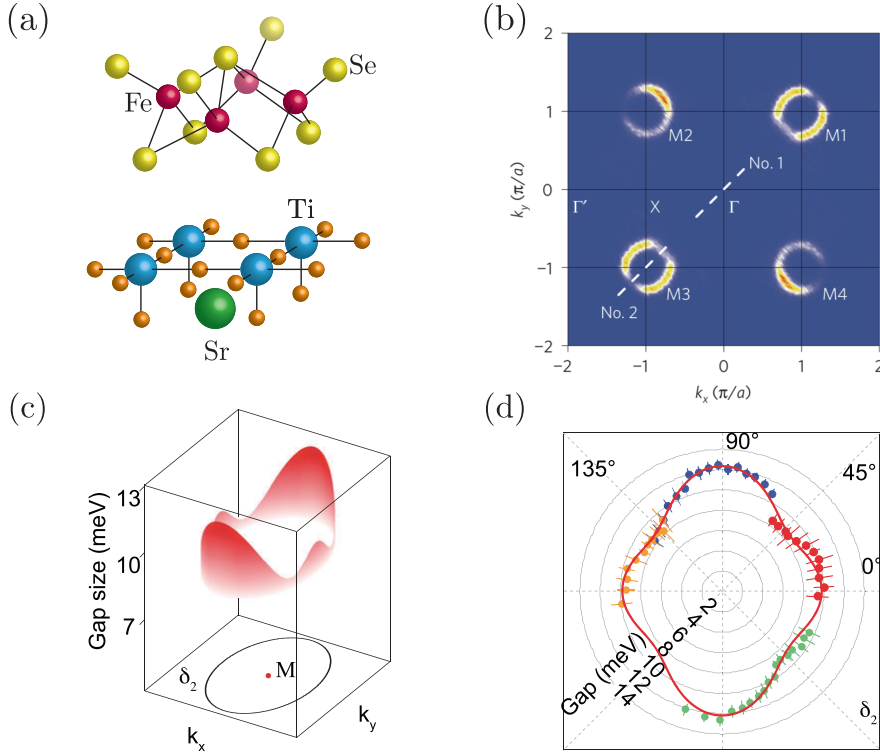
Figure 3.1: (a) Crystal structure of the monolayer FeSe on SrTiO₃ substrate. (b) Fermi surfaces of monolayer FeSe on SrTiO₃ substrate from ARPES experiment [67]. (c) and (d) Anisotropic superconducting gap on the ellipse-like Fermi surface from ARPES experiment [31].

the pairing symmetry. Some proposals are reviewed in Ref. [61] and they include conventional s-wave [59, 62], incipient s-wave [63], extended s-wave [64], fully gapped spin-triplet pairing [65], and nodeless d-wave pairing [32, 66].

Recently, the group of Agterberg has reexamined the pairing symmetry based on the nature of the magnetic correlations in monolayer FeSe [32, 68]. Inelastic neutron scattering experiment in single crystal FeSe [69] observed stripe magnetic fluctuations and also fluctuations associated with checkerboard antiferromagnetic (CB-AFM) order (See Fig. 3.2). The onset of nematic order suppresses CB-AFM [69]. First-principles spin-spiral calculations [68] also predicted enhanced CB-AFM fluctuations in monolayer FeSe, claimed that this system sits near a quantum spin-fluctuation mediated spin paramagnetic ground state. Motivated by the presence of CB-AFM fluctuations, a symmetry based $\boldsymbol{k} \cdot \boldsymbol{p}$ theory was developed to describe fermions around M point in the BZ coupled to these fluctuations [32, 70]. This theory predicts a fully gapped d-wave state [32]. Though symmetry arguments usually predict a nodal d-wave state [33], this theory reveals that nodal points emerge only if the relevant interband spin-orbit coupling exceeds the superconducting gap. This theory thereby naturally accounts for the finite gap minima observed along the expected nodal directions of the d-wave state [31].

インターネット公表に関する同意が
得られなかったため非公表

Figure 3.2: Momentum dependence of the Néel and stripe spin fluctuations at 4 and 110 K [69]. (a) Schematic momentum dependence of the Néel and stripe spin fluctuations in the (H, K) plane of Brillouin zone. (b)-(s) Constant-energy images acquired at 4 or 110 K at indicated energies. With increasing higher energies, the Néel and stripe spin fluctuation overlap and cover a broad area.

A natural question is what is the mechanism that leads to a fully gapped d-wave superconducting state. Indeed, one can ask how such nodeless states are realized when gap nodes are expected from symmetry. In this chapter, we address this question through an examination of the evolution of the nodal d-wave state. This question is naturally related to the growing research on topological insulator and superconductors [10, 14, 71]. It originally started with a study on gapped systems [71] such as quantum Hall systems and topological insulators, and their surface states are characterized by "bulk-edge correspondence [4]." More recently this has been extended to gapless systems such as Weyl and Dirac semimetals [72] and unconventional superconductors [11]. In nodal unconventional superconductors, the sign change of the pairing potential on the Fermi surface leads to dispersionless Andreev bound states at a surface of the system [15]. These states are characterized by topological arguments [16, 73]. Therefore, studies of nodes in unconventional superconductors are important not only to identify the pairing mechanism but also to clarify topological surface states.

Although d-wave states usually have topologically protected nodes in single-band systems, these nodal points can be annihilated in multi-band superconductors [74, 75]. It has been pointed out that the nodal points merge near the Γ-point with those with winding numbers of opposite sign in iron-based superconductors [76]. A nodeless d-wave pairing has also been discussed for cuprates [57]. These previous works did not take account of spin-orbit coupling, which is essential in our theory. We will show the annihilation of nodes due to decreasing spin-orbit coupling and that the nodal charge is protected by a chiral symmetry that is the product of time-reversal and particle-hole symmetries. We also find that the node
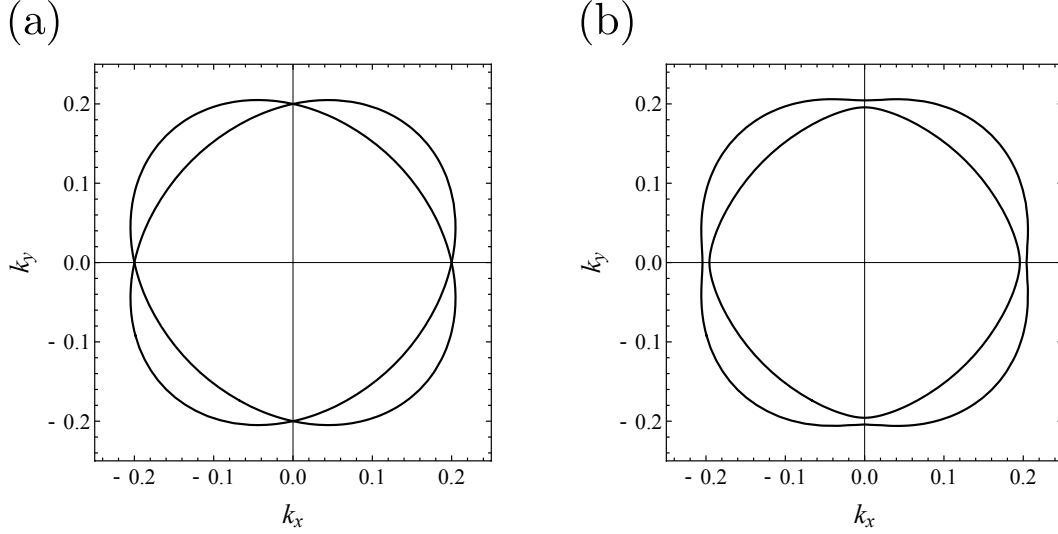
(a)

(b)

Figure 3.3: Fermi surfaces in normal states (a) without spin-orbit coupling and (b) with spin-orbit coupling $v_{\mathrm{so}} = 12$ meV Å. The units of horizontal and vertical axes are Å^{-1}. The other parameters are given in the main text.

annihilation depends upon the orbital structure of the gap function and find two types of B_{2g} pairing: (a) orbitally trivial usual d_{xy}-wave and (b) orbitally nontrivial pairing with no momentum dependence. For the latter nontrivial case, node annihilation arises in a natural and straightforward manner. For the orbitally trivial case, the annihilation is not straight-forward, and proceeds initially through the creation of additional nodes before annihilating as the interband spin-orbit coupling decreases.

3.2   Effective model

A pioneering theoretical model for iron based superconductors was introduced by Kuroki *et al* [17]. They use ten orbital and two spin degrees of freedom and often they obscures the underlying physics. In this section, we briefly review symmetry-based $\boldsymbol{k} \cdot \boldsymbol{p}$-like theory for monolayer FeSe. This describes the electronic states of monolayer FeSe near the Fermi level [32]. Density functional theory calculations show that the Fermi surface around M-point is mainly made of two orbitals, and they are linear combinations of $\{xz, yz\}$ and $x^2 - y^2$ orbitals of Fe ions. They are described by four electronic states (with two orbital and two spin degrees of freedom) through an effective $\boldsymbol{k} \cdot \boldsymbol{p}$ theory. The simplicity of this model allows insight into the underlying physics. It also captures the relevant physics of the superconducting state that appears in monolayer FeSe [65]. Similar effective models are introduced by Chubukov *et al* [77] and Raghu *et al* [78]. Their models do not contain the spin-orbit coupling, which plays an essential role for our model.

In this theory, the two-dimensional normal-state Hamiltonian is

$$H_0(\boldsymbol{k}) = \epsilon_0 (\boldsymbol{k}) \, \sigma_0 \tau_0 + \gamma_{xy} (\boldsymbol{k}) \, \sigma_0 \tau_z + \left[\gamma_x (\boldsymbol{k}) \, \sigma_y + \gamma_y (\boldsymbol{k}) \, \sigma_x \right] \tau_x, \qquad (3.1)$$

where $\boldsymbol{k} = (k_x, k_y)$ is the momentum shift from M-point in BZ and the two types of Pauli

Table 3.1: Function in Hamiltonian (3.1) and set of the parameters that reasonably describe the Fermi surface.

$\epsilon_0(\boldsymbol{k})$	$(k_x^2 + k_y^2)/2m - \mu$	μ	55 meV
$\gamma_{xy}(\boldsymbol{k})$	$ak_x k_y$	$1/(2m)$	1375 meV Å²
$\gamma_x(\boldsymbol{k})$	$v_{\text{so}}k_x$	a	600 meV Å²
$\gamma_y(\boldsymbol{k})$	$v_{\text{so}}k_y$	v_{so}	$\leq$ 15 meV Å

Table 3.2: Symmetry of functions $f(\boldsymbol{k})$ and the Pauli matrices τ_j and σ_i used in the $\boldsymbol{k} \cdot \boldsymbol{p}$ model [32]. They are characterized by irreducible representations Γ at the Γ-point of BZ.

Γ	$f(\boldsymbol{k})$	τ_j	σ_i	Γ	$f(\boldsymbol{k})$	τ_j
A_{1g}	$\epsilon_0(\boldsymbol{k})$	τ_0	$-$	A_{1u}	$-$	τ_y
A_{2g}	$-$	$-$	σ_z	A_{2u}	$-$	$-$
B_{1g}	$k_x^2 - k_y^2$	$-$	$-$	B_{1u}	$-$	$-$
B_{2g}	$k_x k_y$	τ_z	$-$	B_{2u}	$-$	τ_x
E_g	$-$	$-$	$\{\sigma_x, \sigma_y\}$	E_u	$\{k_x, k_y\}$	$-$

matrices τ_i and σ_i describe the orbitals and spin degrees of freedom, respectively. The τ_x term is the spin-orbit coupling, which plays an essential role in the d-wave superconducting state. Its magnitude is related to the on-site spin-orbit coupling but also depends on other factors. Therefore, it may be small even if the on-site spin-orbit coupling is substantial. As observed by angle-resolved photoemission spectroscopy (ARPES), the Fermi surface is reasonably described with the parameters (See Table 3.1).

Figures 3.3 shows the Fermi surfaces in (a) without spin-orbit coupling and (b) with spin-orbit coupling $v_{\text{so}} = 12$ meV Å. The normal state dispersion is given by $\xi^{\pm} = \epsilon_0 \pm \sqrt{\gamma_x^2 + \gamma_y^2 + \gamma_{xy}^2}$ and that have positive-helicity and negative-helicity, respectively. Table 3.2 shows that symmetry of various functions of $\boldsymbol{k}$ and the Pauli matrices τ_j and σ_i.

Superconducting pairing is considered to be induced by the fluctuations associated with CB-AFM [32]. Agterberg *et al* assumed that this spin-fluctuation induces usual spin-singlet and intra-band Cooper pairs and they obtained two types of d_{xy}-like pairing by solving the linear gap equation. Note that with nonzero spin-orbit coupling, the spin-singlet pairing will generally mix with an even parity spin-triplet pairing [70]. Importantly, for this chapter, there are two such pairing states that are described in more detail below. The Hamiltonian is given by the following in the Bogoliubov-de Gennes form:

$$
\begin{aligned}
H(\boldsymbol{k}) = {} & \Gamma_z \left[\epsilon_0 (\boldsymbol{k}) \sigma_0 \tau_0 + \gamma_{xy} (\boldsymbol{k}) \sigma_0 \tau_z + \gamma_x (\boldsymbol{k}) \sigma_y \tau_x \right] \\
& + \gamma_y (\boldsymbol{k}) \Gamma_0 \sigma_x \tau_x + i\Gamma_y \left[\Delta_d (\boldsymbol{k}) \tau_0 + \Delta_z (\boldsymbol{k}) \tau_z \right] i\sigma_y
\end{aligned}
\tag{3.2}
$$

where $\Delta_d(\boldsymbol{k}) = \Delta_2 k_x k_y / k_0^2$, $\Delta_z(\boldsymbol{k}) = \Delta_0$, the Γ_i matrices describe the particle-hole degree of freedom, and we take the typical Fermi wave vector $k_0 = 0.2$ Å^{-1}. The two gap functions $\Delta_d (\boldsymbol{k})$ and $\Delta_z (\boldsymbol{k})$ both belong to B_{2g} representation. The term $\Delta_d (\boldsymbol{k}) \tau_0$ has a trivial part in orbital and a $\boldsymbol{k}$-dependence of B_{2g} symmetry. The $\Delta_z (\boldsymbol{k}) \tau_z$ has an orbital operator with B_{2g} symmetry and no $\boldsymbol{k}$-dependence. Both $\Delta_d (\boldsymbol{k})$ and $\Delta_z (\boldsymbol{k})$ channels have the same symmetry and hybridize in general.

In order to gain a deeper understanding of these two types of B_{2g} pairing, it is convenient to change to the band basis. The Hamiltonian (3.2) is written in block diagonal form with two 4×4 matrices. One of these matrices is

$$
\begin{bmatrix}
\epsilon_0 + \gamma_{xy} & \gamma_y - i\gamma_x & 0 & \Delta_d + \Delta_z \\
\gamma_y + i\gamma_x & \epsilon_0 - \gamma_{xy} & -\Delta_d + \Delta_z & 0 \\
0 & -\Delta_d + \Delta_z & -\epsilon_0 + \gamma_{xy} & \gamma_y + i\gamma_x \\
\Delta_d + \Delta_z & 0 & \gamma_y - i\gamma_x & -\epsilon_0 - \gamma_{xy}
\end{bmatrix},
\tag{3.3}
$$

while the other matrix is given by transforming $\Delta_i \to -\Delta_i$ and $\gamma_x \to -\gamma_x$. Performing a unitary transformation that diagonalizes the normal part of the Hamiltonian, we obtain in the band basis, we find

$$
\begin{bmatrix}
\epsilon_0 + \sqrt{\gamma_x^2 + \gamma_y^2 + \gamma_{xy}^2} & 0 & -\frac{\Delta_z(\gamma_y - i\gamma_x)}{\sqrt{\gamma_x^2 + \gamma_y^2 + \gamma_{xy}^2}} & \Delta_d + \frac{\Delta_z \gamma_{xy}}{\sqrt{\gamma_x^2 + \gamma_y^2 + \gamma_{xy}^2}} \\
0 & \epsilon_0 - \sqrt{\gamma_x^2 + \gamma_y^2 + \gamma_{xy}^2} & -\Delta_d + \frac{\Delta_z \gamma_{xy}}{\sqrt{\gamma_x^2 + \gamma_y^2 + \gamma_{xy}^2}} & \frac{\Delta_z(\gamma_y - i\gamma_x)}{\sqrt{\gamma_x^2 + \gamma_y^2 + \gamma_{xy}^2}} \\
-\frac{\Delta_z(\gamma_y - i\gamma_x)}{\sqrt{\gamma_x^2 + \gamma_y^2 + \gamma_{xy}^2}} & -\Delta_d + \frac{\Delta_z \gamma_{xy}}{\sqrt{\gamma_x^2 + \gamma_y^2 + \gamma_{xy}^2}} & -\epsilon_0 + \sqrt{\gamma_x^2 + \gamma_y^2 + \gamma_{xy}^2} & 0 \\
\Delta_d + \frac{\Delta_z \gamma_{xy}}{\sqrt{\gamma_x^2 + \gamma_y^2 + \gamma_{xy}^2}} & \frac{\Delta_z(\gamma_y - i\gamma_x)}{\sqrt{\gamma_x^2 + \gamma_y^2 + \gamma_{xy}^2}} & 0 & -\epsilon_0 - \sqrt{\gamma_x^2 + \gamma_y^2 + \gamma_{xy}^2}
\end{bmatrix}
\tag{3.4}
$$

This band basis representation shows that the Hamiltonian has both intraband and interband pairings. The interband pairing arises only from the orbitally nontrivial channel Δ_z in combination with the interband spin-orbit coupling. The intraband pairing contains both pairing channels, and the orbitally nontrivial Δ_z channel acquires $\boldsymbol{k}$-dependence with B_{2g} symmetry. Figure 3.4 shows the pairing anisotropy in case of only (a) orbitally trivial pairing and (b) orbitally nontrivial one in the band basis. Note that here only spin-singlet pairings are considered. In general, spin-singlet and triplet pairings can hybridize due to the interband spin-orbit coupling.

The interband pairing generates a gapless superconducting d_{xy} state, provided that the interband spin-orbit coupling is sufficiently small. To examine the condition of the emergence of nodal points along the nodal direction $k_x = 0$ or $k_y = 0$, it is useful to consider the quasiparticle energy of the Hamiltonian (3.2),

$$
E_\pm(\boldsymbol{k}) = \sqrt{\epsilon_0^2 + \gamma_{xy}^2 + \gamma_x^2 + \gamma_y^2 + \Delta_d^2 + \Delta_z^2 \pm 2\sqrt{(\epsilon_0 \gamma_{xy} + \Delta_d \Delta_z)^2 + (\gamma_x^2 + \gamma_y^2)(\epsilon_0^2 + \Delta_z^2)}}.
\tag{3.5}
$$

Along the nodal direction $k_y = 0$, so that $\gamma_{xy} = \gamma_y = \Delta_d = 0$, we obtain $E_\pm(\boldsymbol{k}) = \left| \sqrt{\epsilon_0^2 + \Delta_z^2} \pm |\gamma_x| \right|$. This shows and therefore following relation at the nodal points (labeled $\boldsymbol{k}^*$),

$$
\epsilon_0^2(\boldsymbol{k}^*) = \gamma_x^2(\boldsymbol{k}^*) - \Delta_z^2(\boldsymbol{k}^*).
\tag{3.6}
$$

The nodal points along the directions of $k_x = 0$ or $k_y = 0$ may appear once the interband spin-orbit coupling satisfies $|\gamma_x| > \Delta_z$. As $|\gamma_x|$ decreases, a transition occurs from a nodal to a fully gapped state, which we investigate in the remainder of this chapter. Note that this theory implies that gap minima in the gapped state locate along the nodal directions in the nodal phase, which agrees with what is observed in ARPES measurements [31]. Figure 3.5
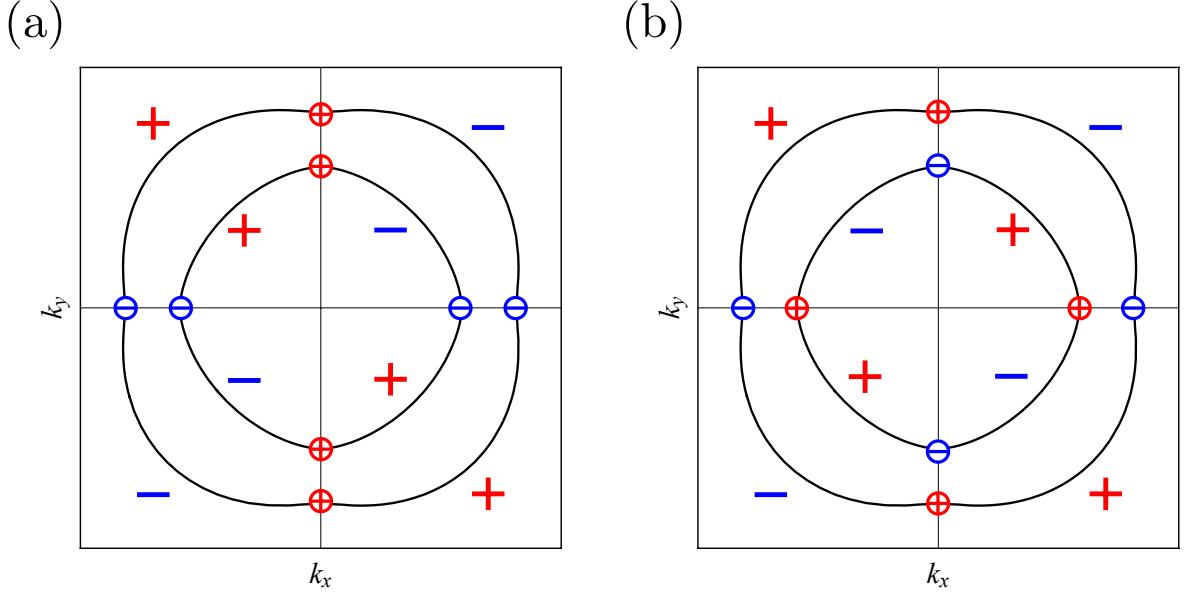
Figure 3.4: Pairing anisotropy and topological charges in (a) orbitally trivial pairing and (b) orbitally nontrivial pairing in band basis with only intraband pairing. The solid lines represent Fermi surface in normal states. The circles represents ± 2 topological charge. (See Section 3.3.)

shows $E_-(\boldsymbol{k})$ on the Fermi surfaces for $v_{\mathrm{so}} = 12$ meV Å(a) and $v_{\mathrm{so}} = 80$ meV Å(b). Along the directions of $k_x = 0$ or $k_y = 0$, the minima of $E_-(\boldsymbol{k})$ locate between the Fermi surfaces in the normal state. When the spin-orbit coupling is strong ($v_{\mathrm{so}} = 80$ meV Å), nodes exist and they locate between the Fermi surfaces.

3.3 Transition of chiral topological charges

3.3.1 Chiral topological charges

Now we examine how the fully gapped d_{xy} state appears as the interband spin-orbit coupling decreases. The following sections are the main parts of Chapter 3. When the interband spin-orbit coupling is sufficiently large, the pairing state is nodal. We show that the nodal point can be characterized by a topological charge that is a $2\mathbb{Z}$ invariant. The key symmetries in defining this charge are time-reversal T and particle-hole conjugation C, which act on $H(\boldsymbol{k})$ as

$$TH(\boldsymbol{k})T^{-1} = H(-\boldsymbol{k}), \tag{3.7}$$

$$CH(\boldsymbol{k})C^{-1} = -H(-\boldsymbol{k}), \tag{3.8}$$

where $T = K\Gamma_0\tau_0\,(i\sigma_y)$, $C = K\Gamma_x\tau_0\sigma_0$, and K is again the complex conjugate operator. Since $T^2 = -1$ and $C^2 = 1$, this Hamiltonian belongs to Altland-Zirnbauer (AZ) class DIII [7]. Furthermore, we define a chiral operator $S = -iTC = \Gamma_x\tau_0\sigma_y$, and $SH(\boldsymbol{k})S^{-1} = H(\boldsymbol{k})$. Since S anticommutes with $H(\boldsymbol{k})$, $H(\boldsymbol{k})$ can be written in a block off-diagonal form using the
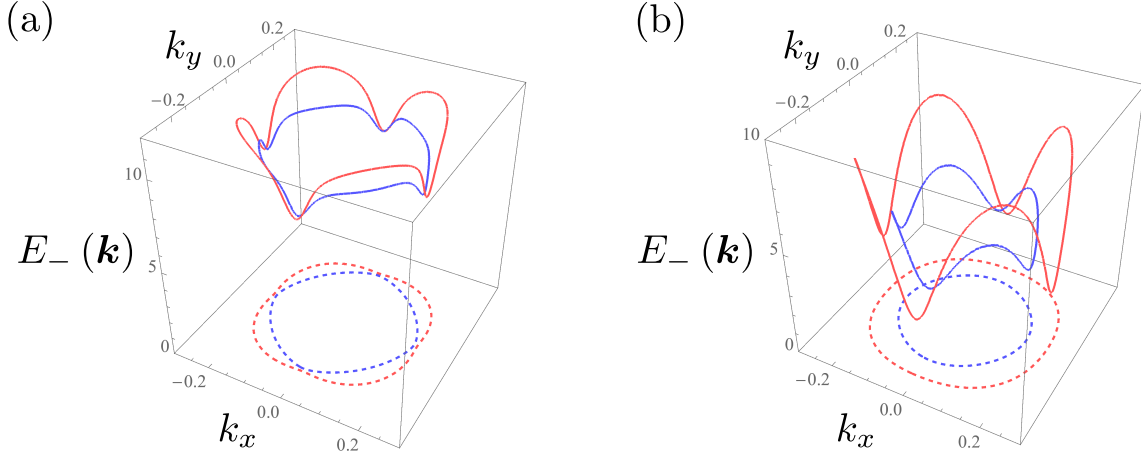
(a)

(b)

Figure 3.5: Gap anisotropy (solid) on the normal-state Fermi surfaces (dashed) for (a) $v_{\mathrm{so}} = 12$ meV Å and (b) $v_{\mathrm{so}} = 80$ meV Å. Along the directions $k_x = 0$ and $k_y = 0$, the gap minima lies between the Fermi surfaces.

basis in which S is diagonal:

$$V H(\boldsymbol{k}) V^\dagger = \begin{bmatrix} 0 & q(\boldsymbol{k}) \\ q^\dagger(\boldsymbol{k}) & 0 \end{bmatrix}, \tag{3.9}$$

where

$$\begin{aligned}
q(\boldsymbol{k}) &= \epsilon_0\left(\boldsymbol{k}\right)\tau_0\sigma_0 + \gamma_{xy}\left(\boldsymbol{k}\right)\tau_z\sigma_0 + \gamma_x\left(\boldsymbol{k}\right)\tau_x\sigma_y + \gamma_y\left(\boldsymbol{k}\right)\tau_x\sigma_x \\
&\quad + i\left(\Delta_d\left(\boldsymbol{k}\right)\tau_0 + \Delta_z\tau_z\right)\sigma_0,
\end{aligned} \tag{3.10}$$

Note that $\det q(\boldsymbol{k^*}) = 0$ at the nodal point $\boldsymbol{k^*}$ because of $E_-(\boldsymbol{k^*}) = 0$.

In the class DIII in two dimensional systems, a topological charge can be defined by the winding number [34], which is given by

$$W_{\mathcal{L}} = \frac{1}{2\pi i} \oint_{\mathcal{L}} d\boldsymbol{k}_l \cdot \mathrm{Tr}\left[q^{-1}(\boldsymbol{k})\nabla_{\boldsymbol{k}_l}q(\boldsymbol{k})\right], \tag{3.11}$$

where the contour $\mathcal{L}$ is a loop around the nodal point. This charge is an integer invariant. The Hamiltonian has the parity symmetry, and this ensures a two-fold degeneracy of the nodal point. Consequently, each node has a $2\mathbb{Z}$ topological charge [36]. We find that the trivial and nontrivial gap functions in the orbital space have different nodal topological charge distributions in momentum space as shown in Fig. 3.4 and that a topological transition exists between these two cases.

To understand the different nodal charge distributions, it is useful to consider the limit in which the interband pairing can be ignored. This is achieved by setting $\Delta_z = 0$ in the orbitally trivial case and by setting $\Delta_d = 0$ and $|\gamma_i| \ll |\gamma_{xy}|$ in the orbitally nontrivial case. When the interband pairing is negligible, the nodal points in two bands are independent. In this case, following Refs [16,73], Eq. (3.11) is simplified to

$$W_{\mathcal{L}^\pm} = -\sum_{\boldsymbol{k}_0 \in S_{\mathcal{L}^\pm}} \mathrm{sgn}\left(\partial_{k_l}\xi_{\boldsymbol{k}}^\pm\big|_{\boldsymbol{k}=\boldsymbol{k}_0}\right) \mathrm{sgn}\left(\Delta_{\boldsymbol{k}_0}^\pm\right). \tag{3.12}$$
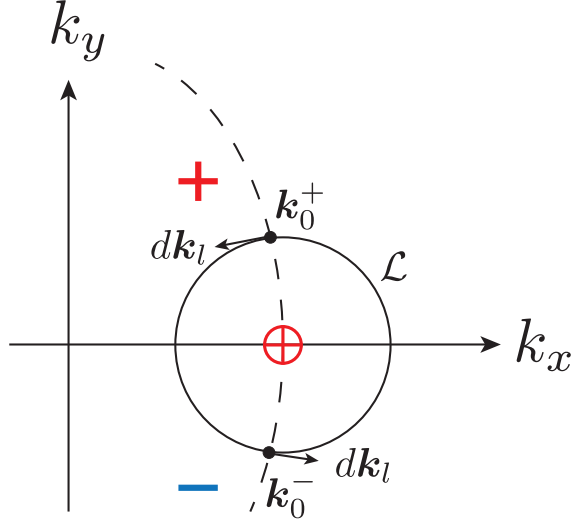
Figure 3.6: Contour $\mathcal{L}$ (solid line), the Fermi surface (dotted line) and set of points $S_{\mathcal{L}} = \{\boldsymbol{k}_0^+, \boldsymbol{k}_0^-\}$ in Eq. 3.12. The sign of $+$ and $-$ represent sign of d_{xy} superconducting gap, respectively.

where $\xi^\pm = \epsilon_0 \pm \sqrt{\gamma_x^2 + \gamma_y^2 + \gamma_{xy}^2}$, $\Delta_{\boldsymbol{k}}^\pm$ is the superconducting gap of $\pm$-helicity and the sum is over the set of points $S_{\mathcal{L}^\pm}$ given by the intersection of $\pm$-helicity Fermi surface with the one-dimensional contour $\mathcal{L}^\pm$ (See Figure 3.6).

We consider explicitly the topological charges of the adjacent pair of nodal points in $k_x(>0)$ direction, $(k_x^{*-}, 0)$ and $(k_x^{*+}, 0)$ with $0 < k_x^{*-} < k_x^{*+}$. In the orbitally trivial case, the superconducting gap $\Delta_{\boldsymbol{k}}^\pm$ of both bands is identical $\Delta_{\boldsymbol{k}}^\pm = -\Delta_d$. Therefore, two nodal points will have the topological charges with the same sign. We call this the *same sign pair* state. On the other hand, in the orbitally nontrivial case, $\Delta_{\boldsymbol{k}}^\pm \sim \mp \gamma_{xy} \Delta_z$, the two nodal points have the opposite sign of topological charge. We call this the *opposite sign pair* states. In general, the orbitally trivial and nontrivial gap functions hybridize, but the nodes are still classified as either same sign pair or opposite sign pair state. A transition between these two topological states occurs with varying the spin-orbit coupling. In both cases, as the spin-orbit coupling decreases, a gapped d_{xy} state must arise assuming that $\Delta_z \neq 0$. The development of this gapless state is intuitively clear for opposite sign pair states, but for same sign pair states.

To understand this point, we generalize the treatment of topological charge. The topological charge (3.11) can be written in the following form:

$$W_{\mathcal{L}} = \frac{1}{\pi} \oint_{\mathcal{L}} d\boldsymbol{k}_l \cdot \nabla_{\boldsymbol{k}_l} \tan^{-1} \left[\frac{2(\epsilon_0 \Delta_d - \gamma_{xy} \Delta_z)}{\epsilon_0^2 - \gamma_x^2 - \gamma_y^2 - \gamma_{xy}^2 - \Delta_d^2 + \Delta_z^2} \right] \tag{3.13}$$

This is the winding number of the vector field $(\epsilon_0^2 - \gamma_x^2 - \gamma_y^2 - \gamma_{xy}^2 - \Delta_d^2 + \Delta_z^2, \ 2(\epsilon_0 \Delta_d - \gamma_{xy} \Delta_z))$ around the nodal point. The term which determines whether the same or opposite sign pair is the numerator $\epsilon_0 \Delta_d - \gamma_{xy} \Delta_z$, since the denominator $\epsilon_0^2 - \gamma_x^2 - \gamma_y^2 - \gamma_{xy}^2 - \Delta_d^2 + \Delta_z^2$ behaves similarly for both cases. Substituting $\boldsymbol{k}$-dependence, the numerator is given by

$$\epsilon_0(\boldsymbol{k}) \Delta_d(\boldsymbol{k}) - \gamma_{xy}(\boldsymbol{k}) \Delta_z = k_x k_y \left(\frac{\Delta_2}{k_0^2} \epsilon_0(\boldsymbol{k}) - a\Delta_0 \right). \tag{3.14}$$
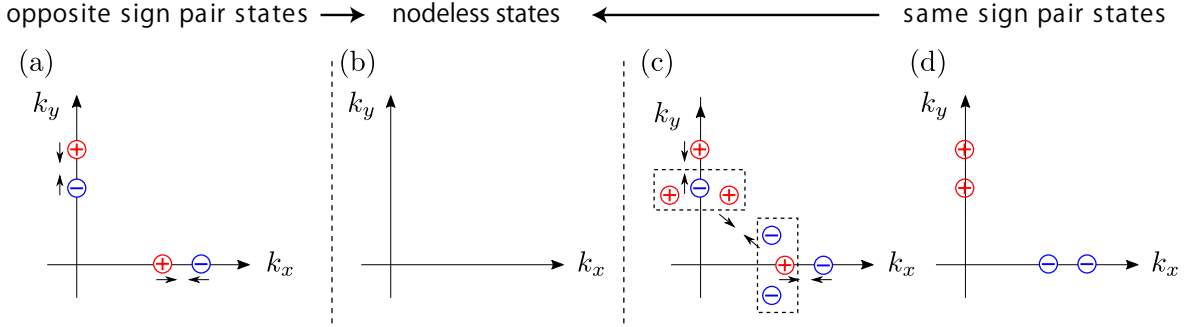
Figure 3.7: Schematic picture of transition to nodeless states from *opposite* (left) and *same sign pair* states (right). The arrows represent that two nodal points merge with each other. In *same sign pair* states, each inner nodal point splits into three nodal points (surrounded by a dotted line) in transition to nodeless states.

If $\Delta_2 = 0$, the sign of the numerator is the same at the two nodal points $\boldsymbol{k}^{*-}$ and $\boldsymbol{k}^{*+}$. This leads to topological charges of opposite sign, i.e., opposite sign pair states. However, if $\Delta_2 \neq 0$ and sign of $\Delta_2/k_0^2\epsilon_0\left(\boldsymbol{k}\right) - a\Delta_0$ changes its sign between the two nodal points, the topological charges have the same sign, leading to the same sign pair states. In order to obtain a condition to distinguish these two cases, we consider $k_y = 0$ direction and define $\tilde{k}_x$ as the solution of $\epsilon_0(\tilde{k}_x) - ak_0^2\Delta_0/\Delta_2 = 0$. In the case of same sign pair state, $k_x^{*-} < \tilde{k}_x < k_x^{*+}$, and this is not satisfied for opposite sign pair states. With the nodal condition Eq. (3.6), we obtain the following inequality,

$$2mv_{\text{so}}^2 - mA < a\frac{\Delta_0}{\Delta_2}k_0^2 < 2mv_{\text{so}}^2 + mA \tag{3.15}$$

with

$$A = \sqrt{2\frac{\mu}{m}v_{\text{so}}^2 - \frac{\Delta_0^2}{m^2} + v_{\text{so}}^4}. \tag{3.16}$$

Let us consider the case of $\Delta_0 = 11$ meV and $\Delta_2 = -1.5$ meV, which was used earlier to reproduce a gap anisotropy consistent with experiment, and assume a strong interband spin-orbit coupling $v_{\text{so}} = 80$ meV Å. Then this is classified as opposite sign pair states.

Now we turn to study how the gapless d_{xy} state develops when nodal points merge and annihilate. This has been studied in Dirac and Weyl semimetals [72] and also in s-and d-wave superconductors [76], but spin-orbit coupling is not an essential interaction in those cases. In the case of opposite sign pair states, the nodal points annihilate as the interband spin-orbit coupling decreases. However, in case of same sign pair states, nodal points cannot annihilate directly because their topological charges have the same sign, and we find an involved mechanism illustrated in Fig. 3.7. Indeed, as the interband spin-orbit coupling decreases, two nodal points are created near the old nodal point (panel (c)). As the spin-orbit coupling further decreases, one nodal point stays near $\boldsymbol{k}^{*-}$, while two nodal points move off the k_x or k_y axis. With decreasing the spin-orbit coupling, they continue to move and annihilate in pairs with other nodes moving from another direction. Figure 3.8 shows the phase diagram of chiral topological charge distribution. There are five regions: nodeless,
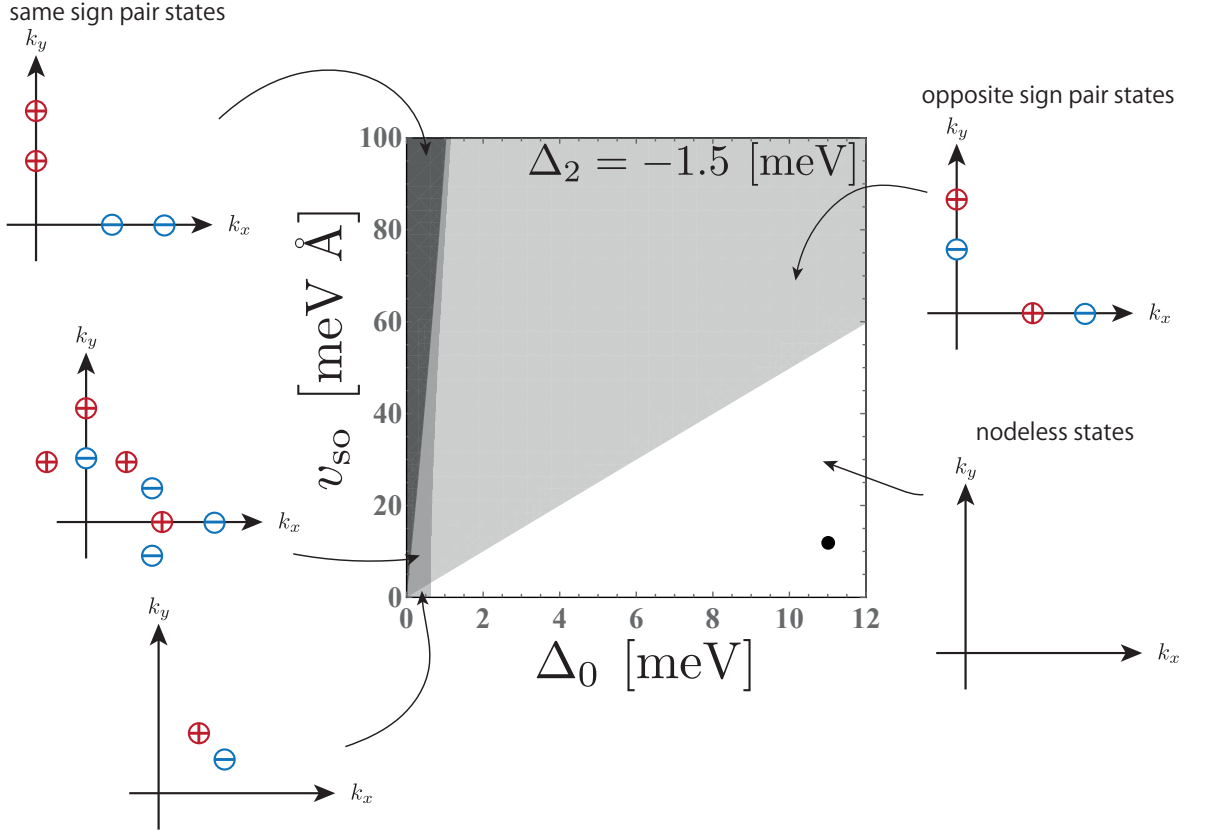
Figure 3.8: Phase diagram of chiral topological charge distribution in $(\Delta_0, v_{\rm so})$ space. There are five regions: nodeless, opposite (same) sign states and two states which have 8 nodal points not on the k_x and k_y axis. We set $\Delta_2 = -1.5$ [meV] and the black dot represents the parameters which reproduces a gap anisotropy consistent with experiment in a monolayer FeSe on SrTiO₃.

opposite (same) sign states and two states which have 8 nodal points not on the k_x and k_y axis. Indeed, in case of same sign pair states, nodal points cannot annihilate directly and the transition to nodeless states occurs through the states with 16 nodal points.

3.3.2 Andreev flat band

We find that either same sign pair states or opposite sign pair states appear when the superconducting state with strong spin-orbit coupling has gap nodes. The state which has 8 nodal points not on the k_x and k_y axis only exists in a narrow range of parameters, and so we do not consider it further here. It would be of interesting experimentally identify same sign or opposite sign pair states. As we show below, one can identify through an examination of edge states. However, we note in advance that the values of the spin-orbit coupling used below are larger than those in monolayer FeSe grown on SrTiO₃. Thus, we do not predict a flat band for this material but there still exist in-gap edge states that are not topologically protected. In order to observe them, it is necessary to enhance spin-orbit coupling, by using
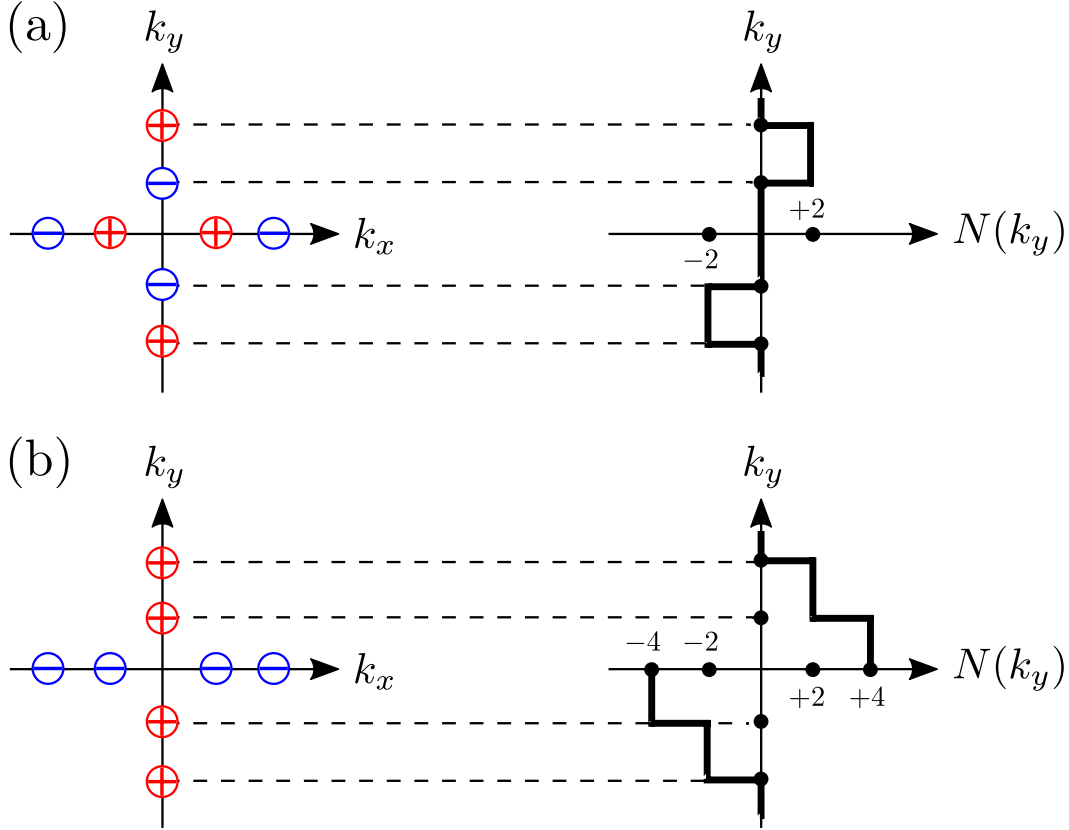
Figure 3.9: Schematic pictures of the relation between $W_{\mathcal{L}}$ (left) and $N(k_y)$ (right) in case of (a) opposite sign pair and (b) same sign pair states. Red and blue points indicate $W_{\mathcal{L}} = +2$ and -2, respectively.

to use a different substrate or doping carriers, for example with Te.

Nodal points with the nontrivial topological charges imply the existence of dispersionless in momentum parallel to an edge, Andreev bound states with flat band spectra at sample edges. References [16, 35] showed that the number of Andreev flat band is related to the one-dimensional winding number $N(\boldsymbol{k}_{\parallel})$ defined by

$$N\left(\boldsymbol{k}_{\parallel}\right) = \int \, d\boldsymbol{k}_{\perp} \cdot \mathrm{Tr}\left[q^{-1}(\boldsymbol{k})\nabla_{\boldsymbol{k}_{\perp}}q(\boldsymbol{k})\right], \qquad (3.17)$$

where $\boldsymbol{k}_{\parallel}$ ($\boldsymbol{k}_{\perp}$) is momentum parallel (perpendicular) to the surface. We now consider the case that edges running along the y-direction and then $\boldsymbol{k}_{\parallel} = (0, k_y)$ and $\boldsymbol{k}_{\perp} = (k_x, 0)$. Figure 3.9 shows that the relation between the one-dimensional winding number $N(k_y)$ and the topological charge $W_{\mathcal{L}}$ defined in Eq. 3.11. Figure 3.9 (a) shows in the case of opposite sign pair states is nonzero $|N(k_y)|$ for k_y between the nodal points if their topological charges have opposite signs. In the case of same sign pair states $|N(k_y)|$ is nonzero for all momenta between the outermost nodal points (Figure 3.9 (b)).

For further investigation, we introduce a lattice model corresponding to the BdG Hamiltonian in Eq. (3.2). We replace $k_i \to \sin k_i$ and $\left(k_x^2 + k_y^2\right)/(2m) \to 2t\left(2 - \cos k_x - \cos k_y\right)$

with $t = (2m)^{-1}$ in Eq. (3.2) and use $A_{i\sigma}$ and $B_{i\sigma}$ for annihilation operators of two orbitals, spin $\sigma = \uparrow$ and $\downarrow$ electron at $\boldsymbol{i}$. We divide $\mathcal{H}$ into three parts, s$\mathcal{H}_0$, $\mathcal{H}_{\text{SOC}}$ and $\mathcal{H}_\Delta$, and they are given by

$$
\begin{aligned}
\mathcal{H}_0 = & -t \sum_{\langle \boldsymbol{i,j}\rangle,\sigma} \left(A_{i\sigma}^\dagger A_{j\sigma} + B_{i\sigma}^\dagger B_{j\sigma} \right) - (\mu - 4t) \sum_{i,\sigma} \left[A_{i\sigma}^\dagger A_{i\sigma} + B_{i\sigma}^\dagger B_{i\sigma} \right] \\
& + \frac{a}{4} \sum_{i,\sigma} \left(A_{i\sigma}^\dagger A_{i+\boldsymbol{x}+\boldsymbol{y}\sigma} + A_{i+\boldsymbol{x}+\boldsymbol{y}\sigma}^\dagger A_{i\sigma} - \left(A_{i\sigma}^\dagger A_{i+\boldsymbol{x}-\boldsymbol{y}\sigma} + A_{i+\boldsymbol{x}-\boldsymbol{y}\sigma}^\dagger A_{i\sigma} \right) \right) \\
& - \frac{a}{4} \sum_{i,\sigma} \left[B_{i\sigma}^\dagger B_{i+\boldsymbol{x}+\boldsymbol{y}\sigma} + B_{i+\boldsymbol{x}+\boldsymbol{y}\sigma}^\dagger B_{i\sigma} - \left(B_{i\sigma}^\dagger B_{i+\boldsymbol{x}-\boldsymbol{y}\sigma} + B_{i+\boldsymbol{x}-\boldsymbol{y}\sigma}^\dagger B_{i\sigma} \right) \right], \quad (3.18)
\end{aligned}
$$

$$
\begin{aligned}
\mathcal{H}_{\text{SOC}} = & -\frac{v_{\text{so}}}{2} \sum_i \left[\left(A_{i\uparrow}^\dagger B_{i+\boldsymbol{x}\downarrow} - A_{i+\boldsymbol{x}\uparrow}^\dagger B_{i\downarrow} \right) - \left(A_{i\downarrow}^\dagger B_{i+\boldsymbol{x}\uparrow} - A_{i+\boldsymbol{x}\downarrow}^\dagger B_{i\uparrow} \right) \right. \\
& \left. + \left(B_{i\uparrow}^\dagger A_{i+\boldsymbol{x}\downarrow} - B_{i+\boldsymbol{x}\uparrow}^\dagger A_{i\downarrow} \right) - \left(B_{i\downarrow}^\dagger A_{i+\boldsymbol{x}\uparrow} - B_{i+\boldsymbol{x}\downarrow}^\dagger A_{i\uparrow} \right) \right] \\
& + \frac{v_{\text{so}}}{2i} \sum_i \left[\left(A_{i\uparrow}^\dagger B_{i+\boldsymbol{y}\downarrow} - A_{i+\boldsymbol{y}\uparrow}^\dagger B_{i\downarrow} \right) + \left(A_{i\downarrow}^\dagger B_{i+\boldsymbol{y}\uparrow} - A_{i+\boldsymbol{y}\downarrow}^\dagger B_{i\uparrow} \right) \right. \\
& \left. + \left(B_{i\uparrow}^\dagger A_{i+\boldsymbol{y}\downarrow} - B_{i+\boldsymbol{y}\uparrow}^\dagger A_{i\downarrow} \right) + \left(B_{i\downarrow}^\dagger A_{i+\boldsymbol{y}\uparrow} - B_{i+\boldsymbol{y}\downarrow}^\dagger A_{i\uparrow} \right) \right], \quad (3.19)
\end{aligned}
$$

$$
\begin{aligned}
\mathcal{H}_\Delta = & -\frac{\Delta_2}{4k_0^2} \sum_i \left[\left(A_{i\uparrow}^\dagger A_{i-\boldsymbol{x}-\boldsymbol{y}\downarrow}^\dagger + A_{i\uparrow}^\dagger A_{i+\boldsymbol{x}+\boldsymbol{y}\downarrow}^\dagger \right) - \left(A_{i\uparrow}^\dagger A_{i-\boldsymbol{x}+\boldsymbol{y}\downarrow}^\dagger + A_{i\uparrow}^\dagger A_{i+\boldsymbol{x}-\boldsymbol{y}\downarrow}^\dagger \right) \right. \\
& \left. - \left(A_{i\downarrow}^\dagger A_{i-\boldsymbol{x}-\boldsymbol{y}\uparrow}^\dagger + A_{i\downarrow}^\dagger A_{i+\boldsymbol{x}+\boldsymbol{y}\uparrow}^\dagger \right) + \left(A_{i\downarrow}^\dagger A_{i-\boldsymbol{x}+\boldsymbol{y}\uparrow}^\dagger + A_{i\downarrow}^\dagger A_{i+\boldsymbol{x}-\boldsymbol{y}\uparrow}^\dagger \right) \right] \\
& - \frac{\Delta_2}{4k_0^2} \sum_i \left[\left(B_{i\uparrow}^\dagger B_{i-\boldsymbol{x}-\boldsymbol{y}\downarrow}^\dagger + B_{i\uparrow}^\dagger B_{i+\boldsymbol{x}+\boldsymbol{y}\downarrow}^\dagger \right) - \left(B_{i\uparrow}^\dagger B_{i-\boldsymbol{x}+\boldsymbol{y}\downarrow}^\dagger + B_{i\uparrow}^\dagger B_{i+\boldsymbol{x}-\boldsymbol{y}\downarrow}^\dagger \right) \right. \\
& \left. - \left(B_{i\downarrow}^\dagger B_{i-\boldsymbol{x}-\boldsymbol{y}\uparrow}^\dagger + B_{i\downarrow}^\dagger B_{i+\boldsymbol{x}+\boldsymbol{y}\uparrow}^\dagger \right) + \left(B_{i\downarrow}^\dagger B_{i-\boldsymbol{x}+\boldsymbol{y}\uparrow}^\dagger + B_{i\downarrow}^\dagger B_{i+\boldsymbol{x}-\boldsymbol{y}\uparrow}^\dagger \right) \right] \\
& + \Delta_0 \sum_i \left[\left(A_{i\uparrow}^\dagger A_{i\downarrow}^\dagger - A_{i\downarrow}^\dagger A_{i\uparrow}^\dagger \right) - \left(B_{i\uparrow}^\dagger B_{i\downarrow}^\dagger - B_{i\downarrow}^\dagger B_{i\uparrow}^\dagger \right) \right] \\
& + \text{ h.c.}. \quad (3.20)
\end{aligned}
$$

This system has a cylindrical geometry with two edges at $i_x = 1$ and N_x in the x-direction and periodic in the y-direction. We numerically diagonalize this Hamiltonian for each k_y and examine edge states. We set $N_x = 10000$ and Figure 3.10 shows the energy spectra for the four sets of parameters: (a) no nodal points, (b), (c) opposite sign pair states and (d) same sign pair states. Without nodal points, we do not have Andreev flat band. Once nodal points appear, flat band states also appear. In cases of opposite sign pair states (b) and (c), flat bands exist at $E = 0$ between the two nodal points that have opposite topological charges, and the number of the flat band states is two for each edge. On the other hand, in the case of (d) same sign pair state, flat bands exist in a part including $k_y = 0$. Four flat band states cross $k_y = 0$ and two of them terminate at each of the two nodal points. Thus, the number of flat band states is identical with $|N(k_y)|$ as shown in Fig. 3.9. Strictly speaking, in Fig. 3.10 (d) the gap at $k_y = 0$ is finite, but this is due to the finite size effect and not intrinsic. We have confirmed that there is no gap at $k_y = 0$ by using the recursive Green's function method explained in Appendix B.
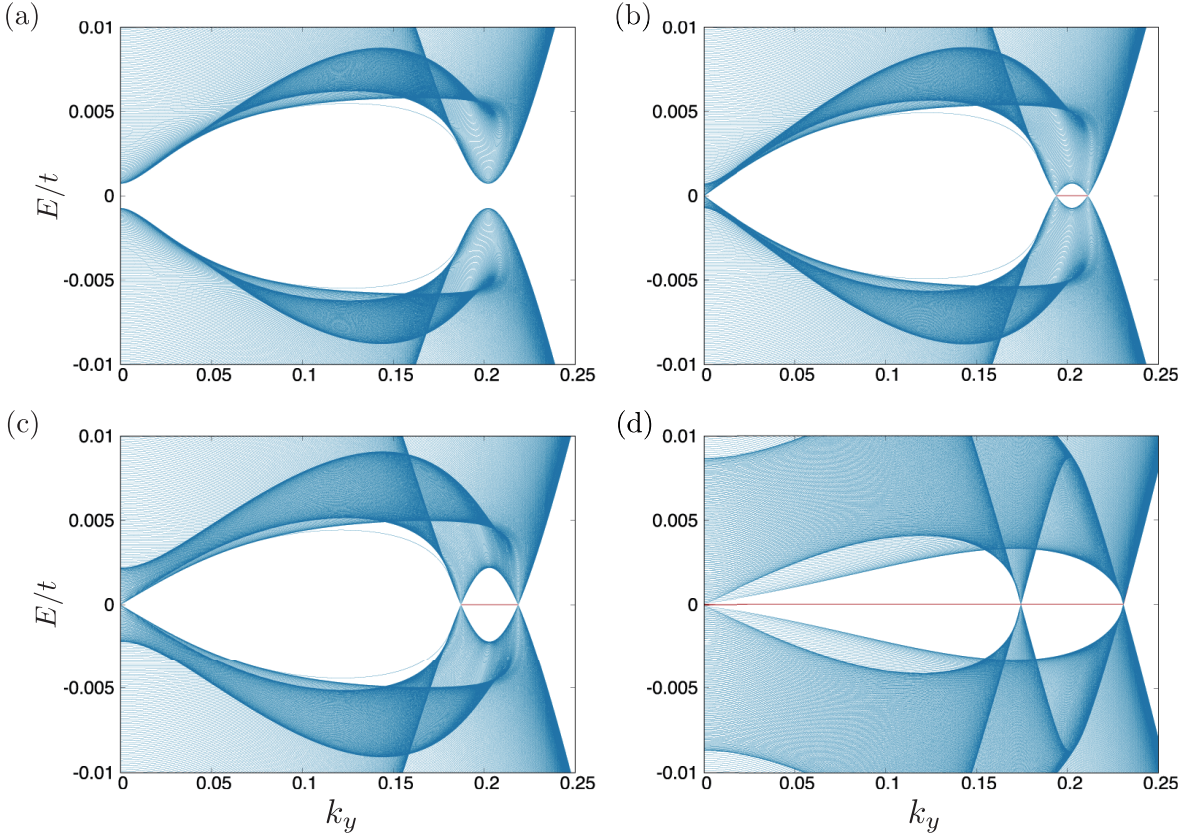
Figure 3.10: Energy spectra for (a) no nodal points (b) opposite sign pair (c) opposite sign pair (d) same sign pair states. We set the parameters as $(v_{\rm so}[{\rm meV\mathring{A}}], \Delta_0[{\rm meV}], \Delta_2[{\rm meV}]) =$ (a) $(50, 11, -1.5)$, (b) $(60, 11, -1.5)$, (c) $(70, 11, -1.5)$ and (d) $(80, 4, -10)$. The vertical axis is scaled by $t = (2m)^{-1}$.

In experiments, boundaries may be misaligned. It is worth mentioning their effects on the distinct topological phases and the resultant anisotropy of the number of Andeev flat bands. The relation of the number of flat bands and $\left| N\left(k_\parallel\right) \right|$ is also useful for the case of edge not parallel to $(1, 0)$ and or $(0, 1)$ direction. For instance, consider edges along $(1, 1)$ direction and denote the parallel component of wave vector $k_\parallel$. Figure 3.11 (a) and (b) show the 1D winding number $\left| N\left(k_\parallel\right) \right|$ and the topological charge $W_{\mathcal{L}}$ for the case opposite sign pair and same sign pair state, respectively. For both cases $N\left(k_\parallel\right) = 0$ for any $k_\parallel$, and therefore, no Andreev flat band appear.

Finally, we note that one should take into account the interaction effects for the bound states. It has been pointed out that they are susceptible to surface instabilities due to a large density of states intrinsic to flat bands [35, 79]. The most likely candidate is edge ferromagnetism, which spits the flat bands [79]. Such a surface instability is seen in tunneling spectroscopy experiments in the cuprate superconductor YBa$_2$Cu$_3$O$_7$, and the zero-bias conductance peak split below the edge transition temperature, approximately $0.1T_c$ [80]. We leave the study of possible edge instabilities to future work.
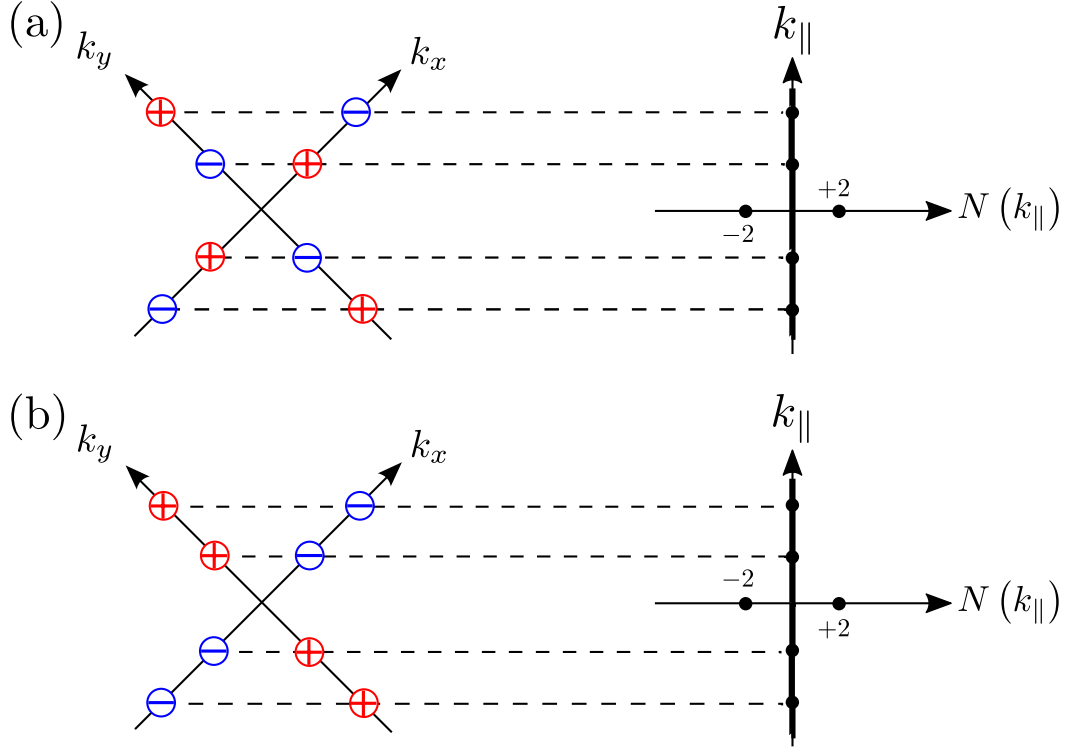
Figure 3.11: Schematic pictures of the relation between $W_\mathcal{L}$ (left) and $N(k_\parallel)$ (right) in case of (a) opposite sign pair and (b) same sign pair states. We consider the edges running along $(1,1)$ direction. Red and blue points indicate $W_\mathcal{L} = +2$ and -2, respectively.

3.4 Effects of in-plane Zeeman field

A recent study shows in-plane Zeeman field induces gapless superconductivity with a partial Fermi surface in two-dimensional spin-orbit-coupled electron systems [81]. Motivated by this study and in order to obtain more information about the gap nodes, we examine the effect of in-plane Zeeman field. The Zeeman field splits the band and breaks the time-reversal symmetry. Here, we assume the Zeeman field applied to the x-direction, the corresponding Hamiltonian is $H_Z^x = -h_x \Gamma_z \tau_0 \sigma_x$.

In order to understand when gap nodes arise, we examine the energy dispersion along the nodal direction $k_x = 0$ and $k_y = 0$. The quasiparticle dispersions for positive energy are

$$E_\pm(\boldsymbol{k}) = \left| \sqrt{\epsilon_0(\boldsymbol{k})^2 + \Delta_z^2} \pm \sqrt{\gamma_x(\boldsymbol{k})^2 + h_x^2} \right| \quad \text{(for } \boldsymbol{k} = (k_x, 0)) \tag{3.21}$$

where each $E_\pm(\boldsymbol{k})$ value is doubly degenerate and

$$E_{\pm\pm}(\boldsymbol{k}) = \left| \sqrt{\epsilon_0^2(\boldsymbol{k}) + \Delta_z^2} \pm \gamma_y(\boldsymbol{k}) \pm h_x \right| \quad \text{(for } \boldsymbol{k} = (0, k_y)). \tag{3.22}$$

Consequently, nodes appear on the k_x axis for $\sqrt{\gamma_x^2 + h_x^2} > \Delta_z$ and on the k_x axis for $|\gamma_y| + |h_x| > \Delta_0$. It is worth pointing out that the nodes can appear even when the spin-orbit

coupling is weak. However, since the Hamiltonian does not belong to the symmetry class DIII, we cannot apply the analysis of Section 3.3 and their nodes are not characterized by $2\mathbb{Z}$ invariant Eq. (3.11). In this section, we give the topological charges for such nodes.

Figure 3.12 shows the line and points nodes when the in-plane field is applied. Panels (a)-(c) are the case of weak spin-orbit coupling, $v_{\text{so}} = 12$ meV Å. In this case, strong in-plane Zeeman field h_x expands nodal lines. Once the expanded nodal lines touch each other, nodal points appear on the k_x axis (Panel (b)). Figure 3.13 shows that the quasiparticle dispersions along the k_y and k_x axis in the case of Fig 3.12(b). Stronger field annihilates the nodal points by touching the nodal lines (Panel (c)). Panels (d)-(f) are the case of strong spin-orbit coupling, $v_{\text{so}} = 80$ meV Å. As we mentioned in the previous section, the strong spin-orbit coupling makes the nodal points. Once in-plane Zeeman field h_x is applied, the nodal points on the k_y axis are inflated and form the nodal lines (Panel (d)). However, the nodal points in k_x axis still remain until the nodal lines touch each other in k_x axis (Panel (f)).

Let us discuss these nodal lines and points from viewpoint of symmetry. The Hamiltonian has another symmetry related to the spatial inversion. We define the inversion operator I as $I = \Gamma_0 \tau_z \sigma_0$, and then

$$IH(\boldsymbol{k})I^{-1} = H(-\boldsymbol{k}). \tag{3.23}$$

The inversion operator I is unitary and $I^2 = \mathbb{1}$. In the presence of the inversion symmetry, the AZ $+ \, \mathcal{I}$ classification [36] can be applied (See also Section 2.2.3). We discuss the line and point nodes based on this classification.

$\mathbb{Z}_2$ line charge

We show that the line nodes can be characterized by a $\mathbb{Z}_2$ invariant [37, 39]. Combining with C and I,

$$(CI)\, H(\boldsymbol{k})\, (CI)^{-1} = -H(\boldsymbol{k}). \tag{3.24}$$

and $(CI)^2 = +1$. One can find a unitary operator Ω which transforms $H(\boldsymbol{k})$ as anti-symmetric matrix. Define $U_{CI} \equiv U_C U_I = \Gamma_x \tau_z \sigma_0$ where $U_C = \Gamma_x \tau_0 \sigma_0$ and $U_I = \Gamma_0 \tau_z \sigma_0$, and then,

$$U_{CI}H(\boldsymbol{k})^T U_{CI}^\dagger = -H(\boldsymbol{k}). \tag{3.25}$$

Becaouse U_{CI} is real symmetric, it can be diagonalized as

$$U_{CI} = Q\Lambda Q^T, \tag{3.26}$$

where Q is a unitary matrix and $\Lambda = \text{diag} \ (\lambda_1, \cdots, \lambda_8)$ with $|\lambda_j| = 1$ for all j's. Inserting this into above,

$$Q\Lambda Q^T H(\boldsymbol{k})^T Q^* \Lambda^\dagger Q^\dagger = -H(\boldsymbol{k}). \tag{3.27}$$

Since Λ is diagonal, its square root can be defined, $\sqrt{\Lambda} = \text{diag} \ (\sqrt{\lambda_1}, \cdots, \sqrt{\lambda_8})$ and it is easy to show the following relation,

$$\left(\sqrt{\Lambda}^\dagger Q^\dagger H(\boldsymbol{k}) Q \sqrt{\Lambda} \right)^T = -\sqrt{\Lambda}^\dagger Q^\dagger H(\boldsymbol{k}) Q \sqrt{\Lambda}. \tag{3.28}$$
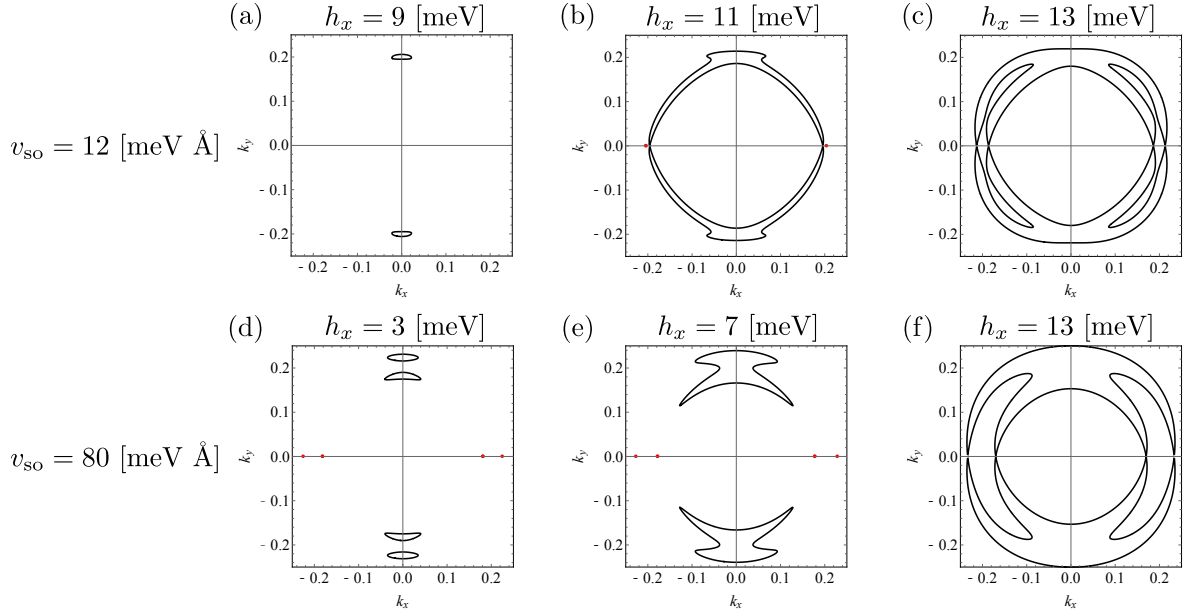
Figure 3.12: Line and points nodes with varying in-plane field h_x. The solid lines represent line nodes. The red points in (b), (d) and (e) represent position of nodal points. Spin-orbit coupling is (a-c) $v_{\text{so}} =$ 12 [meV Å] and (d-f) 80 [meV Å].
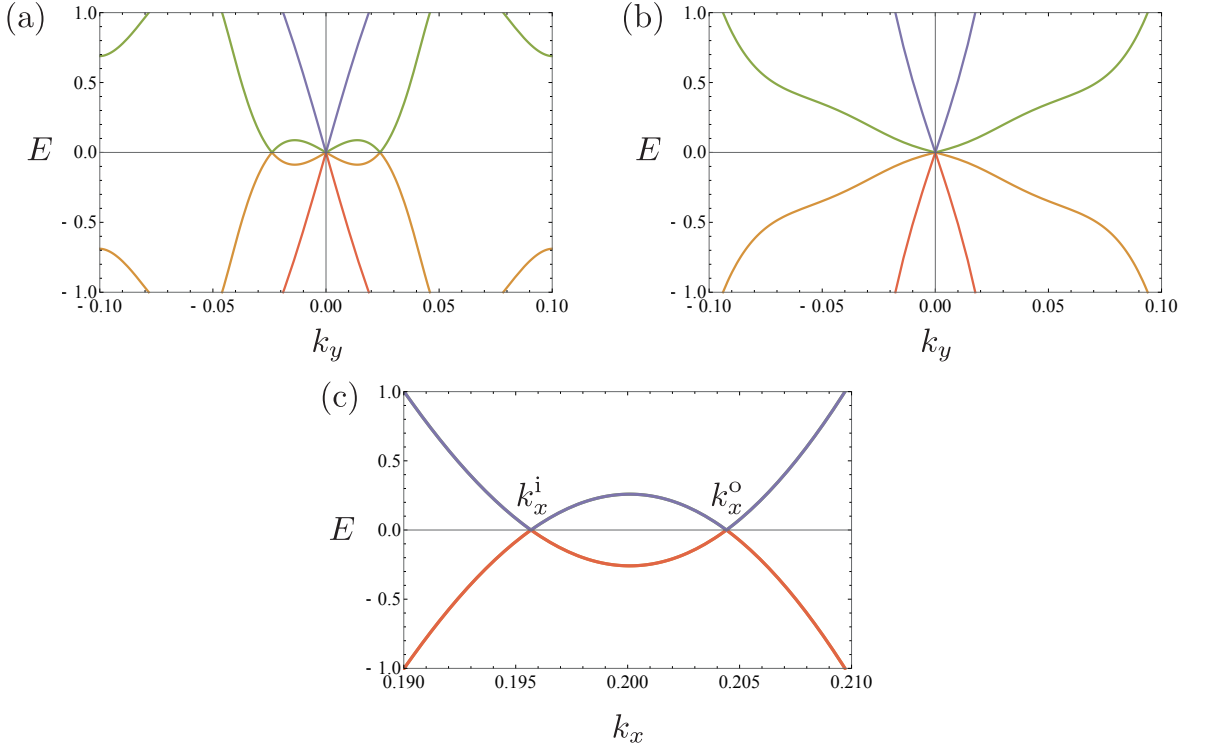

Figure 3.13: Energy dispersion along the k_y axis at $k_x = k_x^{\text{i}}$ (a) and k_x^{o} (b) and along the k_x axis at $k_y = 0$ (c). Note that there are doubly degenerate along the k_x axis and $|E| \approx 20$ for the other four bands. The parameters are $v_{\text{so}} = 12$ [meV Å] and $h_x = 11$ [meV] same as Fig 3.12(b).
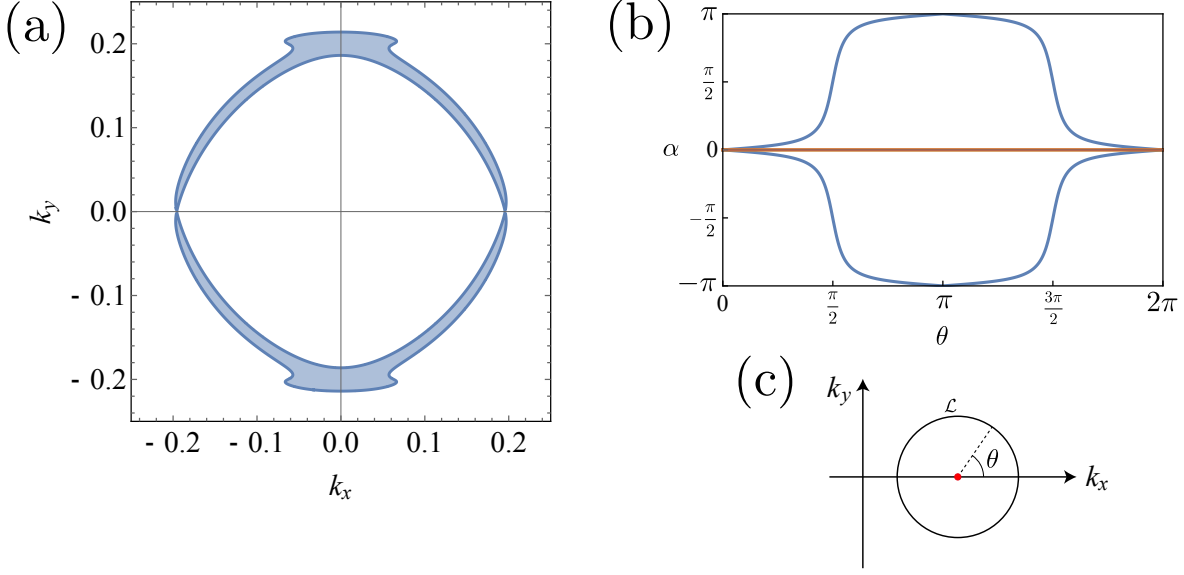
Figure 3.14: $\mathbb{Z}_2$ invariant for (a) line and (b) point nodes. (a) The region of $P(\boldsymbol{k}) < 0$. (b) Phases (blue and red lines) of the eigenvalues $\tilde{Q}(\boldsymbol{k})$ in Eq. (3.41) along the contour $\mathcal{L}$ (shown in (c)) encircling a nodes. Each color line is pair of the eigenvalues. The blue (red) lines indicate the presence of a nontrivial (trivial) topological charge. The parameters are $v_{\rm so} = 12$ [meV Å] and $h_x = 11$ [meV] same as Fig 3.12(b).

Hence, an anti-symmetric matrix is given by $\tilde{H}(\boldsymbol{k}) = \Omega^\dagger H(\boldsymbol{k})\Omega$ where the unitary operator $\Omega = Q\sqrt{\Lambda}$. For each line node, we can define a $\mathbb{Z}_2$ invariant $(-1)^l$ with the sign of Pfaffian $P(\boldsymbol{k}) = {\rm sgn}\left[{\rm Pf}\ \tilde{H}(\boldsymbol{k})\right]$,

$$(-1)^l = P(\boldsymbol{k}_-)P(\boldsymbol{k}_+), \tag{3.29}$$

where $\boldsymbol{k}_+$ $(\boldsymbol{k}_-)$ is momenta inside (outside) of line nodes. Figure 3.14(a) shows the region of $P(\boldsymbol{k}) < 0$. Therefore, each line node has $\mathbb{Z}_2$ invariant (-1) in this case.

$\mathbb{Z}_2$ point charge

Next, we show that the point nodes are also characterized by a $\mathbb{Z}_2$ invariant [36, 39]. Even when in-plane Zeeman field is applied, one can define the pseudo-time-reversal operator as $\tilde{T} = M_z T I$. Here $M_z = \Gamma_z \tau_z (i\sigma_z)$ is the mirror operator, and acts as

$$M_z H(\boldsymbol{k}) M_z^{-1} = H(\boldsymbol{k}). \tag{3.30}$$

Then, the pseudo-time-reversal operator $\tilde{T} = \Gamma_z \tau_0 (i\sigma_x) K$ acts as

$$\tilde{T} H(\boldsymbol{k}) \tilde{T}^{-1} = H(\boldsymbol{k}). \tag{3.31}$$

Notice that this pseudo-time-reversal operator $\tilde{T}$ does not link the momentum $\boldsymbol{k}$ to $-\boldsymbol{k}$ and impose a *local* constraint in $\boldsymbol{k}$ space. Since $\tilde{T}^2 = +1$ and $(CI)^2 = +1$, this Hamiltonian belongs to the symmetry class BDI in AZ + $\mathcal{I}$ classification [36] and a topological charge is

defined as a $\mathbb{Z}_2$ invariant. While one can define the *second* chiral operator $\tilde{S} = -i\tilde{T}CI$ and a related $\mathbb{Z}$ invariant winding number as in Eq. (3.11), this $\mathbb{Z}$-invariant winding number is zero in this case. This is because class BDI in AZ + $\mathcal{I}$ classification has only $\mathbb{Z}_2$ invariants (See Table 2.4.)

We now show that the point nodes in the in-plane Zeeman field have a nontrivial $\mathbb{Z}_2$ invariant. Since $H(\boldsymbol{k})$ anticommutes with $\tilde{S}$, it is written in the form of Eq. (3.9) with the off-diagonal block

$$
\begin{aligned}
\tilde{q}(\boldsymbol{k}) = & \; \epsilon_0\left(\boldsymbol{k}\right)\tau_0\sigma_0 + \gamma_{xy}\left(\boldsymbol{k}\right)\tau_z\sigma_0 + \gamma_x\left(\boldsymbol{k}\right)\tau_x\sigma_y + \gamma_y\left(\boldsymbol{k}\right)\tau_x\sigma_x - h_x\tau_0\sigma_x \\
& +i\left(\Delta_d\left(\boldsymbol{k}\right)\tau_z + \Delta_z\left(\boldsymbol{k}\right)\tau_0\right)\sigma_z.
\end{aligned}
\tag{3.32}
$$

It is instructive to define the corresponding flat band Hamiltonian [7] following Ref. [35]. The Hamiltonian $H(\boldsymbol{k})$ is diagonalized as

$$
\begin{bmatrix} 0 & \tilde{q}(\boldsymbol{k}) \\ \tilde{q}^\dagger(\boldsymbol{k}) & 0 \end{bmatrix} \begin{bmatrix} \chi_i^\pm(\boldsymbol{k}) \\ \eta_i^\pm(\boldsymbol{k}) \end{bmatrix} = \pm\lambda_i\left(\boldsymbol{k}\right) \begin{bmatrix} \chi_i^\pm(\boldsymbol{k}) \\ \eta_i^\pm(\boldsymbol{k}) \end{bmatrix},
\tag{3.33}
$$

where $i(= 1, 2, 3, 4)$ is the index of eigenvalues such that $0 \le \lambda_1 \le \lambda_2 \le \lambda_3 \le \lambda_4$. Multiplying Eq. (3.33) by $H(\boldsymbol{k})$ one more time, we obtain a pair of 4-dimensional eigenvalue equations

$$
\tilde{q}(\boldsymbol{k})\tilde{q}^\dagger(\boldsymbol{k})\chi_i^\pm(\boldsymbol{k}) = \lambda_i^2(\boldsymbol{k})\chi_i^\pm(\boldsymbol{k}),
\tag{3.34}
$$

$$
\tilde{q}^\dagger(\boldsymbol{k})\tilde{q}(\boldsymbol{k})\eta_i^\pm(\boldsymbol{k}) = \lambda_i^2(\boldsymbol{k})\eta_i^\pm(\boldsymbol{k})
\tag{3.35}
$$

Therefore, the eigenfunctions $\left[\chi_i^\pm(\boldsymbol{k}), \; \eta_i^\pm(\boldsymbol{k})\right]$ is obtained from the eigenvectors of $\tilde{q}(\boldsymbol{k})\tilde{q}^\dagger(\boldsymbol{k})$ or $\tilde{q}^\dagger(\boldsymbol{k})\tilde{q}(\boldsymbol{k})$:

$$
\tilde{q}(\boldsymbol{k})\tilde{q}^\dagger(\boldsymbol{k})u_i(\boldsymbol{k}) = \lambda_i^2(\boldsymbol{k})u_i(\boldsymbol{k}),
\tag{3.36}
$$

$$
\tilde{q}^\dagger(\boldsymbol{k})\tilde{q}(\boldsymbol{k})v_i(\boldsymbol{k}) = \lambda_i^2(\boldsymbol{k})v_i(\boldsymbol{k}).
\tag{3.37}
$$

The eigenvectors $\{u_i(\boldsymbol{k})\}$ and $\{v_i(\boldsymbol{k})\}$ are normalized. One can easily check that $\{v_i(\boldsymbol{k})\}$ are obtained from

$$
v_i(\boldsymbol{k}) = \frac{1}{\lambda_i}\tilde{q}^\dagger(\boldsymbol{k})u_i(\boldsymbol{k}).
\tag{3.38}
$$

Hence, the eigenfunctions $\left[\chi_i^\pm(\boldsymbol{k}), \; \eta_i^\pm(\boldsymbol{k})\right]$ are

$$
\begin{bmatrix} \chi_i^\pm(\boldsymbol{k}) \\ \eta_i^\pm(\boldsymbol{k}) \end{bmatrix} = \frac{1}{\sqrt{2}}\begin{bmatrix} u_i(\boldsymbol{k}) \\ \pm v_i(\boldsymbol{k}) \end{bmatrix} = \frac{1}{\sqrt{2}}\begin{bmatrix} u_i(\boldsymbol{k}) \\ \pm\tilde{q}^\dagger(\boldsymbol{k})u_i(\boldsymbol{k})/\lambda_i \end{bmatrix}.
\tag{3.39}
$$

Next, we define the flat band Hamiltonian as $Q(\boldsymbol{k}) = \mathbb{1} - 2P(\boldsymbol{k})$ with the projector $P(\boldsymbol{k})$ onto the filled Bloch states [7],

$$
Q(\boldsymbol{k}) = \sum_i \begin{bmatrix} 0 & u_i(\boldsymbol{k})v_i^\dagger(\boldsymbol{k}) \\ v_i(\boldsymbol{k})u_i(\boldsymbol{k})^\dagger & 0 \end{bmatrix} = \sum_i \begin{bmatrix} 0 & u_i(\boldsymbol{k})u_i^\dagger(\boldsymbol{k})\frac{\tilde{q}(\boldsymbol{k})}{\lambda_i(\boldsymbol{k})} \\ \frac{\tilde{q}^\dagger(\boldsymbol{k})}{\lambda_i(\boldsymbol{k})}u_i(\boldsymbol{k})u_i(\boldsymbol{k})^\dagger & 0 \end{bmatrix}
\tag{3.40}
$$

Therefore, it is again represented in the form of Eq. (3.9) and the off-diagonal block of $Q(\boldsymbol{k})$ reads

$$
\tilde{Q}(\boldsymbol{k}) = \sum_i \frac{1}{\lambda_i(\boldsymbol{k})}u_i(\boldsymbol{k})u_i^\dagger(\boldsymbol{k})\tilde{q}(\boldsymbol{k}).
\tag{3.41}
$$

and this 4×4 matrix is not hermitian.

The topological charge of the point nodes in the class BDI is determined by tracking the eigenvalues of $\tilde{Q}(\boldsymbol{k})$ [36]. The eigenvalues of $\tilde{Q}(\boldsymbol{k})$ are two complex conjugate pairs $\pm e^{i\alpha}$ and their phases α may have a nontrivial winding along the contour $\mathcal{L}$ encircling a node. Figure 3.14(b) shows that phases of two pairs of the eigenvalues of $\tilde{Q}(\boldsymbol{k})$ around a nodal point in case of $v_{\mathrm{so}} = 12$ meV Å and $h_x = 11$ meV, where one nodal point exists on positive k_x axis (see Fig. 3.12(b)). The phases of one pair point touch $-\pi$ or π and this indicates a nontrivial winding around $\mathcal{L}$. In general our eight-band model (including particle-hole space), this winding number conserves only its parity since the pair of $\pm\pi$ crossings is allowed to annihilate [36]. Therefore, the nodal point has this $\mathbb{Z}_2$ topological charge. ($\mathbb{Z}_2$ topological charge) $= (-1)^{\mathrm{N}_\pi}$ where N_π is the number of π touching points. Notice that the nodal point can be inflated and mutate into a $\mathbb{Z}_2$ line node by tilting Zeeman field. The line node inherits a $\mathbb{Z}_2$ topological charge of the nodal point.

Finally, we remark that the nodal points originating from strong spin-orbit coupling without Zeeman field have two types of topological charges: $\mathbb{Z}$ topological charges defined in Eq. (3.11) and nontrivial $\mathbb{Z}_2$ charge defined from the eigenvalues of $\tilde{Q}(\boldsymbol{k})$.

3.5   Conclusion

We have discussed in this chapter the gap nodes in monolayer FeSe on SrTiO$_3$ substrate from a topological perspective. We have employed the effective two-orbital model which includes two types of superconducting pairing: orbitally trivial with usual d-wave anisotropy and orbitally nontrivial isotropic one. With this model, we have examined the evolution with increasing spin-orbit coupling from the experimentally observed nodeless state to a nodal state from a viewpoint of topology. We have shown that this evolution depends strongly on the orbital degrees of freedom in Cooper pairs. Our work highlights the annihilation of gap nodes due to spin-orbit coupling and demonstrates that the nodal charge is protected by a chiral symmetry.

If the interband spin-orbit coupling is controlled to be sufficiently strong by using different substrates or carriers doping for example with Te, nodal points appear with carrying $2\mathbb{Z}$ topological charges. We have found that the momentum-space distribution of the topological charges depends strongly on the orbital character of the pairing as shown in Fig. 3.7. When the orbitally trivial pairing is dominant, the adjacent pair of nodal points each axis have topological charges with the same sign (same sign pair state). On the other hand, when the orbitally nontrivial pairing is dominant, their topological charges have opposite signs (opposite sign pair state). In the latter case, the nodal points can merge and are annihilated directly with decreasing interband spin-orbit coupling, because they have opposite topological charges. However, in the case of same sign pair states, nodal points cannot annihilate directly. We have found that this annihilation occurs through an involved mechanism. As the interband spin-orbit coupling decreases, two nodal points are created near the old nodal point. As the spin-orbit coupling further decreases, one nodal point stays while two nodal points move off the k_x- or k_y-axis. With decreasing the spin-orbit coupling, they continue to move and annihilate in pairs with other nodes having moved from another direction. The nodal points with the nontrivial topological charges imply the existence of Andreev band states that are dispersionless in the direction parallel to a sample edge. We have shown that Andreev flat band spectra differ between the cases of same sign and opposite sign pair state.

We also considered Zeeman coupling to examine the effects of broken time-reversal symmetry. In this case, we have found that line and point nodes can appear even when the spin-orbit coupling is weak. We have discussed these nodes from viewpoint of symmetry and found that they are topologically protected by a $\mathbb{Z}_2$ invariant.

Chapter 4

Bogoliubov Fermi surfaces in UPt$_3$

Multi-orbital superconductors with even-parity and broken time-reversal symmetry may have a Fermi surface of Bogoliubov quasiparticles at zero energy, which we call Bogoliubov Fermi surface. Bogoliubov Fermi surface is topologically protected and we apply this idea to heavy-fermion superconductor UPt$_3$. With symmetry consideration, we propose the paring of mixture of spin-singlet d-wave, spin-triplet in-plane p- and out-of-plane f-waves that belong to the two-dimensional representation E_{1g} in the point group D_{6h}. We show that a finite in-plane p-wave pairing amplitude gives rise to the Bogoliubov Fermi surfaces and finite density of states at zero energy. We further calculate the temperature dependence of thermal conductivity κ by using the Boltzmann theory with relaxation time approximation and show that the Bogoliubov Fermi surfaces explain for the finite κ/T and anisotropy of thermal conductivity observed around $T = 0$.

4.1 Introduction

4.1.1 Multicomponent superconductor UPt$_3$

The uranium superconductor UPt$_3$ has attracted attention over more than two decades due to its multiple superconducting phases [82]. Experimental data of specific heat [83–85] and ultrasonic velocity [86] support that the temperature and magnetic field phase diagram has three superconducting phases, A, B, and C as shown in Figure 4.1(a). It is believed [87] that a weak antiferromagnetic order below $T_N = 5$ K [88–90] splits the transition into two, $T_c^+ \sim 550$ mK and $T_c^- \sim 480$ mK. The C phase is stable under high magnetic field at low temperatures.

The pairing symmetry in UPt$_3$ is still under hot debate [82]. It is believed that the symmetry belongs to either one- or two-dimensional irreducible representation of the point group D_{6h} since this is the relevant point group of the space group $P6_3/mmc$ of the crystal structure. The multiple superconducting phases indicate that the order parameters belong to a two-dimensional representation (η_1, η_2): E_{1g} or E_{2g} (even-parity) or E_{1u} or E_{2u} (odd-parity). Let us choose the bases such that $(\eta_1, \eta_2) \propto (1, 0)$ in the A phase and $\propto (0, 1)$ in the C phase [82]. The weak antiferromagnetic order with modulation vector $\boldsymbol{Q} = (1/2, 0, 0)$ lowers the crystal symmetry from hexagonal to orthorhombic (D_{2h}), and reduces the two-dimensional representation of the point group D_{6h} to two one-dimensional representations. The transition temperature splits into two as a consequence [92, 93]. Muon spin rotation-
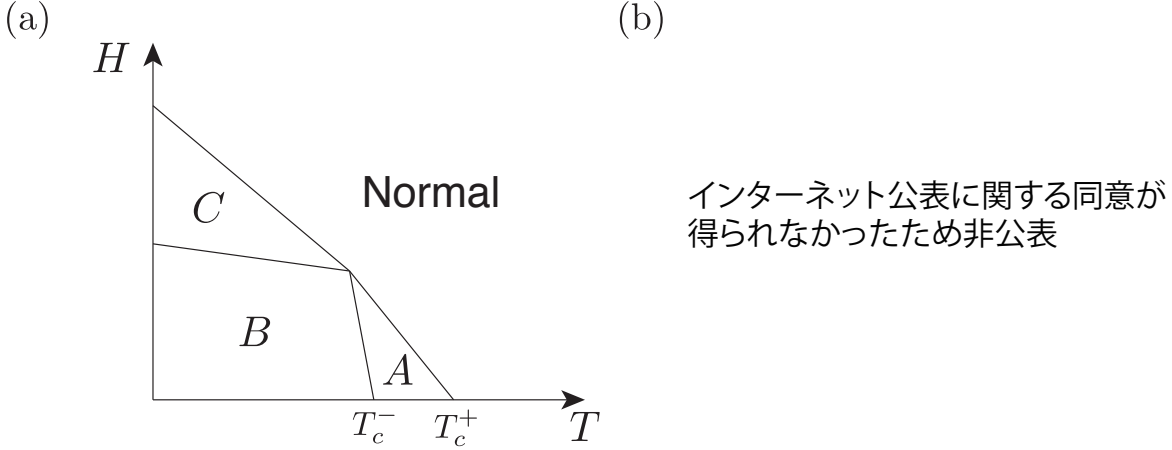
(a)

(b)

H

C

Normal

B

A

T_c^- T_c^+

T

インターネット公表に関する同意が
得られなかったため非公表

Figure 4.1: (a) Schematic phase diagram of UPt$_3$ in the space of temperature and magnetic field [82]. (b) Measurement of Kerr effect [40]. Kerr angle (red, left axis) and the real part of the mutual inductance (blue, right axis) are plotted as a function of temperature. The solid line is a guide to the eye of the polar Kerr angle $\theta_{\mathrm{K}} \propto \sqrt{\left[1 - \left(T_c^+/T_c\right)^2\right]\left[1 - \left(T_c^-/T_c\right)^2\right]}$ for $T < T_c^- \simeq T_{\mathrm{Ker}}$. θ_{K} is proportional to the square of the product of the real and imaginary components of the order parameter [91].

relaxation [94, 95] and polar Kerr effect experiments [40] show that the B phase breaks the time-reversal symmetry. This indicates a chiral pairing symmetry, $(\eta_1, \eta_2) \propto (1, i\eta)$ with real η. Figure 4.1(b) shows the result of polar Kerr effect [40]. The polar Kerr angle θ_{K} is proportional to the square of the product of the real and imaginary components of the order parameter [91].

The gap nodes structure of UPt$_3$ has been studied by thermal conductivity [96, 97], NMR $1/T_1$ [98], specific heat [85, 99], penetration depth [100, 101]. Table 4.1 lists the power-law temperature dependences of various quantities in the low-temperature regime predicted for polar and axial type gap functions. These results imply that the gap structure of UPt$_3$ is *hybrid* [102], i.e., the coexistence of line and point nodes. The first proposal of hybrid gap function is E_{1g} representation by Putikka and Joynt [103] and later by several authors [92, 93, 104]. Its spin part is singlet and its orbital part is d-wave: $\{k_z k_x, k_y k_z\}$, the gap has a line node in the basal plane and point nodes at the north and south poles of the Fermi surface in the normal-state. This is consistent with the observed power-law temperature dependences for various quantities in the low-temperature regime. However, this E_{1g} gap function is incompatible with the result of the nuclear magnetic relaxation (NMR) Knight shift [105], which implies spin-triplet pairing. Another plausible candidate is E_{2u} representation [106–109]. It is spin-triplet pairing and the $\boldsymbol{d}$ vector points along the c axis. This explains the anisotropy in the temperature dependence of upper critical field H_{c2} [110, 111]. Its orbital part is f-wave: $\left\{k_z \left(k_x^2 - k_y^2\right), 2k_x k_y k_z\right\}$, the gap also has a line node in the basal plane and the point nodes at the north and south poles. This state has the $\boldsymbol{d}$ vector pointing along the c axis due to strong spin-orbit coupling and can explain the anisotropy of H_{c2} [110, 111]. However, this E_{2u} representation is also incompatible with the result of Knight shift [105], which implies that the $\boldsymbol{d}$ vector has two spin directions. Recent field-orientation dependent thermal

Table 4.1: Temperature dependences of various quantities at low temperatures in UPt$_3$, and prediction for polar and axial type gap functions.

	UPt$_3$	Polar $\Delta_0 k_z$	Axial $\Delta_0 (k_x + i k_y)$
Thermal conductivity κ [96, 97]	T^2 (30 mK $< T$)	T^2	T^3
NMR $1/T_1$ [98]	T^3 (100 mK $< T$)	T^3	T^5
Specific heat C [85, 99]	T^2 (80 mK $< T <$ 300 mK)	T^2	T^3
Penetration depth $\lambda^{-2}(T) - \lambda^{-2}(0)$ [100, 101]	$\perp : T$ $\parallel : T^2$	$\perp : T$ $\parallel : T^3$	$\perp : T^4$ $\parallel : T^2$

conductivity experiments [112, 113] indicate another possibility, E_{1u} representation [114]. Its orbital part is another f-wave: $\left\{ k_x \left(5k_z^2 - 1 \right), k_y \left(5k_z^2 - 1 \right) \right\}$, and this predicts a vertical line node in both A and C phases, and two horizontal lines nodes in both B and C phases. The spin part of the E_{1u} representation has two candidates for the B phase, planar state $(\hat{y} k_x + \hat{z} k_y) \left(5k_z^2 - 1 \right)$ and chiral state $\hat{z} \left(k_x + i k_y \right) \left(5k_z^2 - 1 \right)$. It depends on whether the spin-orbit coupling is strong or not. The planer state is compatible with the result of Knight shift [105] since the $\boldsymbol{d}$ vector can change its orientation by magnetic field. On the other hand, in the chiral state, the $\boldsymbol{d}$ vector is pinned to along the c axis due to strong spin-orbit coupling, and this explains the anisotropy of H_{c2} [110, 111]. However, the field-angle variation of the specific heat experiment [115] did not observe any in-plane angular oscillation in any phase, while all the candidate gap functions E_{1g}, E_{1u}, and E_{2u} breaks the in-plane rotation symmetry. Table 4.2 summarizes candidate gap functions in the B phase.

Although several experiments have observed line node-like behaviors, Blount's theorem [116] implies the absence of line nodes in the spin-triplet two-dimensional representations since the line nodes are unstable against perturbations which preserve the symmetry of the system. Recently, Yanase adopted a generic order parameter in the E_{2u} representation taking account of nonsymmorphic crystal symmetry of UPt$_3$ and showed that at most 98 point nodes [41].

4.1.2 Thermal conductivity

Superconductors are perfect conductors of electronic current but poor conductors of heat current. In fact, the conventional superconductors are fully gapped and their thermal conductivity divided by temperature κ/T with approaching zero temperature due to no thermally excited quasiparticles [117]. However, the situation is different in unconventional superconductors with nodal gaps. The nonzero quasiparticle density of states is induced by impurities and this produces a finite residual κ/T even at $T = 0$ [118]. The residual κ/T at $T = 0$ which is called *universal* transport is theoretically pointed out first by Patrick Lee [119]

$$\lim_{T \to 0} \frac{\kappa(T)}{T} = \frac{\pi^2 k_B}{3} N_F v_F^2 \frac{a \hbar}{2 \mu \Delta_0}, \tag{4.1}$$

Table 4.2: Candidate gap functions in the B phase. All the candidate gap functions have horizontal line nodes and point nodes.

	chiral E_{1g} $k_z\,(k_x+ik_y)$	planar E_{1u} $(\hat{y}k_x+\hat{z}k_y)\,(5k_z^2-1)$	chiral E_{1u} $\hat{z}\,(k_x+ik_y)\,(5k_z^2-1)$	chiral E_{2u} $\hat{z}k_z\,(k_x+ik_y)^2$
Multi-component $\boldsymbol{d}$ vector [105]	No	Yes	No	No
Anisotropy of H_{c2} [110, 111]	No	?	Yes	Yes
Breaking of time-reversal symmetry [40, 94, 95]	Yes	No	Yes	Yes
Field-orientation dependent thermal conductivity [112, 113]	Yes	Yes	Yes	No
Field-angle dependence of the specific heat [115]	No	No	No	No

where N_F and v_F are the density of states and the velocity at the Fermi level, respectively. a is a coefficient of the order of unity which depends on the topology of the gap node [118]. Δ_0 is the is the maximum amplitude of the superconducting gap and the parameter μ is measured from the slope of the gap at node, and this is given by $\mu \equiv \frac{1}{\Delta_0}\frac{\partial\Delta(\phi)}{\partial\phi}$ where ϕ is the in-plane angle of the wave vector on circular Fermi surface. The *universal* transport is independent of impurity concentration because quasiparticle density and scattering rate both increase and cancel each other as impurity concentration increases. Indeed, this *universal* behavior was verified in the d-wave superconductor YBa$_2$Cu$_3$O$_7$ [120] and p-wave Sr$_2$RuO$_4$ [121].

The thermal conductivity in UPt$_3$ was measured by several groups and its anisotropy was first studied by Lussier *et al.* [96, 97]. Thermal conductivity has the disadvantage that it is difficult to separate phonon contributions which are dominant in conventional superconductors. However, for high-quality crystal UPt$_3$, phonon contribution κ_{ph} to the total thermal conductivity $\kappa = \kappa_{\mathrm{e}} + \kappa_{\mathrm{ph}}$ can be ignored in low temperatures. Indeed, κ_{ph} is estimated from the Wiedemann-Franz law [118] that states the electron contribution to the thermal conductivity κ_{e} and the electrical resistivity ρ have $L_0 = \kappa_{\mathrm{e}}\rho/T$, where constant L_0 is the Lorenz number. In fact, $L(T) = \kappa\rho/T = 0.99L_0$ at $T = 0.1$ K, this implies κ is mostly electronic below 0.1 K in 3T (above $H_{c2}(0)$) in the normal state [96].

Figure 4.2 (a) shows the temperature dependence of thermal conductivity along c-axis κ_c/T [113]. Data at very low temperatures below 30 mK implies that a finite value of κ_c/T is expected at $T = 0$ and this indicates a finite density of states of quasiparticles at zero energy. One expects this κ_c/T agrees with the *universal* transport but it is about 10 times smaller than the prediction [82]. Since the crystal structure is not cubic but hexagonal, the thermal conductivity has anisotropy. Figure 4.2 (b) shows anisotropy κ_c/κ_b. The usual E_{1g} state has point nodes in the north and south poles and a line node in the basal plane. If impurity effects are ignored, one expects that this ratio κ_c/κ_b vanishes at $T = 0$. This is because κ_c is dominated by point nodes with linear dispersion corresponding to density of states $\sim \omega^2$, while κ_b is dominated by line node with linear dispersion corresponding to density of states $\sim \omega$ (See also Table 2.1 in Chapter 2). However, as shown in Figure 4.2 (b), the ratio
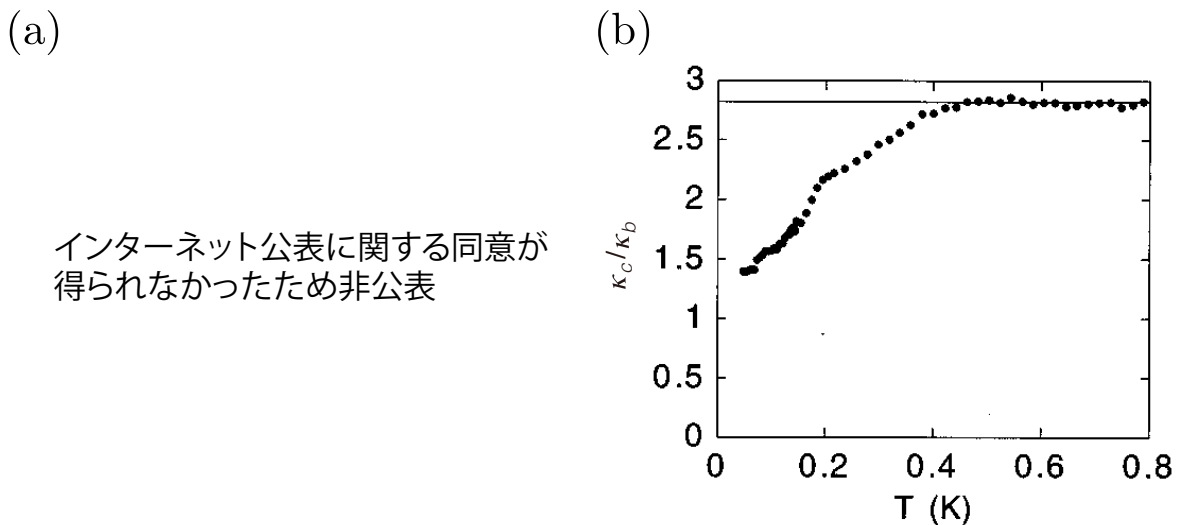
(a)

(b)

インターネット公表に関する同意が
得られなかったため非公表

Figure 4.2: (a) Temperature dependence of thermal conductivity along c-axis κ_c/T [113]. (b) Temperature dependence of the ratio of c-axis to in-plane thermal conductivity κ_c/κ_b [97].

approaches a finite value at lower temperatures.

Finally, we comment on the other experiments to determine the symmetry of the gap. The NMR relaxation rate $1/T_1$ varies in proportion to T^3 at low temperatures [98] (See Fig. 4.3(a)). This behavior indicates the presence of the line nodes and this is consistent with thermal conductivity above 100 mK. The experiments have not yet been performed at very low temperature below 30 mK where the gapless behavior is expected. Specific heat is another powerful tool to verify the nodal structure of the superconducting gap. There is no power or an unusual dependence in $C(T)/T$ at low temperatures below 0.1 K [85, 99]. (See Fig. 4.3(b)) Some groups pointed out that it is related to an antiferromagnetic long-range ordering [99, 122].

4.2 Effective model

In this section, we introduce a model that describes the electronic structure in the normal-state of UPt$_3$ and define some symmetry operators. Quantum oscillation measurements combined with band structure calculations [123–125] show that there is a pair of Fermi surfaces centered at the A-point, three at the Γ-point and two at the K-point in UPt$_3$. However, since small Fermi surfaces enclosing the K-point give a small density of states, their contribution may be a minor and we ignore them.

The space group of UPt$_3$ is $P6_3/mmc$, which is a nonsymmorphic structure (See Fig. 4.4) and the corresponding point group is D_{6h}. Since this space group is nonsymmorphic, some symmetry operations are the combination of point group operations and translations. Some of the point groups have to be combined with trivial translations to map the crystal onto itself, with generating point group isomorphic to D_{6h}.

We start from the model introduced in Ref. [41–43] for describing the normal-state elec-

(a)   (b)
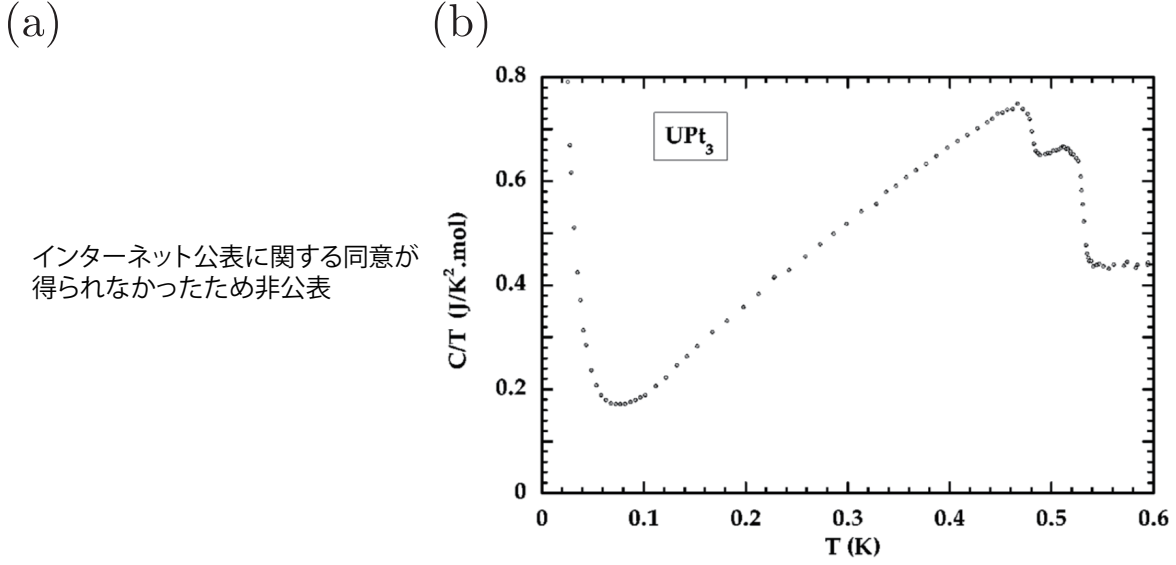
インターネット公表に関する同意が
得られなかったため非公表

Figure 4.3: (a) Temperature dependence of the NMR relaxation rate $1/T_1$ [98]. (b) Temperature dependence of the specific heat [82]. The original data is from Ref. [85].

tronic structure UPt$_3$,

$$H\left(\boldsymbol{k}\right) = \xi_{\boldsymbol{k}}\tau_0\sigma_0 + \frac{\epsilon_{\boldsymbol{k}}}{2}\tau_+\sigma_0 + \frac{\epsilon_{\boldsymbol{k}}^*}{2}\tau_-\sigma_0 + \boldsymbol{g}_{\boldsymbol{k}}\cdot\boldsymbol{\sigma}\tau_z \tag{4.2}$$

where Pauli matrices τ_i (σ_i) describe two sublattice (spin) degrees of freedom, $\tau_\pm = (\tau_x \pm i\tau_y)$, and the intrasublattice hopping and chemical potential,

$$\xi_{\boldsymbol{k}} = 2t\sum_{i=1}^3 \cos\left(\boldsymbol{k}_\parallel\cdot\boldsymbol{e}_i\right) + 2t_z\cos k_z - \mu, \tag{4.3}$$

and the intrasublattice hoping,

$$\epsilon_{\boldsymbol{k}} = 2t'\cos\frac{k_z}{2}\sum_{i=1}^3 e^{i\boldsymbol{k}_\parallel\cdot\boldsymbol{r}_i}, \tag{4.4}$$

and symmetry allows Kane-Mele type spin-orbit coupling,

$$\boldsymbol{g}_{\boldsymbol{k}} = \alpha\hat{z}\sum_{i=1}^3 \sin\left(\boldsymbol{k}_\parallel\cdot\boldsymbol{e}_i\right), \tag{4.5}$$

where $\boldsymbol{k}_\parallel = (k_x, k_y, 0)$, $\boldsymbol{e}_i = (\cos\phi_i, \sin\phi_i, 0)$ with $\phi_i = (i-1)\,2\pi/3$, $\boldsymbol{r}_i = \left(\cos\phi_i'/\sqrt{3}, \sin\phi_i'/\sqrt{3}, 1/2\right)$ with $\phi_i' = (i-1)\,2\pi/3 + \pi/6$ and $i = 1, 2, 3$. We divide UPt$_3$ into two sublattices, namely even and odd layers in order to treat that Uranium ions form an AB-stacking of triangular lattices. The crystal structure of UPt$_3$ is illustrated in Fig. 4.4. The irreducible representations of Pauli matrices τ_i are summarized in Table 4.3.
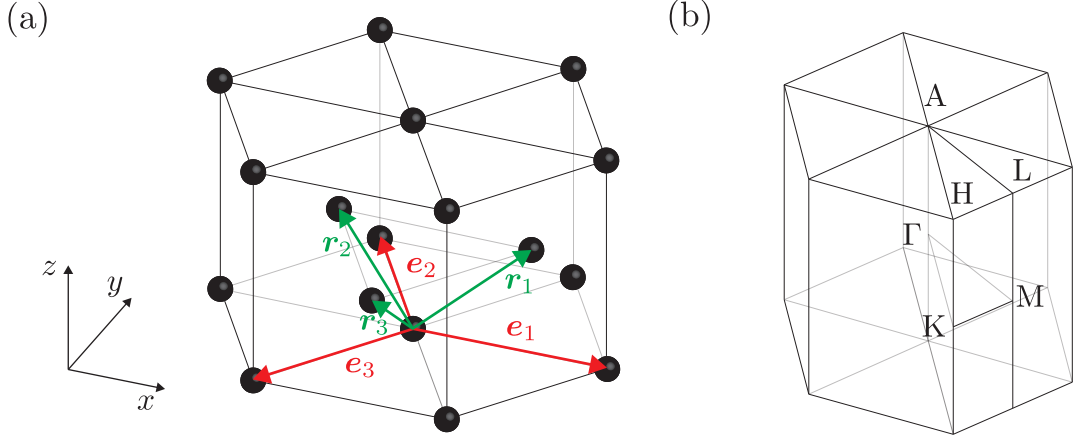
Figure 4.4: (a) Crystal structure of UPt$_3$. Uranium ions form a AB-stacking of triangular lattices. Vectors $\boldsymbol{e}_i$'s and $\boldsymbol{r}_i$'s, are shown by arrows. (b) the Brillouin zone.

Table 4.3: Irreducible representation of sublattice matrices.

	sublattice singlet	sublattice triplet
A_{1g}	$-$	τ_0, τ_x
B_{2u}	τ_y	τ_z

The Hamiltonian (4.2) is parameterized by the set of five parameters $(t, t_z, t', \alpha, \mu)$. Now we take in-plane hopping t as energy unit. As mentioned above, we consider Fermi surfaces around the Γ- and A-point. (See also Fig. 4.4(b)) When we chose $(t, t_z, t', \alpha, \mu) = (1, 4, 1, 0, 16)$, this model reproduces two degenerate spherical Fermi surfaces around Γ-point as shown in Figure 4.5(a). On the other hand, another set of parameters $(t, t_z, t', \alpha, \mu) = (1, 4, 1, 2, 12)$ reproduces two Fermi surfaces around the A-point (Figure 4.5(b)).

Let us now discuss the symmetries of the Hamiltonian (4.2). The time-reversal operator T is given by $T = K\tau_0 (i\sigma_y)$ and K is complex conjugate operator, which acts as

$$TH(\boldsymbol{k}) T^{-1} = H(-\boldsymbol{k}). \tag{4.6}$$

The spatial inversion operator P is defined by $P = \tau_x \sigma_0$ and this acts

$$PH(\boldsymbol{k}) P^{-1} = H(-\boldsymbol{k}). \tag{4.7}$$

There is another symmetry related to the particle-hole transformation. Let us define the particle-hole conjugate operator C is given by $C = K\Gamma_x \tau_0 \sigma_0$, which acts as

$$CH(\boldsymbol{k}) C^{-1} = -H(-\boldsymbol{k}), \tag{4.8}$$

where Pauli matrices Γ_i describe the particle-hole degree of freedom.
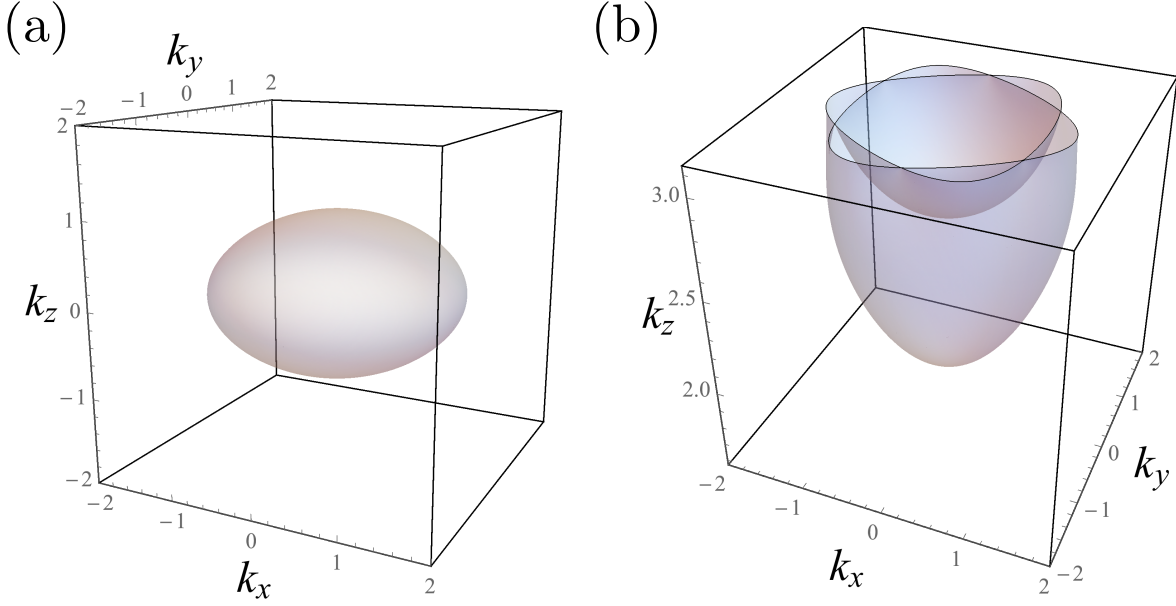
Figure 4.5: Fermi surfaces of normal states UPt$_3$ around (a) Γ-point for $(t, t_z, t', \alpha, \mu) = (1, 4, 1, 0, 16)$ and (b) A-point for $(t, t_z, t', \alpha, \mu) = (1, -4, 1, 2, 12)$.

4.3 E_{1g} pairing state

4.3.1 Symmetry consideration

So far, many researchers have considered the pairing with E_{2u} assuming that the gap function has odd-parity and it is spin-triplet. Recently, Yanase studied a new type of E_{2u} states in nonsymmorphic systems and they include spin-singlet d-wave, spin-triplet p- and f-wave pairings [41]. It is worthwhile to examine the other two-dimensional representations E_{1g}, E_{2g}, and E_{2u} as candidates for the gap symmetry. As mentioned in Section 2.3, if time-reversal symmetry is broken in an even-parity superconducting state, one expects the emergence of the Bogoliubov Fermi surfaces. For this possibility, E_{1u} and E_{2u} states are excluded since they have odd-parity. We also exclude an E_{2g} state because line nodes in the basal plane are not expected there. Therefore, we consider only E_{1g} pairing state and study this case in the following sections.

For two-orbital superconductors, the gap function is generally written as

$$\Delta(\boldsymbol{k}) = \sum_{i=0,x,y,z} [\psi_i(\boldsymbol{k}) + \boldsymbol{d}_i(\boldsymbol{k}) \cdot \boldsymbol{\sigma}] (i\sigma_y) \otimes \tau_i, \tag{4.9}$$

where σ_j and τ_i operate in spin and orbital spaces, respectively. As shown in Table 4.3, the operators τ_i's have the symmetry of A_{1g} or B_{2u}. The gap function with E_{1g} pairing state is constructed by (i) $E_{1g} = E_{1g} \otimes A_{1g}$ and (ii) $E_{1g} = E_{2u} \otimes B_{2u}$. We note that the Pauli principle restricts possible pairing condition. This condition is given by parity of $\boldsymbol{k}$, whether spin-singlet or -triplet and whether sublattice-singlet or triplet. Table 4.4 shows sign of parity of $\boldsymbol{k}$, spin, and sublattice to determine whether the Pauli principle works or does not. The Pauli principle requires, the products of $\boldsymbol{k}$, and spin, and sublattice should be minus.

Table 4.4: Sign of $\boldsymbol{k}$, spin and sublattice. The Pauli principle requires the products of $\boldsymbol{k}$, and spin, and sublattice should be minus.

sign	$\boldsymbol{k}$	spin	sublattice
-	odd	σ_0(singlet)	τ_y (singlet)
+	even	$\sigma_x, \sigma_y, \sigma_z$ (triplet)	τ_0, τ_x, τ_z (triplet)

E_{1g} spin-singlet pairing

We discuss spin-singlet pairing belonging to E_{1g} representation. (i) We consider the simple case of $E_{1g} = E_{1g} \otimes A_{1g}$. In this case, the pairing state is $\boldsymbol{k}$ even for spin-singlet and we use the sublattice part, τ_0 and τ_x have A_{1g} symmetry. We find the pairings are the followings:

$$\{d_{yz}\left(\boldsymbol{k}\right)\sigma_0\tau_x,\ d_{zx}\left(\boldsymbol{k}\right)\sigma_0\tau_x\} \tag{4.10}$$

$$\{d_{yz}\left(\boldsymbol{k}\right)\sigma_0\tau_0,\ d_{zx}\left(\boldsymbol{k}\right)\sigma_0\tau_0\} \tag{4.11}$$

(ii) The second choice is the case of $E_{1g} = E_{2u} \otimes B_{2u}$. The pairing state is $\boldsymbol{k}$ odd for spin-singlet and the Pauli principle requires to use sublattice matrix τ_y only as B_{2u}. However, τ_z does not have the proper sing for the Pauli principle. As a result, $E_{1g} = E_{2u} \otimes B_{2u}$ pairing is the following:

$$\left\{f_{z(x^2-y^2)}\left(\boldsymbol{k}\right)\sigma_0\tau_y,\ f_{xyz}\left(\boldsymbol{k}\right)\sigma_0\tau_y\right\}. \tag{4.12}$$

E_{1g} spin-triplet pairing

As same as spin-singlet case, we construct spin-triplet pairing belonging to E_{1g} representation. (i) We consider simply the case of $E_{1g} = E_{1g} \otimes A_{1g}$ corresponding to the pairing state of $\boldsymbol{k}$ even and spin-triplet. The Pauli principle requires τ_y for sublattice degree of freedom but this belongs to B_{2u}. Consequently, the choice of $E_{1g} = E_{1g} \otimes A_{1g}$ is not suitable. (ii) We consider the case of $E_{1g} = E_{2u} \otimes B_{1u}$. The pairing state is $\boldsymbol{k}$ odd and spin-triplet and the Pauli principle requires τ_z for sublattice degree of freedom and this belongs to B_{2u}. In this case, the pairing with $\boldsymbol{d} \parallel \hat{z}$ is

$$\left\{f_{z(x^2-y^2)}\left(\boldsymbol{k}\right)\sigma_z\tau_z,\ f_{xyz}\left(\boldsymbol{k}\right)\sigma_z\tau_z\right\}, \tag{4.13}$$

and for in-plane $\boldsymbol{d}$ vector $(\boldsymbol{d} \perp \hat{z})$ is

$$\{p_x\left(\boldsymbol{k}\right)\sigma_x\tau_z - p_y\left(\boldsymbol{k}\right)\sigma_y\tau_z,\ p_x\left(\boldsymbol{k}\right)\sigma_y\tau_z + p_y\left(\boldsymbol{k}\right)\sigma_x\tau_z\}. \tag{4.14}$$

4.3.2 E_{1g} model

In the previous section, we examined possible E_{1g} pairings based on symmetry. In general, the mixing of p-, d-, and f-wave components result from many-body effect and the weight of these components should be calculated from microscopic theories. In this section, we consider the normal-state Hamiltonian in Eq. (4.2) and construct gap function with E_{1g} symmetry by introducing the short-range Cooper pairs i.e., intra or intersublattice (next) nearest neighbor (NN) pairings. Taking the intrasublattice next nearest neighbor pairing into consideration is reasonable because is $c/a = 0.85$, where the lattice constants $a = 5.764$ Å and $c =$

4.899 Å [82]. Indeed, the spin-singlet d-wave pairing can be made from intersublattice pairing, spin-triplet p-wave ($\boldsymbol{d} \perp \hat{z}$) and f-wave pairing ($\boldsymbol{d} \parallel \hat{z}$) can be made from intrasublattice pairings. Therefore, the spin-singlet d-wave part $\{d_{zx}(\boldsymbol{k}), d_{yz}(\boldsymbol{k})\} \tau_x \sigma_0 i\sigma_y$ has $\boldsymbol{k}$-dependence and formed on the $\boldsymbol{r}_i$-bonds (See Fig. 4.4(a)) as

$$d_{zx}(\boldsymbol{k}) = \sin\frac{k_z}{2} \sum_{i=1,2,3} \boldsymbol{r}_i^x \sin\left(\boldsymbol{k}_\parallel \cdot \boldsymbol{r}_i\right) = \sin\frac{k_x}{2} \cos\frac{k_y}{2\sqrt{3}} \sin\frac{k_z}{2}, \tag{4.15}$$

$$d_{yz}(\boldsymbol{k}) = \sin\frac{k_z}{2} \sum_{i=1,2,3} \boldsymbol{r}_i^y \sin\left(\boldsymbol{k}_\parallel \cdot \boldsymbol{r}_i\right)$$

$$= \frac{1}{\sqrt{3}} \left(\cos\frac{k_x}{2} \sin\frac{k_y}{2\sqrt{3}} + \sin\frac{k_y}{\sqrt{3}}\right) \sin\frac{k_z}{2}. \tag{4.16}$$

For the spin-triplet p-wave pairing Eq. (4.13) $\boldsymbol{d} \parallel \hat{z}$, the factors are formed with $\boldsymbol{e}_i$-bonds as

$$f_{z(x^2-y^2)}(\boldsymbol{k}) = \sin k_z \sum_{i=1,2,3} \boldsymbol{e}_i^x \sin\left(\boldsymbol{k}_\parallel \cdot \boldsymbol{e}_i\right)$$

$$= \left(\cos k_x - \cos\frac{k_x}{2} \cos\frac{\sqrt{3}k_y}{2}\right) \sin k_z, \tag{4.17}$$

$$f_{xyz}(\boldsymbol{k}) = \sin k_z \sum_{i=1,2,3} \boldsymbol{e}_i^y \sin\left(\boldsymbol{k}_\parallel \cdot \boldsymbol{e}_i\right) = \sqrt{3} \sin\frac{k_x}{2} \sin\frac{\sqrt{3}k_y}{2} \sin k_z. \tag{4.18}$$

while for the case $\boldsymbol{d} \perp \hat{z}$ (4.14),

$$p_x(\boldsymbol{k}) = \sum_{i=1,2,3} \boldsymbol{e}_i^x \sin\left(\boldsymbol{k}_\parallel \cdot \boldsymbol{e}_i\right) = \sin k_x + \sin\frac{k_x}{2} \cos\frac{\sqrt{3}k_y}{2}, \tag{4.19}$$

$$p_y(\boldsymbol{k}) = \sum_{i=1,2,3} \boldsymbol{e}_i^y \sin\left(\boldsymbol{k}_\parallel \cdot \boldsymbol{e}_i\right) = \sqrt{3} \cos\frac{k_x}{2} \sin\frac{\sqrt{3}k_y}{2}. \tag{4.20}$$

With three coefficients, order parameter of the E_{1g} state is represented as $\left(\hat{\Gamma}_1(\boldsymbol{k}), \hat{\Gamma}_2(\boldsymbol{k})\right)$ with

$$\hat{\Gamma}_1(\boldsymbol{k}) = \left[\Delta_d d_{yz}(\boldsymbol{k}) \tau_x\sigma_0 + \Delta_f f_{z(x^2-y^2)}(\boldsymbol{k}) \tau_z\sigma_z \right.$$
$$\left. + \Delta_p\left(p_x(\boldsymbol{k})\sigma_x - p_y(\boldsymbol{k})\sigma_y\right)\tau_z\right] i\sigma_y, \tag{4.21}$$

$$\hat{\Gamma}_2(\boldsymbol{k}) = \left[\Delta_d d_{zx}(\boldsymbol{k}) \tau_x\sigma_0 + \Delta_f f_{xyz}(\boldsymbol{k}) \tau_z\sigma_z \right.$$
$$\left. + \Delta_p\left(p_x(\boldsymbol{k})\sigma_y + p_x(\boldsymbol{k})\sigma_y\right)\tau_z\right] i\sigma_y. \tag{4.22}$$

We note that this E_{1g} state is similar to the E_{2u} state studied in Refs. [41–43], differing in the sublattice degrees of freedom. This state has point nodes at the north and south poles and line node along the equator if $\Delta_p = 0$. In this thesis, we consider the case of $|\Delta_p| \ll \Delta_d, \Delta_f$, which is compatible with the experiments [105] and assume Δ_p, Δ_d and Δ_f are real. Therefore, the BdG Hamiltonian is

$$H_{\mathrm{BdG}}(\boldsymbol{k}) = \begin{bmatrix} H(\boldsymbol{k}) & \Delta(\boldsymbol{k}) \\ \Delta^\dagger(\boldsymbol{k}) & -H^T(-\boldsymbol{k}) \end{bmatrix}, \tag{4.23}$$

where

$$\Delta(\boldsymbol{k}) = \eta_1 \hat{\Gamma}_1(\boldsymbol{k}) + \eta_2 \hat{\Gamma}_2(\boldsymbol{k}). \tag{4.24}$$

4.4 Bogoliubov Fermi surfaces in E_{1g} state

4.4.1 Bogoliubov Fermi surfaces

In this section, we define the $\mathbb{Z}_2$ invariant for the model (4.2) following Ref. [37] and Section 2.3. We also find the finite p-wave pairing amplitude in E_{1g} state reproduces the Bogoliubov Fermi surfaces.

We define the $\mathbb{Z}_2$ invariant defined by the sign of a Pfaffian. The Hamiltonian has the symmetry related to the combination of the particle-hole conjugate operator C and the spatial inversion operator P, we obtain

$$(CP) H_{\text{BdG}}(\boldsymbol{k}) (CP)^{-1} = -H_{\text{BdG}}(\boldsymbol{k}). \tag{4.25}$$

Because $(CP)^2 = +1$, one can find unitary operator Ω that transforms $H_{\text{BdG}}(\boldsymbol{k})$ as antisymmetric matrix. We define $U_{CP} \equiv U_C P = \Gamma_x \tau_x \sigma_0$ where $U_C = \Gamma_x \tau_x \sigma_0$ and $P = \Gamma_0 \tau_x \sigma_0$. Notice C is antiunitary but U_C is unitary. Then,

$$U_{CP} H_{\text{BdG}}(\boldsymbol{k})^T U_{CP}^\dagger = -H_{\text{BdG}}(\boldsymbol{k}). \tag{4.26}$$

Because U_{CP} is a symmetric matrix, it can be diagonalized as

$$U_{CP} = Q \Lambda Q^T, \tag{4.27}$$

where Q is a unitary matrix and Λ is a diagonal matrix and we note the transposed matrix Q^T (not $Q^\dagger$). Inserting this into Eq. (4.26),

$$Q \Lambda Q^T H_{\text{BdG}}(\boldsymbol{k})^T Q^* \Lambda^\dagger Q^\dagger = -H_{\text{BdG}}(\boldsymbol{k}). \tag{4.28}$$

Since Λ is a diagonal matrix, its square root can be defined, $\sqrt{\Lambda} = \text{diag}\left(\sqrt{\lambda_1}, \sqrt{\lambda_2}, \cdots\right)$ even though $\sqrt{\lambda_i}$'s are complex. Defining with a unitary transformation $\sqrt{\Lambda}^\dagger Q^\dagger H_{\text{BdG}}(\boldsymbol{k}) Q \sqrt{\Lambda} \equiv \tilde{H}_{\text{BdG}}(\boldsymbol{k})$, it is easy to show the following relation,

$$\tilde{H}_{\text{BdG}}(\boldsymbol{k})^T = -\tilde{H}_{\text{BdG}}(\boldsymbol{k}). \tag{4.29}$$

Therefore, $\tilde{H}_{\text{BdG}}(\boldsymbol{k})$ is an anti-symmetric matrix. We can define a $\mathbb{Z}_2$ invariant at each $\boldsymbol{k}$ with the sign of Pfaffian

$$P(\boldsymbol{k}) = \text{sgn}\left[\text{Pf } \tilde{H}_{\text{BdG}}(\boldsymbol{k})\right], \tag{4.30}$$

and $\mathbb{Z}_2$ quantity for each Bogoliubov Fermi surface by

$$(-1)^l = P(\boldsymbol{k}_-) P(\boldsymbol{k}_+). \tag{4.31}$$

Here, $\boldsymbol{k}_+ (\boldsymbol{k}_-)$ is a momentum inside (outside) of Bogoliubov Fermi surfaces.

Now we discuss the Bogoliubov Fermi surfaces around the Γ- and the A-point of BZ. We consider the case of pairing $\Delta(\boldsymbol{k}) = \hat{\Gamma}_1 + i\eta\hat{\Gamma}_2$ with real η and basis functions (4.21) and (4.22) , which breaks the time-reversal symmetry. Since the results do not change qualitatively with the value of η, we chose $\eta = 1$ for simplicity. Note that we use different sets of the parameter (t, t_z, t, α, μ) to reproduce normal-state Fermi surfaces near the Γ- and the A-point of BZ. Furthermore, we consider the electronic states near the Γ- and the A-point

of BZ independently and ignore intercoupling effects and the difference of the weight of p-, d-, and f-wave pairing amplitudes between the Γ- and the A-point of BZ.

For around the Γ-point of BZ, in the case of $\Delta_p = 0$, $\Delta(\boldsymbol{k})$ has a horizontal line node in the $k_z = 0$ and two-point nodes at the north and south poles ($k_x = k_y = 0$). When $\Delta_p \neq 0$, we find one Bogoliubov Fermi surface with nontrivial $\mathbb{Z}_2$ invariant. The line node disappears but two point nodes at the north and south poles persist. Figure 4.6(a) illustrates the normal-state Fermi surfaces (transparent) and the region of $P(\boldsymbol{k}) < 0$ (orange), and the surface, of which is the Bogoliubov Fermi surface with nontrivial $\mathbb{Z}_2$ invariant. The parameters are $\Delta_p = \Delta_d = \Delta_f = 0.4$. This Bogoliubov Fermi surface forms a thin torus located around the original line nodes and can been understood as the inflation of the original horizontal line nodes. When Δ_p increases, the Bogoliubov Fermi surface grows as shown in Figure 4.6(b).

For around the A-point of BZ, the pairing with $\Delta_p = 0$ has line nodes that form six rings in the $k_z = \pi$ plane and two-point nodes at $k_x = k_y = 0$ on the normal-state Fermi surfaces. Figure 4.6(c) illustrates the normal-state Fermi surfaces (transparent) and the regions of $P(\boldsymbol{k}) < 0$ (orange) and the surfaces, of which are the Bogoliubov Fermi surfaces with nontrivial $\mathbb{Z}_2$ invariant. The parameters are $\Delta_p = \Delta_d = \Delta_f = 0.1$. These Bogoliubov Fermi surfaces are located around the original six rings of line nodes and form hollow sphere-wises. One may understand that as the original line nodes are inflated. When Δ_p increases, the regions of $P(\boldsymbol{k}) < 0$ expanded as shown in Figure 4.6(d). Two point nodes at the north and south poles persist even when $\Delta_p \neq 0$. We note that there are no Bogoliubov Fermi surfaces in superconducting states with time-reversal symmetry.

The gap nodes around the Γ- and the A-point has the common properties that the horizontal line nodes inflate when $\Delta_p \neq 0$ but the point nodes do not. These properties can be understood by considering the pseudo-chemical potential $\delta\mu(\boldsymbol{k})$ and pseudo-magnetic field $\delta h(\boldsymbol{k})$ introduced in Sec. 2.3.3. Note that $\delta\mu(\boldsymbol{k})$ and $\delta h(\boldsymbol{k})$ result from a pairing with broken time-reversal symmetry. Figure 4.7(a) and (b) schematically show the cases that the Bogoliubov Fermi surfaces emerge and do not emerge, respectively. A nodal superconductor has point or line node at $\boldsymbol{k} = \boldsymbol{k}^*$ (See left sides in Figure 4.7(a) and (b)), which corresponds to the case of $\Delta_p = 0$ in our E_{1g} state. Both d- and f-wave pairing amplitudes have line nodes in the plane of $k_z = 0$ and π in addition to point nodes at $k_x = k_y = 0$ even if the pairing breaks time-reversal symmetry. When $\Delta_p \neq 0$, both $\delta\mu(\boldsymbol{k})$ and $\delta h(\boldsymbol{k})$ are generally finite at $\boldsymbol{k} = \boldsymbol{k}^*$ but both are zero at $k_x = k_y = 0$. Therefore, the line nodes are inflated and split into $\boldsymbol{k}_\mathrm{o}^*$ and $\boldsymbol{k}_\mathrm{i}^*$ but the point nodes are not inflated and remain as the point nodes.

4.4.2   Density of states

When Bogoliubov Fermi surfaces do not exist, the superconducting gap has no nodes, or point or line nodes. Thus, their density of states is zero at $\omega = 0$. However, once the Bogoliubov Fermi surfaces emerge, the density of states at $\omega = 0$ is finite and it may provide a natural explanation for finite κ/T value toward $T = 0$.

Here, we confirm that in-plane p-wave pairing amplitude in the broken time-reversal E_{1g} state, which gives the Bogoliubov Fermi surfaces near the Γ- and the A-point of BZ, also give a finite density of states at $\omega = 0$. The density of states $\rho(\omega)$ is given by

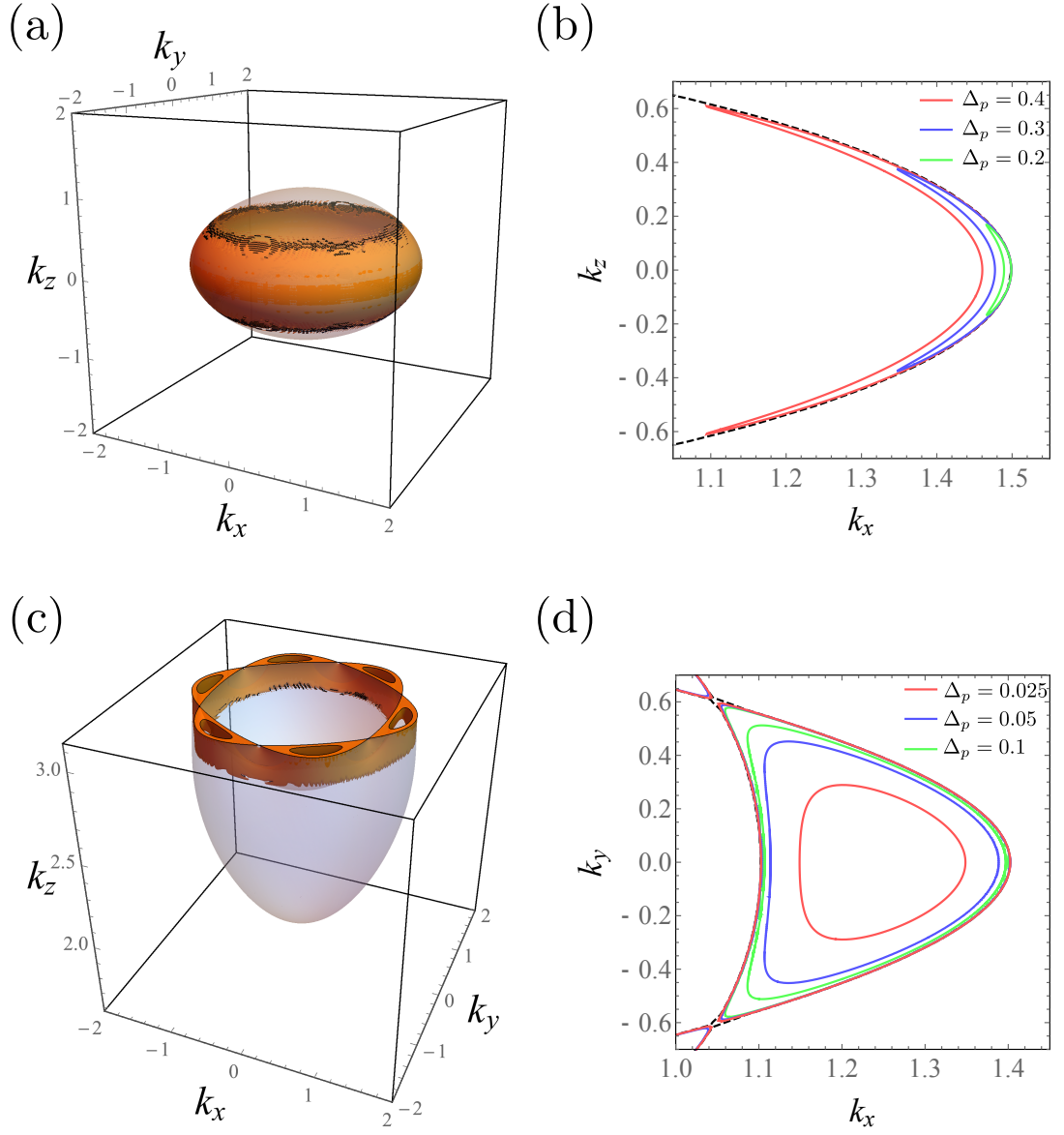$$\rho(\omega) = \frac{1}{V}\sum_{\boldsymbol{k}} \delta(\omega - E_{\boldsymbol{k}}). \tag{4.32}$$

Figure 4.6: The normal-state and Bogoliubov Fermi surfaces around Γ- and A-point of BZ. (a) and (c) the normal-state Fermi surfaces (transparent) and the regions of $P(\boldsymbol{k}) < 0$ (orange), and the surfaces, of which are the Bogoliubov Fermi surfaces. (a) around the Γ-point and $\Delta_p = 0.4$ and (c) A-point and $\Delta_p = 0.1$. We use sets of the parameter $(t, t_z, t', \alpha, \mu) = (1, 4, 1, 0, 16)$ and $(1, -4, 1, 2, 12)$ to reproduces normal-state Fermi surfaces around Γ- and A-point, respectively. (b) and (d) show the cut of the plane $k_y = 0$ and $k_z = \pi$, respectively. The normal-state Fermi surfaces are shown by dashed line and the Bogoliubov Fermi surfaces are shown by solid lines. The parameters are $\Delta_d = \Delta_f = 0.4$ in (a) and (b), and $\Delta_d = \Delta_f = 0.1$ in (c) and (d).
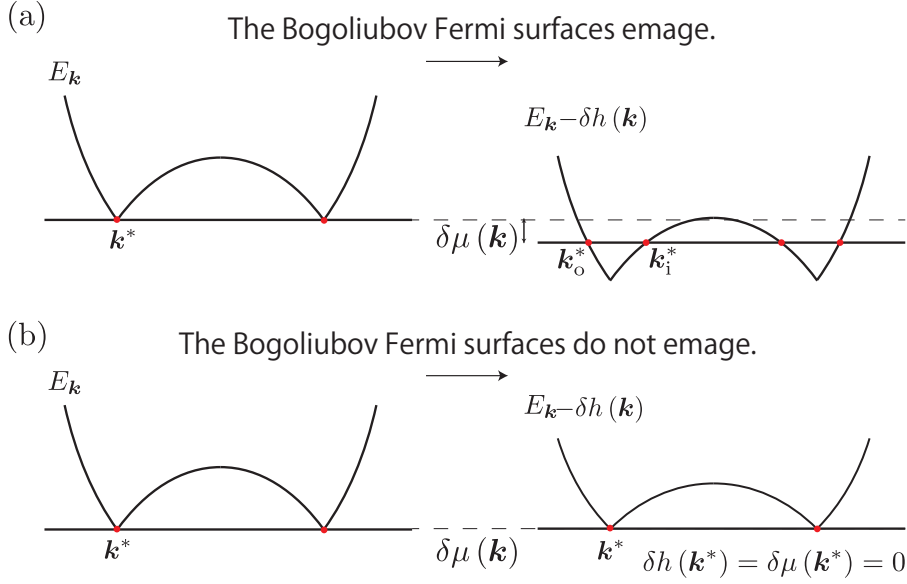
Figure 4.7: Schematic pictures that the Bogoliubov Fermi surfaces emerge (a) and do not emerge (b). In case they do not emerge, the pseudo-chemical potential $\delta\mu\,(\boldsymbol{k})$ and the pseudo-magnetic field $\delta\boldsymbol{h}\,(\boldsymbol{k})$ both vanish at original node position $\boldsymbol{k} = \boldsymbol{k}^*$.

Note that we use different sets of the parameter $(t, t_z, t', \alpha, \mu)$ to reproduce normal-state Fermi surfaces near the Γ- and the A-points of BZ. Furthermore, we consider the electronic states near the Γ- and the A-points of BZ independently and ignore intercoupling effects and the difference of the weight of p-, d-, and f-wave pairing amplitudes between the Γ- and the A-points of BZ. Therefore, we may discuss qualitatively but cannot do quantitatively. Figure 4.8 shows the contribution to the density of states from (a) the Γ- and (b) the A-point of BZ in broken time-reversal E_{1g} pairing state. When $\Delta_p = 0$, the density of states at $\omega = 0$ is zero both contributions near the Γ- and the A-points of BZ. Certainly, in-plane p-wave pairing is necessary for Bogoliubov Fermi surfaces.

4.5 Thermal conductivity for E_{1g} state

As mentioned in Section 4.1.2, the thermal conductivity at a very low temperature below 30 mK implies a finite value of κ_c/T at $T = 0$ and this originates from a finite density of states of quasiparticles at $\omega = 0$. The finite value of κ_c/T at $T = 0$ also indicate a finite ration of anisotropy κ_c/κ_b in the limit of $T = 0$. For usual E_{1g} state [92, 94, 103, 104], one expects this ratio to become zero since the κ_c is dominated by the point nodes that have linear dispersion with a density of states $\sim \omega^2$ and the κ_b is dominated by line node which has linear dispersion with a density of states $\sim \omega$.

We propose in the thesis that our proposed E_{1g} state may provide a natural explanation for finite κ/T and κ_c/κ_b at $T = 0$. This is because the line nodes of the E_{1g} state are inflated and to form Bogoliubov Fermi surfaces and they explain the behaviors of κ. We would like
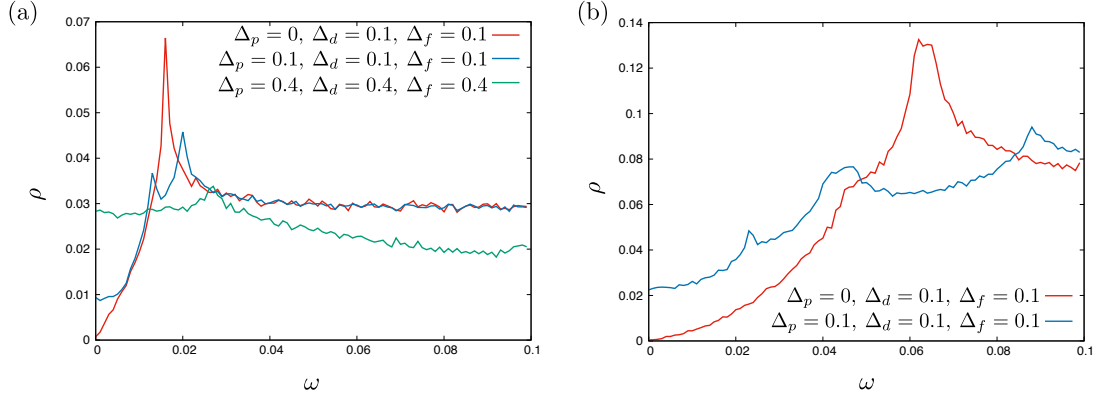
Figure 4.8: The contribution to the density of states from (a) the Γ- and (b) the A-point of BZ in broken time-reversal E_{1g} pairing state. We use sets of parameter $(t, t_z, t', \alpha, \mu) = (1, 4, 1, 0, 16)$ and $(1, -4, 1, 2, 12)$ to reproduces normal-state Fermi surfaces around the Γ- and the A-point, respectively.

to emphasize that the Bogoliubov Fermi surfaces appear as an intrinsic effect. That is, the in-plane p-wave pairing has a finite amplitude in bulk and this pairing controls the size of the Bogoliubov Fermi surfaces. In order to explain a value of κ_c/T smaller than the predicted universal transport, one may take the amplitude of in-plane p-wave pairing is smaller than the other amplitudes, and then this makes small Bogoliubov Fermi surfaces. Indeed, Knight shift in the NMR experiment revealed that the in-plane spin-triplet parts are smaller than the c-axis spin-triplet part [105], and this is consistent with the expectation above.

In this section, we study the thermal conductivity for our proposed E_{1g} state and calculate values of κ_c/T and κ_c/κ_b at $T = 0$ by using the Boltzmann equation with the approximation of relaxation time [117]. The thermal conductivity tensor in the single band model was derived in Ref. [126] and was generalized for the multi-orbital model [127] is written in

$$\kappa_{ij} = -\sum_{\boldsymbol{k},l} \frac{E_{\boldsymbol{k}l}^2}{T} \left(\boldsymbol{v}_{\boldsymbol{k}l}\right)_i \left(\boldsymbol{v}_{\boldsymbol{k}l}\right)_j \frac{\partial n_{\boldsymbol{k}l}^0}{\partial E_{\boldsymbol{k}l}} \tau_{\boldsymbol{k}l}, \tag{4.33}$$

where $\boldsymbol{k}$ is the momentum and l labels the extra degrees of freedom such as orbital, sublattice or layer. $E_{\boldsymbol{k}l}$ is the quasiparticle energy, $n_{\boldsymbol{k}l}^0 = [1 + \exp(E_{\boldsymbol{k}l}/k_B T)]^{-1}$ is thermal equilibrium distribution function, $(\boldsymbol{v}_{\boldsymbol{k}l})_i = \partial_{k_i} E_{\boldsymbol{k}l}$ is quasiparticle velocity and $\tau_{\boldsymbol{k}l}^{-1}$ is the relaxation rate. In order to take into account for the Bogoliubov Fermi surfaces, we treat $\tau_{\boldsymbol{k}l}^{-1}$ as the normal-state relaxation rate $\tau_N = $ constant. Note that in general, $\tau_{\boldsymbol{k}l}$ in anisotropic superconductors have a complex form due to the coherence factors [128] and the normal-state phase shift [126,129]. We calculate numerically temperature dependence of $\kappa_b \equiv \kappa_{yy}$ and $\kappa_c \equiv \kappa_{zz}$. In this calculation, we assume temperature dependence of gap function [126,130] is

$$\Delta_i(T) = \Delta_i^0 \tanh\left[2\left(\frac{T_c - T}{T}\right)^{1/2}\right]. \tag{4.34}$$

This assumption ignores the multiple critical temperatures $T_c^{\pm}$. However, it is valid for $T \to 0$ far from T_c.
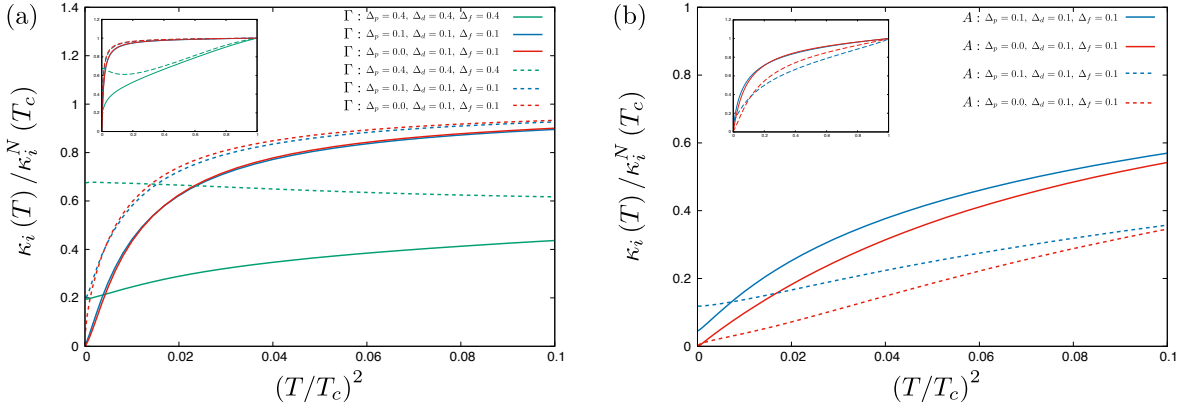
Figure 4.9: Temperature dependence of the contribution to κ_c/T (solid lines) and κ_b/T (dashed lines) from the Bogoliubov Fermi surfaces around (a) the Γ-point and (b) the A-point of BZ. Inset figures shows the full range: $0 < T < T_c = 0.05$. The vertical and horizontal axes are normalized by the normal-state thermal conductivity $\kappa_i^N(T_c)$ and T_c, respectively. The solid We use sets of parameter $(t, t_z, t', \alpha, \mu) = (1, 4, 1, 0, 16)$ and $(1, -4, 1, 2, 12)$ around the Γ- and the A-point, respectively.

Figure 4.9(a) and (b) show temperature dependence of the contribution to κ_b/T and κ_c/T from the Bogoliubov Fermi surfaces near the Γ- and the A-point of BZ, respectively. In the case of $\Delta_p \neq 0$, there is finite κ/T. This is consistent with that the in-plane p-wave pairing gives the Bogoliubov Fermi surfaces near both the Γ- and the A-point of BZ and finite density of states as we mentioned in Section 4.4.2.

Figure 4.10 shows the temperature dependence of the contribution to κ_c/κ_b from the Bogoliubov Fermi surfaces around the Γ- and the A-point of BZ. Once the in-plane p-wave pairing amplitude is finite and the Bogoliubov Fermi surfaces emerge, a value of κ_c/κ_b is finite even at $T = 0$. Therefore, the Bogoliubov Fermi surfaces due to small in-plane p-wave pairing amplitude give a good explanation of thermal conductivity.

Finally, we note that one should take into account $\boldsymbol{k}$ and T dependence of the relaxation time [128, 129] and the size of the normal-state Fermi surfaces for quantitative analysis. Our calculation is based on the assumption that the relaxation time of quasiparticle is considered as the normal-state relaxation time and ignores the size of the normal-state Fermi surfaces (but their topology is considered), it lacks a quantitative analysis and can not be compared simply with the hitherto scenario of impurity effect. We leave the quantitative analysis to future work.

4.6 Conclusion

In this chapter, we have addressed the issue of how we realize the new type of gap nodes, Bogoliubov Fermi surface, in multi-orbital superconductors and applied that idea to the multi-component superconductor UPt$_3$.

Unless impurity effects are taken into account, previous proposed gap symmetries do not explain the temperature dependence of thermal conductivity, which shows that a finite
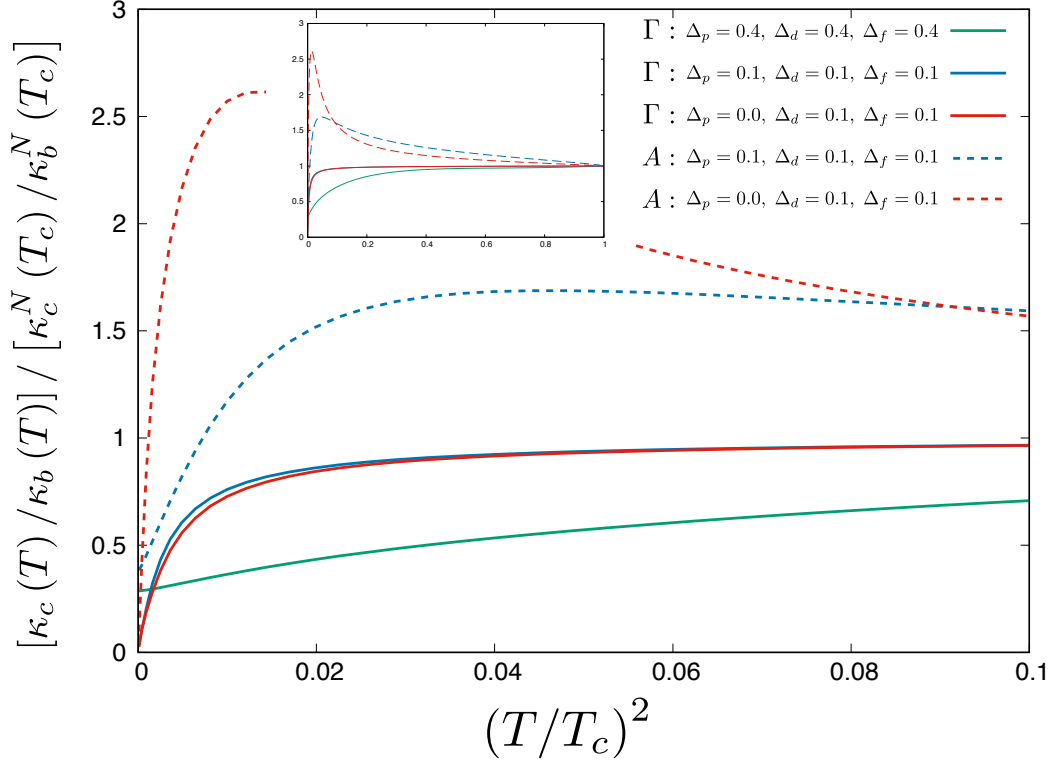
Figure 4.10: Temperature dependence of the contribution to κ_c/κ_b from the Bogoliubov Fermi surfaces around the Γ-point (solid lines) and the A-point (dashed lines) of BZ. We use sets of parameter $(t, t_z, t', \alpha, \mu) = (1, 4, 1, 0, 16)$ and $(1, -4, 1, 2, 12)$ around the Γ- and the A-point, respectively. Inset figures shows the full range: $0 < T < T_c = 0.05$. The vertical and horizontal axes are normalized by $\kappa_c^N(T_c)/\kappa_b^N(T_c)$ and T_c, respectively.

value of κ/T and also a finite ratio of the in-plane to c-axis thermal conductivity at very low temperatures. In order to explain them, we have applied the idea of Bogoliubov Fermi surface proposed by Agterberg *et al.*.

We have considered the pairing belonging to the two-dimensional E_{1g} representation in the point group D_{6h}. Nonsymmorphic crystal structure of UPt$_3$ allows to include spin-singlet d-wave, spin-triplet p- and f-wave pairings, and we have considered their mixer state. We have employed the model [41–43] which has the Fermi surfaces near the Γ- and the A-point in Brillouin zone in the normal-state. We have introduced $\mathbb{Z}_2$ invariant [37] by using the particle-hole conjugate (C) and inversion (P) symmetries and shown that the in-plane p-wave pairing amplitude needs to be finite to realize the Bogoliubov Fermi surfaces. Since the in-plane p-wave pairing has a finite amplitude in the planes $k_z = 0$ and π, the horizontal line nodes in these planes are inflated to the Bogoliubov Fermi surface. These Bogoliubov Fermi surfaces have nontrivial $\mathbb{Z}_2$ invariant defined by CP symmetry, and therefore we expect these are robust against the perturbations which preserve CP symmetry. The point nodes at $k_x = k_y = 0$ are not inflated and remain as point nodes. It is worthwhile to emphasize

Table 4.5: Correspondence to other experiments

	Our proposed E_{1g}
Multi-component $\boldsymbol{d}$ vector [105]	Yes
Anisotropy of H_{c2} [110, 111]	Yes
Breaking of time-reversal symmetry [40, 94, 95]	Yes
Field-orientation dependent thermal conductivity [112, 113]	Yes
NMR relaxation rate $1/T_1$ [98]	No
Field-angle dependence of the specific heat [115]	No

that the Bogoliubov Fermi surfaces appear as an intrinsic effect because the in-plane p-wave pairing has a finite amplitude in bulk and this pairing controls the size of the Bogoliubov Fermi surfaces.

We have calculated the thermal conductivity by using the Boltzmann theory and shown that the Bogoliubov Fermi surfaces give an explanation of a residual κ/T and anisotropy κ_c/κ_b. However, we note that since our calculation presumes that the relaxation time of quasiparticle is considered as constant and ignores the size dependence of the normal-state Fermi surfaces, it lacks a quantitative analysis and can not be compared directly to experiment data. Thus, we cannot exclude the possibility that the behaviors of thermal conductivity are explained by extrinsic effect such as impurities. In order to discuss quantitatively, one should take into account $\boldsymbol{k}$ and T dependence of the relaxation time and the size of the normal-state Fermi surfaces. We leave quantitative analysis to future work. We note that in general, the mixing of p-, d-, and f-wave pairings result from many-body effect and the weight of these pairing amplitudes should be calculated from microscopic theories.

Finally, we discuss implication to other experiments (See also Table 4.5). Our proposed E_{1g} pairing is compatible with the result of NMR Knight shift [105], which implies multi-component $\boldsymbol{d}$ vector, and twofold oscillation of the thermal conductivity within the basal plane in the C phase [112, 113] doe to d_{yz}-wave pairing. The spin-orbit coupling along the c-axis implies that the c-axis critical field is suppressed than the in-plane critical field and gives rise to the anisotropy of H_{c2} [110, 111]. An argument for this is given in Ref. [131]. The broken time-reversal E_{1g} state can be more stable than the time-reversal symmetric E_{1g} state. This is compatible with muon spin rotation-relaxation [94, 95] and polar Kerr effect experiments [40] imply the broken time-reversal symmetry in the B phase. However, there are two remaining problems. One expects that the NMR relaxation rate $1/T_1$ varies in proportion to T in the presence of Bogoliubov Fermi surface. This is inconsistent with the result by Kohori $et\ al.$ [98], which showed $1/T_1$ varies in proportion to T^3 in 100 mK $\leq T \leq 400$ mK. It is worth mentioning that at sufficiently high temperatures, the excitation spectrum will not show a difference between inflated nodes and nodes. However, this is not a satisfying answer. Another remaining problem is anomalous field-angle dependence of the

specific heat [115], which did not observe any in-plane angular oscillation.

Chapter 5

Summary and Conclusions

In this thesis, we have investigated the gap nodes in multi-orbital superconductors from a topological perspective. In particular, we have focused on (i) how nodeless, fully gapped superconducting states appears when the lattice symmetry dictates nodes in a nodeless state in multi-orbital systems and (ii) how to realize the new type of gap nodes, Bogoliubov Fermi surfaces. In both problems, orbital degrees of freedom play an important role.

In Chapter 3, the question (i) has been addressed and we have studied gap nodes in monolayer FeSe superconductor grown on $SrTiO_3$ substrate. We discussed topological charges of the nodes and explained the origin of a fully gapped d-wave state. We have investigated the effective two-orbital model which includes two types of superconducting pairing: orbitally trivial d-wave pairing and orbitally nontrivial isotropic one.

When the interband spin-orbit coupling is too strong, nodal points appear with $2\mathbb{Z}$ topological charges. We have found the momentum space distribution of the topological charges depends strongly on the orbital character of the pairing. When the orbitally trivial pairing is dominant, points on the same axis in the momentum space have the topological charges with a same sign (same sign pair state). On the other hand, when the orbitally nontrivial pairing is dominant, the adjacent nodal points on each axis have the topological charges with opposite signs (opposite sign pair state). As the spin-orbit coupling decreases, in the case of opposite sign pair state, the nodal points can merge and are annihilated directly in pairs of neighboring nodes because they have opposite charges. However, nodal points in the same sign pair states cannot annihilate directly. We have found that this annihilation occurs through an involved mechanism. As the interband spin-orbit coupling decreases, new nodal points are first created near the old one. As the spin-orbit coupling further decreases, some nodal points stay while other nodal points move off the k_x or k_y axis. With further decreasing the spin-orbit coupling, they continue to move and annihilate in pairs with other nodes moving from another direction. The nodal points with the nontrivial topological charges imply the existence of Andreev band states with flat dispersion in the direction parallel to an edge. We have shown different Andreev flat band spectra for the case of same sign and opposite sign pair state.

We also considered Zeeman coupling to examine the effects of broken time-reversal symmetry. In this case, we have found that the line and point nodes appear even when the spin-orbit coupling is weak. We have found that these nodal nodes are topologically protected by $\mathbb{Z}_2$ invariant.

In Chapter 4, we have addressed the question (ii) and have studied the multi-component

superconductor UPt$_3$. One plausible candidate of its gap symmetry in UPt$_3$ is E_{2u} representation in the point group D_{6h}. However, unless impurity effects are taken into account, this gap symmetry do not explain the behaviors of its thermal conductivity in the B phase, which shows that a finite value of κ/T and also a finite ratio of the in-plane to c-axis thermal conductivity at very low temperatures. In order to explain them, we have applied the idea of Bogoliubov Fermi surface proposed by Agterberg *et al.*.

We have employed on two-dimensional representation E_{1g} pairing. This representation includes spin-singlet d-wave, spin-triplet in-plane p- and out-of-plane f-wave mixing pairing. We have discussed the Fermi surfaces near the Γ- and the A-point in Brillouin zone in the normal state. We have introduced a $\mathbb{Z}_2$ invariant by using the particle-hole and the inversion symmetries and shown that the in-plane p-wave pairing amplitude needs to be finite to realize the Bogoliubov Fermi surfaces with nontrivial $\mathbb{Z}_2$ invariant. Since this pairing has a finite amplitude in the planes $k_z = 0$ and π, the horizontal line nodes of d-wave pairing in these planes are inflated. The point nodes at $k_x = k_y = 0$ are not inflated and remain as point nodes. It is worthwhile to emphasize that the Bogoliubov Fermi surfaces appear as an intrinsic effect. That is, amplitude of p-wave pairing in bulk controls the size of the Bogoliubov Fermi surfaces.

We have calculated the thermal conductivity by using the Boltzmann theory and shown that this theory explains a residual κ/T and anisotropy κ_c/κ_b. However, we note that since our calculation is based on the relaxation time approximation without necessary details, it lacks a quantitative analysis be compared with the alternative considering impurity effect. For more quantitative analysis, one should take into account $\boldsymbol{k}$ and T dependence of the relaxation time and the details of the normal-state Fermi surfaces. Thus, we leave the quantitative analysis to future work.

Thus, related issues are now raised.

For the issue (i), we have found two types of topological charges, $\mathbb{Z}$ and $\mathbb{Z}_2$ invariants. The $\mathbb{Z}$ invariant has its momentum space distribution depends strongly on the orbital character of the pairing and this reflects in some physical properties. However, its physical meaning of the $\mathbb{Z}_2$ invariant has not yet been investigated. However, we have found that this still remains invariant even if the time-reversal symmetry is broken.

For the issue (ii), first, we have constructed E_{1g} pairing by symmetry analysis and realized Bogoliubov Fermi surface in the B phase of UPt$_3$. It seems odd that Fermi surfaces exist in the superconductors. Therefore, more microscopic analysis, e.g., mean-field approach is needed. The second issue is what is the characteristic physical properties shown by the Bogoliubov Fermi surface. Although we have used a finite density of states at zero energy to explain thermal conductivity of UPt$_3$, it may originate also from impurity effect, and we cannot exclude its possibility. We hope that unique properties exclusive to the Bogoliubov Fermi surface will be discovered in the future.

Acknowledgements

I would like to acknowledge my supervisor Prof. Hirokazu Tsunetsugu for his various guidances and stimulating discussions during the five years of my graduate course.

Appendix A

Effective two-orbital model of monolayer FeSe

In this appendix, we briefly review the effective two-orbital model of monolayer FeSe following Ref. [32]. Monolayer FeSe has a nonsymmorphic structure presented by the space group P_4/nmm [70]. (See Fig. A.1(a)) It has an n-glide plane related to the combination of the mirror reflection about the FeSe plane and translation by a half unit cell. It leads to an important restriction on the irreducible representation of the little group at the M-point of Brillouin Zone (BZ). All the physical irreducible representations two dimensional referred to as M_1, M_2, M_3 and M_4 in Ref. [70]. The part near Fermi level of energy bands in monolayer FeSe is mainly made of the states of M_1- and M_3-doublets, around the M-point. The Fermi surface around M-point is mainly made of two orbitals, and they are linear combinations of $\{xz, yz\}$ and $x^2 - y^2$ orbitals of Fe ions as shown in Fig. A.1(c). Thus, its normal-state Hamiltonian is given in (M_1, M_3) space [32] with

$$H_{M_1 - M_3} = H_{\text{CV}} + H_{\text{SOC}}, \tag{A.1}$$

where

$$H_{\text{CV}} = \sum_{\boldsymbol{k}} \tilde{\Psi}_{\boldsymbol{k}}^{\dagger} \begin{bmatrix} \epsilon_1 \tilde{\tau}_0 \sigma_0 + a_1 k_x k_y \tilde{\tau}_z \sigma_0 & -iv \left(k_x \tilde{\tau}_0 + k_y \tilde{\tau}_z \right) \sigma_0 \\ iv \left(k_x \tilde{\tau}_0 + k_y \tilde{\tau}_z \right) \sigma_0 & \epsilon_3 \tilde{\tau}_0 \sigma_0 + a_3 k_x k_y \tilde{\tau}_z \sigma_0 \end{bmatrix} \tilde{\Psi}_{\boldsymbol{k}}, \tag{A.2}$$

and the spin-orbit coupling term

$$H_{\text{SOC}} = \sum_{\boldsymbol{k}} \tilde{\Psi}_{\boldsymbol{k}}^{\dagger} \begin{bmatrix} \lambda_1 \tilde{\tau}_x \left(k_y \sigma_x - k_x \sigma_y \right) & \lambda \left(-i \tilde{\tau}_x \sigma_y + \tilde{\tau}_y \sigma_x \right) \\ \lambda \left(i \tilde{\tau}_x \sigma_y + \tilde{\tau}_y \sigma_x \right) & \lambda_2 \tilde{\tau}_x \left(k_y \sigma_x + k_x \sigma_y \right) \end{bmatrix} \tilde{\Psi}_{\boldsymbol{k}}, \tag{A.3}$$

where $\boldsymbol{k} = (k_x, k_y)$ is momentum measured from M-point, $\tilde{\tau}_i$ matrices describe the two orbital (linear combinations of $\{xz, yz\}$ and $x^2 - y^2$ orbitals degrees of freedom) and σ_i matrices describes spin degrees of freedom, and $\tilde{\Psi}_{\boldsymbol{k}}$ is an eight-component spinor. We label each band of H_{CV} as $M_{1,1}$, $M_{1,2}$, $M_{3,1}$ and $M_{3,2}$. At the M-point, $M_{1,1}$ and $M_{1,2}$ ($M_{3,1}$ and $M_{3,2}$) are degenerate, as well as $M_{3,1}$- and $M_{3,2}$-bands and each band has spin degeneracy (Figure A.1(b)).

We will reduce this eight-band Hamiltonian to an effective model projected on the $M_{1,1}$ and $M_{3,1}$-bands. We assume that the energy scales of H_{SOC} are smaller than those of H_{CV}

(a)

(b)

(c)

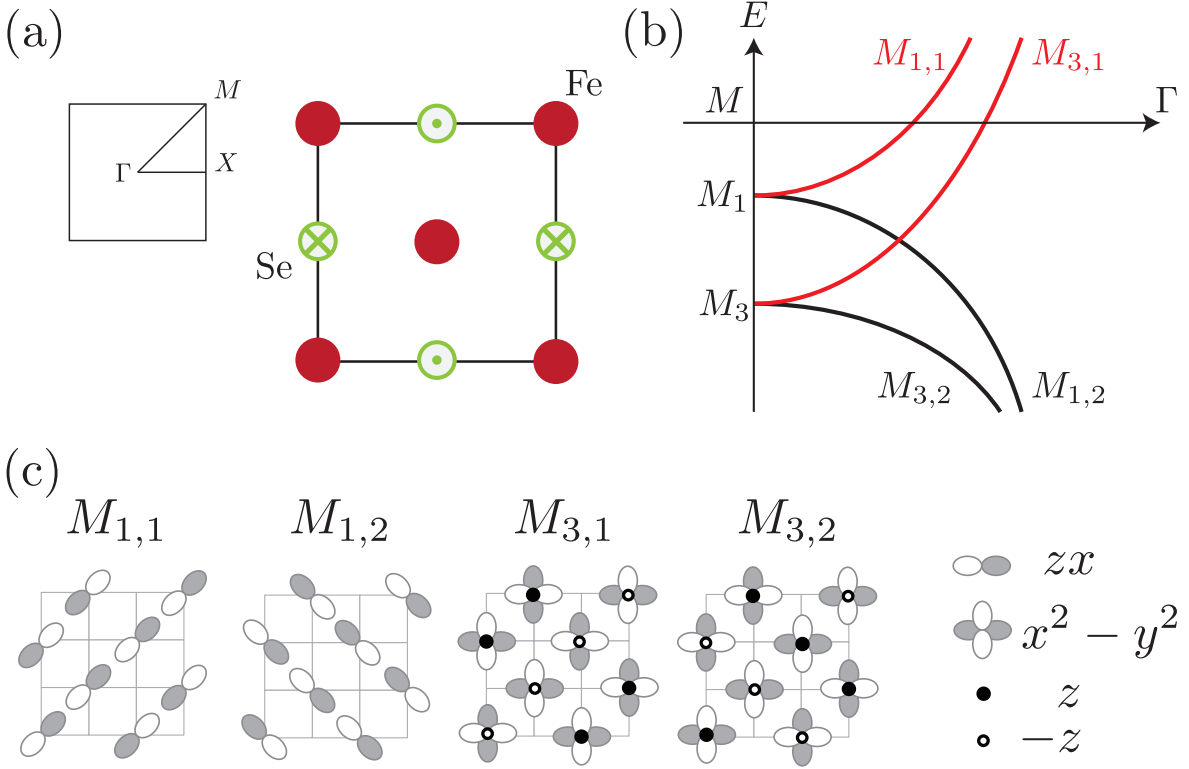$M_{1,1}$ $M_{1,2}$ $M_{3,1}$ $M_{3,2}$

Figure A.1: (a) Brillouin zone and unit cell of FeSe. One sublattice of the pnictide is puckered above and the other is puckered below the layer. (b) Schematic band structure of H_{CV} around the M-point of BZ. The red lines represent the bands near the Fermi level. We label each band as $M_{1,1}$, $M_{1,2}$, $M_{3,1}$ and $M_{3,2}$. At the M-point, $M_{1,1}$ and $M_{1,2}$ ($M_{3,1}$ and $M_{3,2}$) are degenerate and each band has spin degeneracy. Degenerate orbital basis sets at the M-point for the two electronic representations (M_1 and M_3) [32]. We note that the Fe sites are not inversion centers, allowing for p_z orbitals to mix with the $x^2 - y^2$ orbitals.

near the Fermi surface. The following effective Hamiltonian in normal states,

$$H_{\mathrm{M}} = \sum_{\boldsymbol{k}} \Psi_{\boldsymbol{k}}^{\dagger} \left[\epsilon_0 \left(\boldsymbol{k} \right) + \gamma_{xy} \left(\boldsymbol{k} \right) \tau_z + \tau_x \left(\gamma_y \left(\boldsymbol{k} \right) \sigma_x + \gamma_x \left(\boldsymbol{k} \right) \sigma_y \right) \right] \Psi_{\boldsymbol{k}}, \tag{A.4}$$

where τ_i matrices describe the two band degree of freedom, $\Psi_{\boldsymbol{k}}$ is a four-component spinor and

$$\epsilon_0 \left(\boldsymbol{k} \right) = \frac{\epsilon_1 + \epsilon_3}{2} + \frac{E_+ \left(\boldsymbol{k} \right) + E_- \left(\boldsymbol{k} \right)}{2}, \tag{A.5}$$

$$\gamma_{xy} \left(\boldsymbol{k} \right) = \frac{a_1 + a_3}{2} k_x k_y + \frac{E_+ \left(\boldsymbol{k} \right) - E_- \left(\boldsymbol{k} \right)}{2}, \tag{A.6}$$

$$\gamma_x \left(\boldsymbol{k} \right) = k_x \left[\lambda_1 A_+ \left(\boldsymbol{k} \right) A_- \left(\boldsymbol{k} \right) + \lambda_2 B_+ \left(\boldsymbol{k} \right) B_- \left(\boldsymbol{k} \right) \right]$$
$$+ i\lambda \left[A_+ \left(\boldsymbol{k} \right) B_- \left(\boldsymbol{k} \right) + B_+ \left(\boldsymbol{k} \right) A_- \left(\boldsymbol{k} \right) \right], \tag{A.7}$$

$$\gamma_y \left(\boldsymbol{k} \right) = k_y \left[-\lambda_1 A_+ \left(\boldsymbol{k} \right) A_- \left(\boldsymbol{k} \right) + \lambda_2 B_+ \left(\boldsymbol{k} \right) B_- \left(\boldsymbol{k} \right) \right]$$
$$+ i\lambda \left[A_+ \left(\boldsymbol{k} \right) B_- \left(\boldsymbol{k} \right) - B_+ \left(\boldsymbol{k} \right) A_- \left(\boldsymbol{k} \right) \right], \tag{A.8}$$

with

$$E_\pm\left(\boldsymbol{k}\right) = \sqrt{\gamma_\pm^2\left(\boldsymbol{k}\right) + v^2\left(k_x \pm k_y\right)^2}, \tag{A.9}$$

$$\gamma_\pm\left(\boldsymbol{k}\right) = \frac{\epsilon_1 - \epsilon_3 \pm \left(a_1 - a_3\right)k_x k_y}{2}, \tag{A.10}$$

$$A_\pm\left(\boldsymbol{k}\right) = -i\,\mathrm{sgn}\left(v\right)\mathrm{sgn}\left(k_x \pm k_y\right)\sqrt{\frac{1}{2}\left(1 + \frac{\gamma_\pm\left(\boldsymbol{k}\right)}{E_\pm\left(\boldsymbol{k}\right)}\right)}, \tag{A.11}$$

$$B_\pm\left(\boldsymbol{k}\right) = \sqrt{\frac{1}{2}\left(1 - \frac{\gamma_\pm\left(\boldsymbol{k}\right)}{E_\pm\left(\boldsymbol{k}\right)}\right)}. \tag{A.12}$$

The basis functions of $\Psi_{\boldsymbol{k}}$ are given by

$$\Psi_{\boldsymbol{k}} = \begin{pmatrix} \left|F_1\left(\boldsymbol{k}\right)\right\rangle \\ \left|F_2\left(\boldsymbol{k}\right)\right\rangle \end{pmatrix}, \tag{A.13}$$

with

$$\left|F_1\left(\boldsymbol{k}\right)\right\rangle = A_+\left(\boldsymbol{k}\right)\left|M_{1,1}\right\rangle + B_+\left(\boldsymbol{k}\right)\left|M_{3,1}\right\rangle, \tag{A.14}$$

$$\left|F_2\left(\boldsymbol{k}\right)\right\rangle = A_-\left(\boldsymbol{k}\right)\left|M_{1,2}\right\rangle + B_-\left(\boldsymbol{k}\right)\left|M_{3,2}\right\rangle. \tag{A.15}$$

Surprisingly, these two bands crossing the Fermi level belong the single representation M_3 although they originate from the M_1 and the M_3 representation. In other words, this means the basis $\left(\left|F_1\left(\boldsymbol{k}\right)\right\rangle, \left|F_2\left(\boldsymbol{k}\right)\right\rangle\right)$ transform as a M_3 representation [70] and $M_3 \otimes M_3$ is reduced to $A_{1g} \oplus B_{2g} \oplus A_{1u} \oplus B_{2u}$ of D_{4h} representation. This means that one can construct one-dimensional representations from product $F_i^\dagger F_j$ and we find that $A_{1g}:~F_1^\dagger F_1 + F_2^\dagger F_2~(\tau_0)$, $B_{2g}:~F_1^\dagger F_1 - F_2^\dagger F_2~(\tau_z)$, $A_{1u}:~F_1^\dagger F_2 - F_2^\dagger F_1~(\tau_y)$ and $A_{1g}:~F_1^\dagger F_2 + F_2^\dagger F_1~(\tau_x)$.

We briefly explain above by invoking Ref. [70]. $\epsilon_0\left(\boldsymbol{k}\right)$ in Eq. (A.5) and $\gamma_{xy}\left(\boldsymbol{k}\right)$ in Eq. (A.6) transform as A_{1g} and B_{2g} representation, respectively. $\left\{\gamma_x\left(\boldsymbol{k}\right), \gamma_y\left(\boldsymbol{k}\right)\right\}$ in Eqs. (A.7) and (A.8) transforms as E_{2u} representation. The symmetry of functions $f(\boldsymbol{k})$ and the Pauli matrices τ_j and σ_i which we used are shown in Table 3.2. The same analysis shows that the states in Eqs. (A.14) and (A.15) are a basis set of the M_3 representation since they are transformed as E_{M3} of Table III in Ref. [70].

In this thesis, instead of using the detailed expressions (A.5)–(A.8), we use $\epsilon_0\left(\boldsymbol{k}\right) = (k_x^2 + k_y^2)/2m - \mu$, $\gamma_x\left(\boldsymbol{k}\right) = v_{\mathrm{so}}k_x$, $\gamma_y\left(\boldsymbol{k}\right) = v_{\mathrm{so}}k_y$, $\gamma_{xy}\left(\boldsymbol{k}\right) = ak_x k_y$. We set there the parameters as $a = 600$ meV Å^2, $1/(2m) = 1375$ meV Å^2, $\mu = 55$ meV Å and $k_0 = 0.2$ Å^{-1} in order to reproduce the bands and the Fermi surface observed by ARPES [31]. Note that our $\boldsymbol{k}\cdot\boldsymbol{p}$-like Hamiltonian (A.4) is derived from symmetry arguments and there are no other terms in the form $\tau_i \sigma_j$.

Appendix B

Energy spectrum by Green's function method

In this appendix, we explain the recursive Green's function method [132] used in Section 3.3.

Let us set up a problem for electrons on a lattice that is semi-infinite in the x-direction and has a finite cross section in the other directions. We consider a Hamiltonian in which interactions are shot ranged and electrons on site with $x = n$ ($1 \leq n < \infty$) interact those at $x = n \pm 1$ only. Electrons at the edge $x = 0$ interact those at $x = 1$ only. Neglecting the edge effects, the Hamiltonian is defined as a block diagonal form

$$
\mathcal{H} = \begin{pmatrix}
A & B & 0 & 0 & 0 & 0 & \cdot & \cdot \\
B^\dagger & A & B & 0 & 0 & 0 & \cdot & \cdot \\
0 & B^\dagger & A & B & 0 & 0 & \cdot & \cdot \\
0 & 0 & B^\dagger & A & B & 0 & & \\
\cdot & \cdot & \cdot & & & & & \\
\cdot & \cdot & \cdot & & & & &
\end{pmatrix},
\tag{B.1}
$$

where A and B are square matrices and their dimensions are both 8 (or 4 in a reduced form) in our problem in Section 3.3. The Green's function is defined by

$$
G(\omega) = (\omega I - \mathcal{H})^{-1},
\tag{B.2}
$$

for a complex number ω and let us denote its (n, m)-block by $G_{nm}(\omega)$. For this form of Hamiltonian, López Sancho *et al.* [132] have developed a quickly convergent iterative scheme to calculate the surface and bulk Green's functions, i.e., $G_{0,0}$ and $G_{\infty,\infty}$ respectively. We explain this recursive method following Ref. [132].

The definition of Green's function leads to the following recursion relation

$$
\begin{align}
(\omega I - A)G_{0,0}(\omega) &= I + B\,G_{1,0}(\omega), \tag{B.3} \\
(\omega I - A)G_{n,0}(\omega) &= B^\dagger\,G_{n-1,0}(\omega) + B\,G_{n+1,0}(\omega) \quad (n \geq 1). \tag{B.4}
\end{align}
$$

Using Eqs. (B.4) and (B.3) with $n = 1$, we obtain the relation between $G_{0,0}$ and $G_{2,0}$ which is

$$
\left[\omega I - A - B(\omega I - A)^{-1}B^\dagger\right]G_{0,0}(\omega) = I + B\,(\omega I - A)^{-1}B\,G_{2,0}(\omega).
\tag{B.5}
$$

In the same way, one yields the general relation between $G_{n,0}$ and $G_{n\pm2,0}$:

$$\left[\omega I - A - B(\omega I - A)^{-1}B^{\dagger} - B^{\dagger}(\omega I - A)^{-1}B\right]G_{n,0}(\omega)$$
$$= B^{\dagger}(\omega I - A)^{-1}B^{\dagger}\,G_{n-2,0}(\omega) + B\,(\omega I - A)^{-1}B\,G_{n+2}(\omega) \quad (n \geq 2). \quad \text{(B.6)}$$

We note that the nearest neighbors ($G_{1,0}$ and $G_{n\pm1,0}$) disappeared in Eqs. (B.5) and (B.6). We write these relations more compactly,

$$(\omega I - \epsilon_1^{\rm s}(\omega))G_{0,0}(\omega) = I + \alpha_1(\omega)\,G_{2,0}(\omega), \tag{B.7}$$
$$(\omega I - \epsilon_1(\omega))G_{n,0}(\omega) = \beta_1(\omega)\,G_{n-2,0} + \alpha_1(\omega)\,G_{n+2,0}(\omega) \quad (n \geq 2), \tag{B.8}$$
$$(\omega I - \epsilon_1(\omega))G_{n,n}(\omega) = I + \beta_1(\omega)\,G_{n-2,n} + \alpha_1(\omega)\,G_{n+2,n}(\omega) \quad (n \geq 2), \tag{B.9}$$

where

$$\epsilon_i^{\rm s}(\omega) = A + B\,(\omega I - A)^{-1}\,B^{\dagger}, \tag{B.10}$$
$$\epsilon_i(\omega) = A + B(\omega I - A)^{-1}B^{\dagger} + B^{\dagger}(\omega I - A)^{-1}B, \tag{B.11}$$
$$\alpha_1(\omega) = B(\omega I - A)^{-1}B, \tag{B.12}$$
$$\beta_1(\omega) = B^{\dagger}(\omega I - A)^{-1}B^{\dagger}. \tag{B.13}$$

When we take even value for n, we obtain

$$(\omega I - \epsilon_i(\omega))G_{2n,0}(\omega) = \beta_1(\omega)\,G_{2(n-1),0}(\omega) + \alpha_1(\omega)\,G_{2(n+1),0}(\omega), \tag{B.14}$$
$$(\omega I - \epsilon_i(\omega))G_{2n,2n}(\omega) = I + \beta_1(\omega)\,G_{2(n-1),n}(\omega) + \alpha_1(\omega)\,G_{2(n+1),2n}(\omega). \tag{B.15}$$

Repeating above procedure i times, we have an iterative sequence

$$\epsilon_i^{\rm s}(\omega) = \epsilon_{i-1}^{\rm s}(\omega) + \alpha_{i-1}(\omega)\,(\omega I - \epsilon_{i-1})^{-1}\beta_{i-1}(\omega), \tag{B.16}$$
$$\epsilon_i(\omega) = \epsilon_{i-1}(\omega) + \alpha_{i-1}(\omega)\,(\omega I - \epsilon_{i-1}(\omega))^{-1}\beta_{i-1}(\omega)$$
$$\qquad\qquad + \beta_{i-1}(\omega)\,(\omega I - \epsilon_{i-1}(\omega))^{-1}\alpha_{i-1}(\omega), \tag{B.17}$$
$$\alpha_i(\omega) = \alpha_{i-1}(\omega)\,(\omega I - \epsilon_{i-1}(\omega))^{-1}\alpha_{i-1}(\omega), \tag{B.18}$$
$$\beta_i(\omega) = \beta_{i-1}(\omega)\,(\omega I - \epsilon_{i-1}(\omega))^{-1}\beta_{i-1}(\omega) \tag{B.19}$$

and the (renormalized) $G_{0,0}$ with 2^i-th layer:

$$(\omega I - \epsilon_i^{\rm s}(\omega))G_{0,0}(\omega) = I + \alpha_i(\omega)\,G_{2^i,0}(\omega), \tag{B.20}$$

and other elements given by

$$(\omega I - \epsilon_i(\omega))G_{2^i n,0}(\omega) = \beta_i(\omega)\,G_{2^i(n-1),0}(\omega) + \alpha_i(\omega)\,G_{2^i(n+1),0}(\omega), \tag{B.21}$$
$$(\omega I - \epsilon_i(\omega))G_{2^i n,2^i n}(\omega) = \beta_i(\omega)\,G_{2^i(n-1),2^i n} + \alpha_i(\omega)\,G_{2^i(n+1),2^i n}(\omega). \tag{B.22}$$

where theenergy matrices $\epsilon_i^{\rm s}$, ϵ_i, α_i, and β_i are determined recursively starting from $\epsilon_0^{\rm s} = \epsilon_0 = A$, $\alpha_0 = B$, and $\beta_0 = B^{\dagger}$. As the iteration proceeds, the effective interactions α_i and β_i decay quickly.

Figure B.1 shows k_y-resolved spectral functions obtained by this method,

$$N_n(k_y, E) = -\frac{1}{\pi}\,\text{Im Tr } G_{n,n}(k_y, E + i\eta) \tag{B.23}$$

at $n = 0$ (edge) and $n = \infty$ (bulk). Four parameter set are used Fig. 3.10 (a)-(d) in Sec. 3.3. The part near $k_y \sim 0$ is magnified in Fig. B.2. We take $\eta/t = 10^{-5}$ and stop the iteration when both $|\alpha_i/t|$ and $|\beta_i/t|$ are smaller than 10^{-7}. Required number of iterations are at most 20.
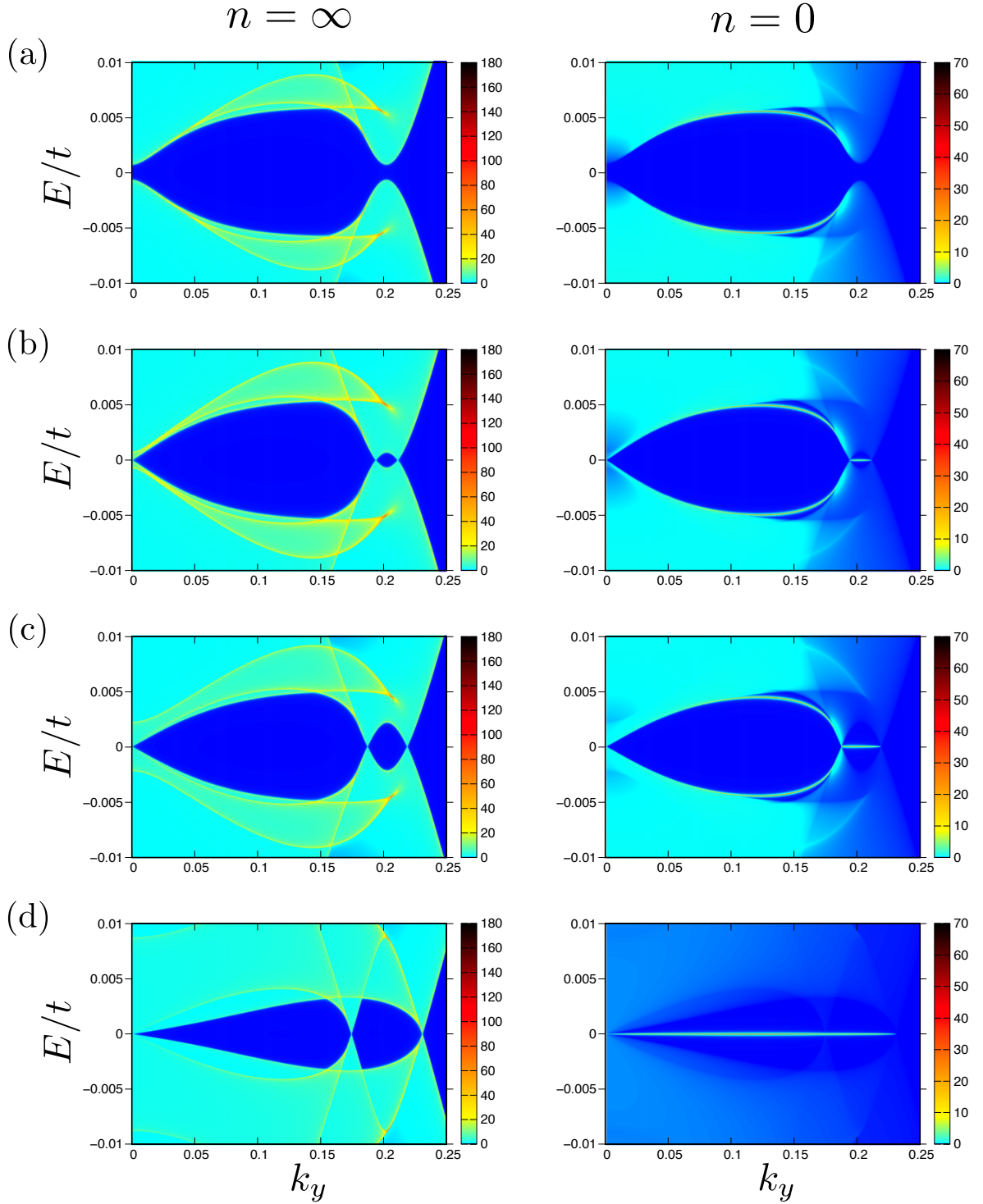
Figure B.1:   Momentum-resolved spectral function calculated by Green's function method. Left (Right) panels show local density of states in bulk (at edge). Dark blue area represents no-state region. (a) full gap, (b)(c) opposite sign pair of nodal points, (d) same sign pair of nodal points.
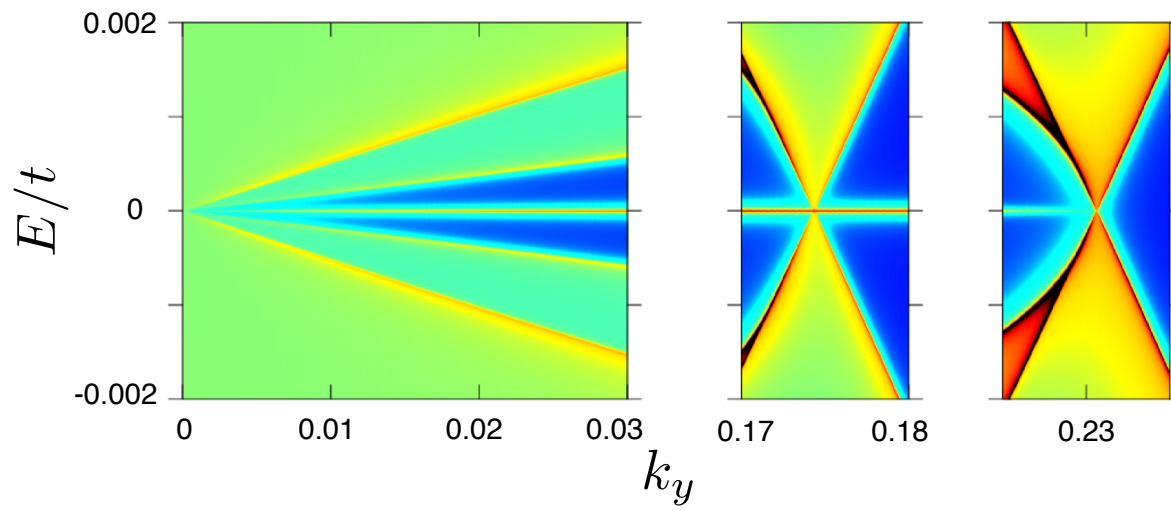
Figure B.2:   Low-energy part of spectral function (edge+bulk) of in Figure B.1 (d).

Appendix C

Character tables for the tetragonal and hexagonal point groups

Here we the show character tables of the point groups D_{4h} and D_{6h} [133]. Basis functions of their irreducible representations are also listed.

Table C.1: Character table and basis functions for the tetragonal point groups D_{4h}.

D_{4h}	E	$2C_4$	C_2	$2C_2'$	$2C_2''$	i	$2S_4$	σ_h	$2\sigma_v$	$2\sigma_d$	linear functions, rotations	quadratic functions	cubic functions
A_{1g}	$+1$	$+1$	$+1$	$+1$	$+1$	$+1$	$+1$	$+1$	$+1$	$+1$	—	$x^2+y^2,\ z^2$	—
A_{2g}	$+1$	$+1$	$+1$	-1	-1	$+1$	$+1$	$+1$	-1	-1	R_z	—	—
B_{1g}	$+1$	-1	$+1$	$+1$	-1	$+1$	-1	$+1$	$+1$	-1	—	x^2-y^2	—
B_{2g}	$+1$	-1	$+1$	-1	$+1$	$+1$	-1	$+1$	-1	$+1$	—	xy	—
E_g	$+2$	0	-2	0	0	$+2$	0	-2	0	0	$\{R_x,\ R_y\}$	$\{zx,\ yz\}$	—
A_{1u}	$+1$	$+1$	$+1$	$+1$	$+1$	-1	-1	-1	-1	-1	—	—	—
A_{2u}	$+1$	$+1$	$+1$	-1	-1	-1	-1	-1	$+1$	$+1$	z	—	$z^3,\ z\left(x^2+y^2\right)$
B_{1u}	$+1$	-1	$+1$	$+1$	-1	-1	$+1$	-1	-1	$+1$	—	—	xyz
B_{2u}	$+1$	-1	$+1$	-1	$+1$	-1	$+1$	-1	$+1$	-1	—	—	$z\left(x^2-y^2\right)$
E_u	$+2$	0	-2	0	0	-2	0	$+2$	0	0	$\{x,\ y\}$	—	$\left\{xz^2,\ yz^2\right\}$ $\left\{xy^2,\ x^2y\right\}$ $\left\{x^3,\ y^3\right\}$

Table C.2: Character table and basis functions for the hexagonal point groups D_{6h}.

D_{6h}	E	$2C_6$	$2C_3$	C_2	$3C_2'$	$3C_2''$	i	$2S_3$	$2S_6$	σ_h	$3\sigma_v$	$3\sigma_d$	linear functions, rotations	quadratic functions	cubic functions
A_{1g}	+1	+1	+1	+1	+1	+1	+1	+1	+1	+1	+1	+1	—	$x^2+y^2,\ z^2$	—
A_{2g}	+1	+1	+1	+1	-1	-1	+1	+1	+1	+1	-1	-1	R_z	—	—
B_{1g}	+1	-1	+1	-1	+1	-1	+1	-1	+1	-1	+1	-1	—	—	—
B_{2g}	+1	-1	+1	-1	-1	+1	+1	-1	+1	-1	-1	+1	—	—	—
E_{1g}	+2	+1	-1	-2	0	0	+2	+1	-1	-2	0	0	$\{R_x, R_y\}$	$\{zx,\ yz\}$	—
E_{2g}	+2	-1	-1	+2	0	0	+2	-1	-1	-2	0	0	—	$\{x^2-y^2,\ xy\}$	—
A_{1u}	+1	+1	+1	+1	+1	+1	-1	-1	-1	-1	-1	-1	—	—	—
A_{2u}	+1	+1	+1	+1	-1	-1	-1	-1	-1	-1	+1	+1	z	—	$z^3,\ z\left(x^2+y^2\right)$
B_{1u}	+1	-1	+1	-1	+1	-1	-1	+1	-1	+1	-1	+1	—	—	$x\left(x^2-3y^2\right)$
B_{2u}	+1	-1	+1	-1	-1	+1	-1	+1	-1	+1	+1	-1	—	—	$y\left(3x^2-y^2\right)$
E_{1u}	+2	+1	-1	-2	0	0	-2	-1	+1	+2	0	0	$\{x, y\}$	—	$\{xz^2,\ yz^2\}$ $\left\{x\left(x^2+y^2\right),\ y\left(x^2+y^2\right)\right\}$
E_{2u}	+2	-1	-1	+2	0	0	-2	+1	+1	-2	0	0	—	—	$\left\{xyz,\ z\left(x^2-y^2\right)\right\}$

Bibliography

[1] K. v. Klitzing, G. Dorda, and M. Pepper, New Method for High-Accuracy Determination of the Fine-Structure Constant Based on Quantized Hall Resistance, Phys. Rev. Lett. **45**, 494 (1980).

[2] D. J. Thouless, M. Kohmoto, M. P. Nightingale, and M. den Nijs, Quantized Hall Conductance in a Two-Dimensional Periodic Potential, Phys. Rev. Lett. **49**, 405 (1982).

[3] Xiao-Gang Wen, Topological orders in rigid states, Int. J. Mod. Phys. B **4**, 239 (1990).

[4] Yasuhiro Hatsugai, Chern number and edge states in the integer quantum Hall effect, Phys. Rev. Lett. **71**, 3697 (1993).

[5] Mahito Kohmoto, Topological invariant and the quantization of the Hall conductance, Ann. Phys. (N.Y.) **160**, 343 (1985).

[6] B. Andrei Bernevig, Taylor L. Hughes, and Shou-Cheng Zhang, Quantum Spin Hall Effect and Topological Phase Transition in HgTe Quantum Wells, Science **314**, 1757 (2006).

[7] Andreas P. Schnyder, Shinsei Ryu, Akira Furusaki, and Andreas W. W. Ludwig, Classification of topological insulators and superconductors in three spatial dimensions, Phys. Rev. B **78**, 195125 (2008).

[8] Alexander Altland and Martin R. Zirnbauer, Nonstandard symmetry classes in mesoscopic normal-superconducting hybrid structures, Phys. Rev. B **55**, 1142 (1997).

[9] Xiao-Liang Qi and Shou-Cheng Zhang, Topological insulators and superconductors, Rev. Mod Phys. **83**, 1057 (2011).

[10] Yoichi Ando and Liang Fu, Topological crystalline insulators and topological superconductors: from concepts to materials, Annu. Rev. Condens. Matter Phys. **6**, 361 (2015).

[11] Andreas P Schnyder and Philip M R Brydon, Topological surface states in nodal superconductors, J. Phys. Condens.: Matter. **27**, 243201 (2015).

[12] Masatoshi Sato and Yoichi Ando, Topological superconductors: a review, Rep. Prog. Phys. **80**, 076501 (2017).

[13] Nicholas Read and Dmitry Green, Paired states of fermions in two dimensions with breaking of parity and time-reversal symmetries and the fractional quantum Hall effect, Phys. Rev. B **61**, 10267 (2000).

[14] A Yu Kitaev, Unpaired Majorana fermions in quantum wires, Physics-Uspekhi **44**, 131 (2001).

[15] Yukio Tanaka and Satoshi Kashiwaya, Theory of Tunneling Spectroscopy of d-Wave Superconductors, Phys. Rev. Lett. **74**, 3451 (1995).

[16] Masatoshi Sato, Yukio Tanaka, Keiji Yada, and Takehito Yokoyama, Topology of Andreev bound states with flat dispersion, Phys. Rev. B **83**, 224511 (2011).

[17] Kazuhiko Kuroki, Seiichiro Onari, Ryotaro Arita, Hidetomo Usui, Yukio Tanaka, Hiroshi Kontani, and Hideo Aoki, Unconventional Pairing Originating from the Disconnected Fermi Surfaces of Superconducting LaFeAsO$_{1-x}$F$_x$, Phys. Rev. Lett. **101**, 087004 (2008).

[18] I. I. Mazin, D. J. Singh, M. D. Johannes, and M. H. Du, Unconventional Superconductivity with a Sign Reversal in the Order Parameter of LaFeAsO$_{1-x}$F$_x$, Phys. Rev. Lett. **101**, 057003 (2008).

[19] M. Yi, D. H. Lu, J. G. Analytis, J.-H. Chu, S.-K. Mo, R.-H. He, R. G. Moore, X. J. Zhou, G. F. Chen, J. L. Luo, N. L. Wang, Z. Hussain, D. J. Singh, I. R. Fisher, and Z.-X. Shen, Electronic structure of the BaFe$_2$As$_2$ family of iron-pnictide superconductors, Phys. Rev. B **80**, 024515 (2009).

[20] P Richard, T Sato, K Nakayama, T Takahashi, and H Ding, Fe-based superconductors: an angle-resolved photoemission spectroscopy perspective, Rep. Prog. Phys. **74**, 124512 (2011).

[21] P Richard, T Qian, and H Ding, ARPES measurements of the superconducting gap of Fe-based superconductors and their implications to the pairing mechanism, J. Phys. Condens.: Matter **27**, 293203 (2015).

[22] Andrey Chubukov, Pairing mechanism in Fe-based superconductors, Annu. Rev. Condens. Matter Phys. **3**, 57 (2012).

[23] Yi Gao, Wu-Pei Su, and Jian-Xin Zhu, Interorbital pairing and its physical consequences for iron pnictide superconductors, Phys. Rev. B **81**, 104504 (2010).

[24] Liang Fu, Odd-parity topological superconductor with nematic order: Application to Cu$_x$Bi$_2$Se$_3$, Phys. Rev. B **90**, 100509 (2014).

[25] Shingo Yonezawa, Kengo Tajiri, Suguru Nakata, Yuki Nagai, Zhiwei Wang, Kouji Segawa, Yoichi Ando, and Yoshiteru Maeno, Thermodynamic evidence for nematic superconductivity in Cu$_x$ Bi$_2$ Se$_3$, Nat. Phys. **13**, 123 (2017).

[26] P. M. R. Brydon, Limin Wang, M. Weinert, and D. F. Agterberg, Pairing of $j = 3/2$ Fermions in Half-Heusler Superconductors, Phys. Rev. Lett. **116**, 177001 (2016).

[27] Hyunsoo Kim, Kefeng Wang, Yasuyuki Nakajima, Rongwei Hu, Steven Ziemak, Paul Syers, Limin Wang, Halyna Hodovanets, Jonathan D. Denlinger, Philip M. R. Brydon, Daniel F. Agterberg, Makariy A. Tanatar, Ruslan Prozorov, and Johnpierre Paglione, Beyond triplet: Unconventional superconductivity in a spin-3/2 topological semimetal, Sci. Adv. **4**, eaao4513 (2018).

[28] Defa Liu, Wenhao Zhang, Daixiang Mou, Junfeng He, Yun-Bo Ou, Qing-Yan Wang, Zhi Li, Lili Wang, Lin Zhao, Shaolong He, Yingying Peng, Xu Liu, Chaoyu Chen, Li Yu, Guodong Liu, Xiaoli Dong, Jun Zhang, Chuangtian Chen, Zuyan Xu, Jiangping Hu, Xi Chen, Xucun Ma, Qikun Xue, and X J Zhou, Electronic origin of high-temperature superconductivity in single-layer FeSe superconductor, Nat. Commun. **3**, 931 (2012).

[29] Shaolong He, Junfeng He, Wenhao Zhang, Lin Zhao, Defa Liu, Xu Liu, Daixiang Mou, Yun-Bo Ou, Qing-Yan Wang, Zhi Li, Lili Wang, Yingying Peng, Yan Liu, Chaoyu Chen, Li Yu, Guodong Liu, Xiaoli Dong, Jun Zhang, Chuangtian Chen, Zuyan Xu, Xi Chen, Xucun Ma, Qikun Xue, and X J Zhou, Phase diagram and electronic indication of high-temperature superconductivity at 65 K in single-layer FeSe films, Nat. Mater. **12**, 605 (2013).

[30] Shiyong Tan, Yan Zhang, Miao Xia, Zirong Ye, Fei Chen, Xin Xie, Rui Peng, Difei Xu, Qin Fan, Haichao Xu, Juan Jiang, Tong Zhang, Xinchun Lai, Tao Xiang, Jiangping Hu, Binping Xie, and Donglai Feng, Interface-induced superconductivity and strain-dependent spin density waves in FeSe/SrTiO$_3$ thin films, Nat. Mater. **12**, 634 (2013).

[31] Y. Zhang, J. J. Lee, R. G. Moore, W. Li, M. Yi, M. Hashimoto, D. H. Lu, T. P. Devereaux, D.-H. Lee, and Z.-X. Shen, Superconducting Gap Anisotropy in Monolayer FeSe Thin Film, Phys. Rev. Lett. **117**, 117001 (2016).

[32] D. F. Agterberg, T. Shishidou, J. O'Halloran, P. M. R. Brydon, and M. Weinert, Resilient Nodeless d-Wave Superconductivity in Monolayer FeSe, Phys. Rev. Lett. **119**, 267001 (2017).

[33] Manfred Sigrist and Kazuo Ueda, Phenomenological theory of unconventional superconductivity, Rev. Mod. Phys. **63**, 239 (1991).

[34] B. Béri, Topologically stable gapless phases of time-reversal-invariant superconductors, Phys. Rev. B **81**, 134515 (2010).

[35] Andreas P. Schnyder and Shinsei Ryu, Topological phases and surface flat bands in superconductors without inversion symmetry, Phys. Rev. B **84**, 060504 (2011).

[36] Tomáš Bzdušek and Manfred Sigrist, Robust doubly charged nodal lines and nodal surfaces in centrosymmetric systems, Phys. Rev. B **96**, 155105 (2017).

[37] D. F. Agterberg, P. M. R. Brydon, and C. Timm, Bogoliubov Fermi Surfaces in Superconductors with Broken Time-Reversal Symmetry, Phys. Rev. Lett. **118**, 127001 (2017).

[38] Shingo Kobayashi, Ken Shiozaki, Yukio Tanaka, and Masatoshi Sato, Topological Blount's theorem of odd-parity superconductors, Phys. Rev. B **90**, 024516 (2014).

[39] Y. X. Zhao, Andreas P. Schnyder, and Z. D. Wang, Unified Theory of PT and CP Invariant Topological Metals and Nodal Superconductors, Phys. Rev. Lett. **116**, 156402 (2016).

[40] E. R. Schemm, W. J. Gannon, C. M. Wishne, W. P. Halperin, and A. Kapitulnik, Observation of broken time-reversal symmetry in the heavy-fermion superconductor UPt$_3$, Science **345**, 190 (2014).

[41] Youichi Yanase, Nonsymmorphic Weyl superconductivity in UPt$_3$ based on E_{2u} representation, Phys. Rev. B **94**, 174502 (2016).

[42] Youichi Yanase and Ken Shiozaki, Möbius topological superconductivity in UPt$_3$, Phys. Rev. B **95**, 224514 (2017).

[43] Zhiqiang Wang, John Berlinsky, Gertrud Zwicknagl, and Catherine Kallin, Intrinsic ac anomalous Hall effect of nonsymmorphic chiral superconductors with an application to UPt$_3$, Phys. Rev. B **96**, 174511 (2017).

[44] Grigory E Volovik, The Universe in a Helium Droplet (International Series of Monographs on Physics) (Oxford University Press, 2009).

[45] P. M. R. Brydon, D. F. Agterberg, Henri Menke, and C. Timm, Bogoliubov Fermi surfaces: General theory, magnetic order, and topology, Phys. Rev. B **98**, 224509 (2018).

[46] Anthony J. Leggett, A theoretical description of the new phases of liquid ^{3}He, Rev. Mod. Phys. **47**, 331 (1975).

[47] Masatoshi Sato, Nodal structure of superconductors with time-reversal invariance and $\mathbb{Z}_2$ topological number, Phys. Rev. B **73**, 214502 (2006).

[48] Shinsei Ryu, Andreas P. Schnyder, Akira Furusaki, and Andreas W. W. Ludwig, Topological insulators and superconductors: tenfold way and dimensional hierarchy, New J. Phys. **12**, 065010 (2010).

[49] Shunji Matsuura, Po-Yao Chang, Andreas P Schnyder, and Shinsei Ryu, Protected boundary states in gapless topological phases, New J. Phys. **15**, 065001 (2013).

[50] Y. X. Zhao and Z. D. Wang, Topological Classification and Stability of Fermi Surfaces, Phys. Rev. Lett. **110**, 240404 (2013).

[51] Ching-Kai Chiu and Andreas P. Schnyder, Classification of reflection-symmetry-protected topological semimetals and nodal superconductors, Phys. Rev. B **90**, 205136 (2014).

[52] Ching-Kai Chiu, Hong Yao, and Shinsei Ryu, Classification of topological insulators and superconductors in the presence of reflection symmetry, Phys. Rev. B **88**, 075142 (2013).

[53] Takahiro Morimoto and Akira Furusaki, Topological classification with additional symmetries from Clifford algebras, Phys. Rev. B **88**, 125129 (2013).

[54] Ken Shiozaki and Masatoshi Sato, Topology of crystalline insulators and superconductors, Phys. Rev. B **90**, 165114 (2014).

[55] Ching-Kai Chiu, Jeffrey C. Y. Teo, Andreas P. Schnyder, and Shinsei Ryu, Classification of topological quantum matter with symmetries, Rev. Mod. Phys. **88**, 035005 (2016).

[56] J. M. Luttinger and W. Kohn, Motion of Electrons and Holes in Perturbed Periodic Fields, Phys. Rev. **97**, 869 (1955).

[57] Guo-Yi Zhu, Fu-Chun Zhang, and Guang-Ming Zhang, Proximity-induced superconductivity in monolayer CuO_2 on cuprate substrates, Phys. Rev. B **94**, 174501 (2016).

[58] Wang Qing-Yan, Li Zhi, Zhang Wen-Hao, Zhang Zuo-Cheng, Zhang Jin-Song, Li Wei, Ding Hao, Ou Yun-Bo, Deng Peng, Chang Kai, Wen Jing, Song Can-Li, He Ke, Jia Jin-Feng, Ji Shuai-Hua, Wang Ya-Yu, Wang Li-Li, Chen Xi, Ma Xu-Cun, and Xue Qi-Kun, Interface-Induced High-Temperature Superconductivity in Single Unit-Cell FeSe Films on $SrTiO_3$, Chin. Phys. Lett. **29**, 037402 (2012).

[59] Q. Fan, W. H. Zhang, X. Liu, Y. J. Yan, M. Q. Ren, R. Peng, H. C. Xu, B. P. Xie, J. P. Hu, T. Zhang, and D. L. Feng, Plain s-wave superconductivity in single-layer FeSe on $SrTiO_3$ probed by scanning tunnelling microscopy, Nat. Phys. **11**, 946 (2015).

[60] Zhi Li, Jun-Ping Peng, Hui-Min Zhang, Wen-Hao Zhang, Hao Ding, Peng Deng, Kai Chang, Can-Li Song, Shuai-Hua Ji, Lili Wang, Ke He, Xi Chen, Qi-Kun Xue, and Xu-Cun Ma, Molecular beam epitaxy growth and post-growth annealing of FeSe films on $SrTiO_3$: a scanning tunneling microscopy study, J. Phys.: Condens. Matter **26**, 265002 (2014).

[61] Dennis Huang and Jennifer E. Hoffman, Monolayer FeSe on $SrTiO_3$, Annu. Rev. Condens. Matter Phys. **8**, 311 (2017).

[62] Sinisa Coh, Marvin L Cohen, and Steven G Louie, Large electron-phonon interactions from FeSe phonons in a monolayer, New J. Phys. **17**, 073027 (2015).

[63] Xiao Chen, S. Maiti, A. Linscheid, and P. J. Hirschfeld, Electron pairing in the presence of incipient bands in iron-based superconductors, Phys. Rev. B **92**, 224514 (2015).

[64] I. I. Mazin, Symmetry analysis of possible superconducting states in $K_xFe_ySe_2$ superconductors, Phys. Rev. B **84**, 024529 (2011).

[65] P. Myles Eugenio and Oskar Vafek, Classification of symmetry derived pairing at the M point in FeSe, Phys. Rev. B **98**, 014503 (2018).

[66] Zi-Xiang Li, Fa Wang, Hong Yao, and Dung-Hai Lee, What makes the Tc of monolayer FeSe on $SrTiO_3$ so high: a sign-problem-free quantum Monte Carlo study, Science Bulletin **61**, 925 (2016).

[67] Z. F. Wang, Huimin Zhang, Defa Liu, Chong Liu, Chenjia Tang, Canli Song, Yong Zhong, Junping Peng, Fangsen Li, Caina Nie, Lili Wang, X. J. Zhou, Xucun Ma, Q. K. Xue, and Feng Liu, Topological edge states in a high-temperature superconductor FeSe/$SrTiO_3$ (001) film, Nat. Mater. **15**, 968 (2016).

[68] T Shishidou, D F Agterberg, and M Weinert, Magnetic fluctuations in single-layer FeSe, Commun. Phys. **1**, 8 (2018).

[69] Qisi Wang, Yao Shen, Bingying Pan, Xiaowen Zhang, K Ikeuchi, K Iida, A D Christianson, H. C. Walker, D. T. Adroja, M. Abdel-Hafiez, Xiaojia Chen, D. A. Chareev, A. N. Vasiliev, and Jun Zhao, Magnetic ground state of FeSe, Nat. Commun. **7**, 12182 (2016).

[70] Vladimir Cvetkovic and Oskar Vafek, Space group symmetry, spin-orbit coupling, and the low-energy effective Hamiltonian for iron-based superconductors, Phys. Rev. B **88**, 134510 (2013).

[71] M. Z. Hasan and C. L. Kane, Colloquium: Topological insulators, Rev. Mod. Phys. **82**, 3045 (2010).

[72] Oskar Vafek and Ashvin Vishwanath, Dirac Fermions in Solids: From High-T_c Cuprates and Graphene to Topological Insulators and Weyl Semimetals, Annu. Rev. Condens. Matter Phys. **5**, 83 (2014).

[73] Andreas P. Schnyder, P. M. R. Brydon, and Carsten Timm, Types of topological surface states in nodal noncentrosymmetric superconductors, Phys. Rev. B **85**, 024522 (2012).

[74] Andrey V. Chubukov, Oskar Vafek, and Rafael M. Fernandes, Displacement and annihilation of Dirac gap nodes in d-wave iron-based superconductors, Phys. Rev. B **94**, 174518 (2016).

[75] Emilian M Nica, Rong Yu, and Qimiao Si, Orbital-selective pairing and superconductivity in iron selenides, npj Quantum Materials **2**, 24 (2017).

[76] Dmitry V. Chichinadze and Andrey V. Chubukov, Winding numbers of nodal points in Fe-based superconductors, Phys. Rev. B **97**, 094501 (2018).

[77] A. V. Chubukov, D. V. Efremov, and I. Eremin, Magnetism, superconductivity, and pairing symmetry in iron-based superconductors, Phys. Rev. B **78**, 134512 (2008).

[78] S. Raghu, Xiao-Liang Qi, Chao-Xing Liu, D. J. Scalapino, and Shou-Cheng Zhang, Minimal two-band model of the superconducting iron oxypnictides, Phys. Rev. B **77**, 220503 (2008).

[79] Andrew C. Potter and Patrick A. Lee, Edge Ferromagnetism from Majorana Flat Bands: Application to Split Tunneling-Conductance Peaks in High-T_c Cuprate Superconductors, Phys. Rev. Lett. **112**, 117002 (2014).

[80] M. Covington, M. Aprili, E. Paraoanu, L. H. Greene, F. Xu, J. Zhu, and C. A. Mirkin, Observation of Surface-Induced Broken Time-Reversal Symmetry in $YBa_2Cu_3O_7$ Tunnel Junctions, Phys. Rev. Lett. **79**, 277 (1997).

[81] Noah F. Q. Yuan and Liang Fu, Zeeman-induced gapless superconductivity with a partial Fermi surface, Phys. Rev. B **97**, 115139 (2018).

[82] Robert Joynt and Louis Taillefer, The superconducting phases of UPt_3, Rev. Mod. Phys. **74**, 235 (2002).

[83] R. A. Fisher, S. Kim, B. F. Woodfield, N. E. Phillips, L. Taillefer, K. Hasselbach, J. Flouquet, A. L. Giorgi, and J. L. Smith, Specific heat of UPt$_3$: Evidence for unconventional superconductivity, Phys. Rev. Lett. **62**, 1411 (1989).

[84] T. Trappmann, H. v. Löhneysen, and L. Taillefer, Pressure dependence of the superconducting phases in UPt$_3$, Phys. Rev. B **43**, 13714 (1991).

[85] J. P. Brison, N. Keller, P. Lejay, J. L. Tholence, A. Huxley, N. Bernhoeft, A. I. Buzdin, B. Fåk, J. Flouquet, L. Schmidt, A. Stepanov, R. A. Fisher, N. Phillips, and C. Vettier, Magnetism and superconductivity in heavy fermion systems, J. Low Temp. Phys. **95**, 145 (1994).

[86] S. Adenwalla, S. W. Lin, Q. Z. Ran, Z. Zhao, J. B. Ketterson, J. A. Sauls, L. Taillefer, D. G. Hinks, M. Levy, and Bimal K. Sarma, Phase diagram of UPt$_3$ from ultrasonic velocity measurements, Phys. Rev. Lett. **65**, 2298 (1990).

[87] Kazushige Machida and Masa-aki Ozaki, Superconducting double transition in a heavy-fermion material UPt$_3$, Phys. Rev. Lett. **66**, 3293 (1991).

[88] G. Aeppli, E. Bucher, C. Broholm, J. K. Kjems, J. Baumann, and J. Hufnagl, Magnetic order and fluctuations in superconducting UPt$_3$, Phys. Rev. Lett. **60**, 615 (1988).

[89] R. H. Heffner, D. W. Cooke, A. L. Giorgi, R. L. Hutson, M. E. Schillaci, H. D. Rempp, J. L. Smith, J. O. Willis, D. E. MacLaughlin, C. Boekema, R. L. Lichti, J. Oostens, and A. B. Denison, Muon spin rotation in the magnetic and superconducting ground states of (U,Th)Be$_{13}$ and (U,Th)Pt$_3$, Phys. Rev. B **39**, 11345 (1989).

[90] S. M. Hayden, L. Taillefer, C. Vettier, and J. Flouquet, Antiferromagnetic order in UPt$_3$ under pressure: Evidence for a direct coupling to superconductivity, Phys. Rev. B **46**, 8675 (1992).

[91] Victor M. Yakovenko, Theory of the High-Frequency Chiral Optical Response of a $p_x + ip_y$ Superconductor, Phys. Rev. Lett. **98**, 087003 (2007).

[92] DW Hess, TA Tokuyasu, and JA Sauls, Broken symmetry in an unconventional superconductor: a model for the double transition in UPt$_3$, J. Phys. Condens.: Matter **1**, 8135 (1989).

[93] Kazushige Machida, Masa-aki Ozaki, and Tetsuo Ohmi, Unconventional superconducting class in a heavy Fermion system UPt$_3$, J. Phys. Soc. Jpn. **58**, 4116 (1989).

[94] G. M. Luke, A. Keren, L. P. Le, W. D. Wu, Y. J. Uemura, D. A. Bonn, L. Taillefer, and J. D. Garrett, Muon spin relaxation in UPt$_3$, Phys. Rev. Lett. **71**, 1466 (1993).

[95] P. Dalmas de Réotier, A. Huxley, A. Yaouanc, J. Flouquet, P. Bonville, P. Imbert, P. Pari, P.C.M. Gubbens, and A.M. Mulders, Absence of zero field muon spin relaxation induced by superconductivity in the B phase of UPt$_3$, Phys. Lett. A **205**, 239 (1995).

[96] Benoit Lussier, Brett Ellman, and Louis Taillefer, Anisotropy of Heat Conduction in the Heavy Fermion Superconductor UPt$_3$, Phys. Rev. Lett. **73**, 3294 (1994).

[97] Benoit Lussier, Brett Ellman, and Louis Taillefer, Determination of the gap structure in UPt$_3$ by thermal conductivity, Phys. Rev. B **53**, 5145 (1996).

[98] Yoh Kohori, Takao Kohara, Hirofumi Shibai, Yasukage Oda, Yoshio Kitaoka, and Kunisuke Asayama, Nuclear Magnetic Relaxation in the Heavy-Fermion Superconductor UPt$_3$, J. Phys. Soc. Jpn. **57**, 395 (1988).

[99] E. A. Schuberth, B. Strickler, and K. Andres, Specific-heat anomaly in superconducting UPt$_3$ at 18 mK, Phys. Rev. Lett. **68**, 117 (1992).

[100] C. Broholm, G. Aeppli, R. N. Kleiman, D. R. Harshman, D. J. Bishop, E. Bucher, D. Ll. Williams, E. J. Ansaldo, and R. H. Heffner, Anisotropic temperature dependence of the magnetic-field penetration in superconducting UPt$_3$, Phys. Rev. Lett. **65**, 2062 (1990).

[101] A Yaouanc, P Dalmas de Réotier, A Huxley, J Flouquet, P Bonville, PCM Gubbens, and AM Mulders, Strong axial anisotropy of the magnetic penetration length in superconducting UPt$_3$, J. Phys. Condens.: Matter **10**, 9791 (1998).

[102] P Hirschfeld, D Vollhardt, and P Wölfle, Resonant impurity scattering in heavy fermion superconductors, Solid State Commun. **59**, 111 (1986).

[103] W. Putikka and Robert Joynt, Stability of anisotropic superconducting phases in UPt$_3$, Phys. Rev. B **37**, 2372 (1988).

[104] Robert Joynt, d-wave superconductivity and antiferromagnetism in UPt$_3$, J. Phys. Condens.: Matter **2**, 3415 (1990).

[105] H. Tou, Y. Kitaoka, K. Ishida, K. Asayama, N. Kimura, Y. Ōnuki, E. Yamamoto, Y. Haga, and K. Maezawa, Nonunitary Spin-Triplet Superconductivity in UPt$_3$: Evidence from ^{195}Pt Knight Shift Study, Phys. Rev. Lett. **80**, 3129 (1998).

[106] M.R. Norman, What is the superconducting order parameter for UPt$_3$?, Physica C: Superconductivity **194**, 203 (1992).

[107] C. H. Choi and J. A. Sauls, Identification of odd-parity superconductivity in UPt$_3$ from paramagnetic effects on the upper critical field, Phys. Rev. Lett. **66**, 484 (1991).

[108] JA Sauls, The order parameter for the superconducting phases of UPt$_3$, Advances in Physics **43**, 113 (1994).

[109] Matthias J. Graf, S.-K. Yip, and J. A. Sauls, Identification of the orbital pairing symmetry in UPt$_3$, Phys. Rev. B **62**, 14393 (2000).

[110] B. S. Shivaram, T. F. Rosenbaum, and D. G. Hinks, Unusual Angular and Temperature Dependence of the Upper Critical Field in UPt$_3$, Phys. Rev. Lett. **57**, 1259 (1986).

[111] K. Tenya, M. Ikeda, T. Tayama, T. Sakakibara, E. Yamamoto, K. Maezawa, N. Kimura, R. Settai, and Y. Ōnuki, Anisotropic Magnetic Response in the Superconducting Mixed State of UPt$_3$, Phys. Rev. Lett. **77**, 3193 (1996).

[112] Y. Machida, A. Itoh, Y. So, K. Izawa, Y. Haga, E. Yamamoto, N. Kimura, Y. Onuki, Y. Tsutsumi, and K. Machida, Twofold Spontaneous Symmetry Breaking in the Heavy-Fermion Superconductor UPt$_3$, Phys. Rev. Lett. **108**, 157002 (2012).

[113] Koichi Izawa, Yo Machida, Atsushi Itoh, Yoshitaka So, Katsuya Ota, Yoshinori Haga, Etsuji Yamamoto, Noriaki Kimura, Yoshichika Onuki, Yasumasa Tsutsumi, and Kazushige Machida, Pairing Symmetry of UPt$_3$ Probed by Thermal Transport Tensors, J. Phys. Soc. Jpn. **83**, 061013 (2014).

[114] Yasumasa Tsutsumi, Kazushige Machida, Tetsuo Ohmi, and Masa-aki Ozaki, A spin triplet superconductor UPt$_3$, J. Phys. Soc. Jpn. **81**, 074717 (2012).

[115] Shunichiro Kittaka, Koji An, Toshiro Sakakibara, Yoshinori Haga, Etsuji Yamamoto, Noriaki Kimura, Yoshichika Ōnuki, and Kazushige Machida, Anomalous Field-Angle Dependence of the Specific Heat of Heavy-Fermion Superconductor UPt$_3$, J. Phys. Soc. Jpn. **82**, 024707 (2013).

[116] E. I. Blount, Symmetry properties of triplet superconductors, Phys. Rev. B **32**, 2935 (1985).

[117] J. Bardeen, G. Rickayzen, and L. Tewordt, Theory of the Thermal Conductivity of Superconductors, Phys. Rev. **113**, 982 (1959).

[118] M. J. Graf, S-K. Yip, J. A. Sauls, and D. Rainer, Electronic thermal conductivity and the Wiedemann-Franz law for unconventional superconductors, Phys. Rev. B **53**, 15147 (1996).

[119] Patrick A. Lee, Localized states in a *d*-wave superconductor, Phys. Rev. Lett. **71**, 1887 (1993).

[120] Louis Taillefer, Benoit Lussier, Robert Gagnon, Kamran Behnia, and Hervé Aubin, Universal Heat Conduction in YBa$_2$Cu$_3$O$_{6.9}$, Phys. Rev. Lett. **79**, 483 (1997).

[121] M. Suzuki, M. A. Tanatar, N. Kikugawa, Z. Q. Mao, Y. Maeno, and T. Ishiguro, Universal Heat Transport in Sr$_2$RuO$_4$, Phys. Rev. Lett. **88**, 227004 (2002).

[122] Yoshihiro Koike, Naoto Metoki, Noriaki Kimura, Etsuji Yamamoto, Yoshinori Haga, Yoshichika Onuki, and Kunihiko Maezawa, Long Range Antiferromagnetic Ordering Observed Below 20 mK in the Heavy Fermion Superconductor UPt$_3$, J. Phys. Soc. Jpn. **67**, 1142 (1998).

[123] M.R. Norman, R.C. Albers, A.M. Boring, and N.E. Christensen, Fermi surface and effective masses for the heavy-electron superconductors UPt$_3$, Solid State Commun. **68**, 245 (1988).

[124] G J McMullan, P M C Rourke, M R Norman, A D Huxley, N Doiron-Leyraud, J Flouquet, G G Lonzarich, A McCollam, and S R Julian, The Fermi surface and f-valence electron count of UPt$_3$, New J. Phys. **10**, 053029 (2008).

[125] Takuya Nomoto and Hiroaki Ikeda, Exotic Multigap Structure in UPt$_3$ Unveiled by a First-Principles Analysis, Phys. Rev. Lett. **117**, 217002 (2016).

[126] B. Arfi and C. J. Pethick, Thermal conductivity and ultrasonic attenuation in heavy-fermion superconductors, Phys. Rev. B **38**, 2312 (1988).

[127] D. F. Agterberg, T. M. Rice, and M. Sigrist, Orbital Dependent Superconductivity in Sr_2RuO_4, Phys. Rev. Lett. **78**, 3374 (1997).

[128] C. J. Pethick and David Pines, Transport processes in heavy-fermion superconductors, Phys. Rev. Lett. **57**, 118 (1986).

[129] B. Arfi, H. Bahlouli, and C. J. Pethick, Transport properties of anisotropic superconductors: Influence of arbitrary electron-impurity phase shifts, Phys. Rev. B **39**, 8959 (1989).

[130] P. Wölfle and V. E. Koch, Theory of sound propagation in superfluid 3 He-A, J. Low Temp. Phys. **30**, 61 (1978).

[131] Suk Joo Youn, Mark H. Fischer, S. H. Rhim, Manfred Sigrist, and Daniel F. Agterberg, Role of strong spin-orbit coupling in the superconductivity of the hexagonal pnictide SrPtAs, Phys. Rev. B **85**, 220505 (2012).

[132] M. P. Lopez Sancho, J. M. Lopez Sancho, J. M. L. Sancho, and J. Rubio, Highly convergent schemes for the calculation of bulk and surface Green functions, J. Phys. F **15**, 851 (1985).

[133] George F. Koster, Properties of the thirty-two point groups (The MIT Press, 1963).